CMOS IMAGER FOR NANOSATELLITE APPLICATIONS

PATRICK IRVIN

A THESIS SUBMITTED TO THE FACULTY OF GRADUATE STUDIES IN PARTIAL FULFILLMENT OF THE REQUIREMENTS FOR THE DEGREE OF MASTER'S OF SCIENCE

GRADUATE PROGRAM IN EARTH AND SPACE SCIENCE
YORK UNIVERSITY
TORONTO, ONTARIO

October 2014

Abstract

This research examines the capabilities of Commercial-off-the-shelf CMOS image sensors for use on nanosatellites as a star tracker. An emphasis is placed on selecting low cost components that meet the restrictions on mass and power of nanosatellites. To determine the expected sky coverage a Monte Carlo simulation is used with different limiting magnitudes and orbits. An image sensor, and lens system are selected and are interfaced using a Field Programmable Gate Array for data processing. The camera is then characterized in lab before being tested imaging the night sky.

“Somewhere, something incredible is waiting to be known.”

- Carl Sagan

Acknowledgements

I would like to thank everyone at York University who has helped me, starting from undergrad all the way through my Masters, this would not have happened without you. Specifically I would like to thank my supervisor Dr. Regina Lee for all the support and for believing in me and this project from start to finish. The guidance I received from every faculty member at York has been very helpful in steering me in the right direction.

To all my friends in the Earth and Space Science Department, having the opportunity to relax and learn with you, whether at lunch or hanging out in the office, has helped make this a great experience and kept me going. Everyone in the YuSEND group, past and present, there are too many of you to name individually but your support and help with all my work has been invaluable, and your friendship in and outside of school is something I am honored to have gained.

To my friends outside of school and my family, the distractions that you have provided were a welcome change from the focus on work. The encouragement and belief that you gave me, combined with the patience you have with me is exceptional.

Lastly a special thanks to Tim, Sarah, and James for providing me with a great location for late night testing, both at the Lake and your house.

Table of Contents

List of Tables

List of Figures

List of Acronyms

ADC	Analog to Digital Converter
AEC	Automatic Exposure Control
AGC	Automatic Gain Control
APS	Active Pixel Sensor
BLC	Black Level Correction
CCD	Charge Coupled Device
CFOV	Circular Field of View
CMOS	Complementary Metal Oxide Semiconductor
COTS	Commercial off the Shelf
DEC	Declination
DFOV	Diagonal Field of View
DSNU	Dark Signal Non-Uniformity
ECEF	Earth Centred Earth Frame
ECIF	Earth Centred Inertial Frame
FDC	Frame Data Counting Module
FF	Fill Factor
FIFO	First In First Out
FPGA	Field Programmable Gate Array
FPN	Fixed Pattern Noise
FOV	Field Of View
GPIO	General Purpose Input/Output
HFOV	Horizontal Field of View
IRM	International Reference Meridian
IRP	International Reference Pole
kTc	Thermal Noise

LVDS	Low Voltage Differential Signal
MTF	Modulation Transfer Function
NORAD	North American Aerospace Defense Command
OA	Orientation Angle
PPOD	Poly Picosatellite Orbital Deployer
PRNU	Photo-Response Non-Uniformity
PSF	Point Spread Function
RA	Right Ascension
RMS	Root Mean Square
SCCB	Serial Camera Control Bus
SDSR	SRAM Data Storage and Retrieval Module
SNR	Signal to Noise Ratio
SOC	System on a Chip
SRAM	Static Random Access Memory
TWI	Two Wire Interface
UART	Universal Asynchronous Receiver/Transmitter
VFOV	Vertical Field of View
YuSEND	York University Space Engineering Nanosatellite Demonstration Group

Chapter 1 Introduction

1.1 Nanosatellites

The objective of this research is to determine the feasibility of Complementary Metal Oxide Semiconductors (CMOS) image sensors for nanosatellite applications. Nanosatellites are a specific type of satellite which have many constraints, such as mass and power, which any sensor must be designed to meet. A nanosatellite is a class of satellite defined as being less than 10kg and greater than 1kg [1]. Within the designation of nanosatellite there exists a subclass of satellites which follow the CubeSat Standard developed by California Polytechnic State University [2], it is worth noting that under the CubeSat standard satellites less than 10kg are classified as picosatellites, this is not the definition used in this thesis.

A typical nanosatellite, having a severe mass restriction, also has limited the surface area available for mounting solar panels. This is because as the dimensions increase the mass needed for structure also increases. In addition, the small size limits the options of using articulated solar panels which decreases the power that can be produced. This leads to a limit of power production of typically ≤5W for the largest nanosatellites.

CubeSats use a standardized geometry to reduce the requirements on developers for interfacing with launch vehicles and also to help group nanosatellites together to reduce launch costs by sharing deployment mechanisms. There are several different form factors which the CubeSat standard defines, as outlined in Table 1. The 3+U designates a satellite which has a component extending in the height direction outside of the main body of the satellite.

Table 1 - CubeSat Standard Form Factors

	Length(mm)	Width(mm)	Height(mm)	Mass(kg)
1U	100.0	100.0	113.5	1.33
1.5U	100.0	100.0	170.25	2.0
2U	100.0	100.0	227.0	2.66
3U	100.0	100.0	340.5	4.0
3+U	100.0	100.0	340.5+	4.0

The deployment vehicle developed by the California Polytechnic State University is known as the Poly Picosatellite Orbital Deployer (PPOD) and is seen in Figure 1. The PPOD allows for the deployment of multiple CubeSats smaller than 3U or a single 3U or 3+U. The PPOD is then attached to the launch vehicle removing the interface requirements from the developer of the nanosatellite and placing them on the PPOD developer.

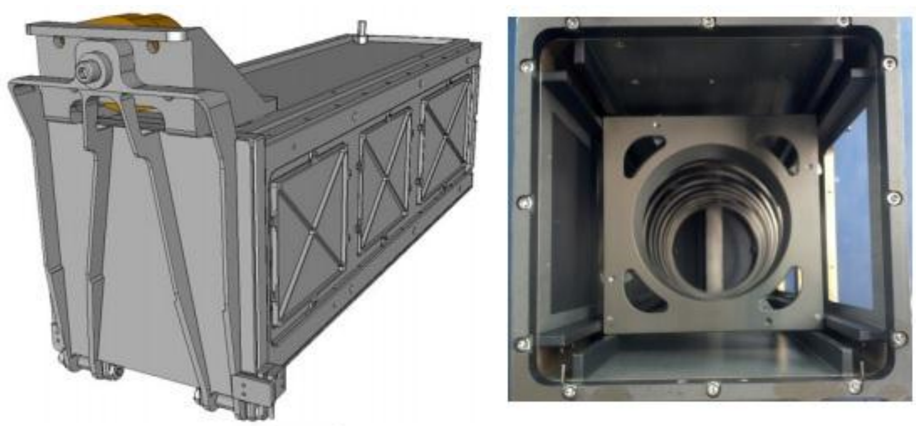

Figure 1 – The Poly Picosatellite Orbital Deployer. Image Credit: [2]

Nanosatellites, and especially CubeSats, are becoming increasingly popular due to their low cost of design, construction, and launch as well as rapid development cycles which allow smaller groups and even students to build, launch, and operate a satellite. These satellites typically rely on Commercial-Off-The-Shelf (COTS) components to reduce cost and increase reliability, the trade-off being that these parts are rarely space qualified. The inclusion of COTS components has allowed the nanosatellite community to take advantage of the increasing capability of advanced commercial electronics which are smaller in size, use less power but have abilities similar to technology used in larger spacecraft.

By examining the number of launches over the last 13 years of CubeSats, for which data is readily available from North American Aerospace Defense Command (NORAD), a clear trend is seen of increasing satellite launches as more educational institutions begin to develop CubeSat programs. Figure 2 shows that there have been progressively more launches each year since 2006 with the exception of 2011. The source of the decrease in launches in 2011 is likely due to launch vehicle failures.

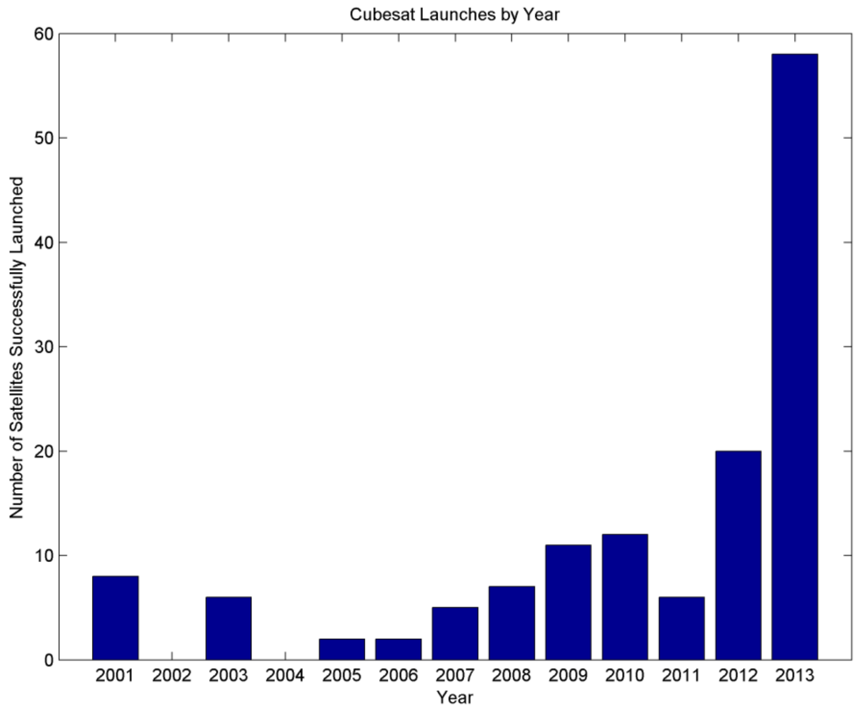

Figure 2 - CubeSats launched by year for 2001-2013.

The sudden increase in the number of CubeSats in 2013 is largely due to a pair of launches late in the year which included 11 [3] and 28 [4] satellites smaller than 10kg respectively. The second launch included a Microsatellite, less than 100kg, which housed and deployed 8 smaller satellites for the first time ever [5]. There are many future missions planned which will only increase the number and quality of nanosatellites such as QB50 which aims to use 50 nanosatellites from 35 different countries on orbit at once for research in the lower thermosphere [6].

1.2 Typical Attitude Sensors

There are a variety of sensors used on spacecraft for the purpose of attitude determination. Most spacecraft rely on several types of sensors, each with their own advantages and disadvantages, which in combination provide the attitude knowledge.

There are 5 main types of sensors often used to attain attitude knowledge, namely: Earth Sensors, Sun Sensors, Magnetometers, Rate Sensors and Star Trackers.

1.2.1 Earth Sensor

Earth sensors are imagers which determine where the satellite is pointing by looking for the thermal difference between Earth and deep space. This is done using a camera which is sensitive to Infrared radiation, this allows for the camera to look for the difference in temperature between the Earth and the much colder deep space. A typical accuracy for an Earth sensor is 0.1-0.25 degrees however there are limitations in its application [7]. The spacecraft must be Earth pointing, limiting the candidate satellites to those in Earth orbit, and it does not work when the sun or moon are in the field of view. An earth sensor designed for CubeSats is shown in Figure 3.

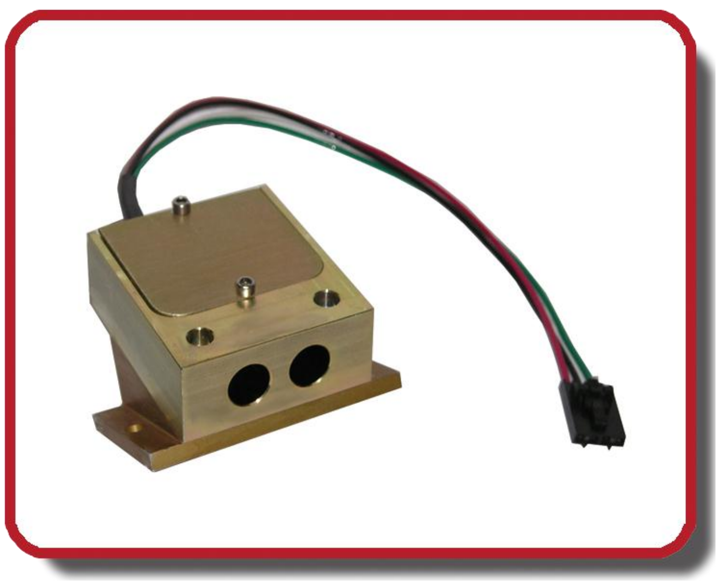

Figure 3 - An Earth sensor for CubeSats. Image Credit: [8]

1.2.2 Sun Sensor

There are two primary methods of performing sun sensing onboard satellites. The first is using a dedicated sun sensor; this is usually done through an array of discrete photodiodes or an image sensor. The Sun Sensor field of view is covered and then a small hole or slit is made allowing light to fall onto the detector. The satellite's vector to the sun can then be constructed using the signal position on the detector, with the Earth's sun vector in the Earth Centered Inertial Frame (ECIF), for satellites in Earth orbit, providing the attitude of the spacecraft. The primary limitation of a sun sensor is that it does not operate while the satellite is in eclipse and therefore relies on other forms of attitude determination for those periods. Furthermore several sun sensors are required on a spacecraft in order to maintain attitude knowledge during maneuvers where different faces of the spacecraft can be facing the sun.

Figure 4 - SSBV Sun sensor. Image Credit: [9]

The second method of sun sensing is achieved using the solar panels on the satellite itself. In this method the voltage or current being produced by the panels on different faces of the satellite are used to roughly determine the sun vector which again is compared to the sun vector in ECIF to get the attitude. This is possible due to the dependence of power production on solar angle.

Sun sensors provide accuracies from 0.005-3 degrees depending on the technique used, the quality of the sensors involved and the configuration of the spacecraft.

1.2.3 Magnetometer

Magnetometers are sensors which measure the direction and magnitude of the magnetic field of Earth. They rely on knowledge of the Earth's magnetic field to determine their attitude, however knowledge of the Earth's magnetic field is limited and imperfect. This severely limits the attitude knowledge gained to between 0.5-3 degrees. Due to their reliance on the Earth's magnetic field, magnetometers are not suitable for missions outside of Low Earth Orbit.

1.2.4 Gyroscopes/Rate Sensor

A Gyroscope, or Rate Sensor, is used to measure the angular rate of rotation of the spacecraft from an initial orientation. They do not provide any absolute attitude knowledge, and therefore are typically used in combination with other sensors such as star trackers or sun sensors to provide high frequency, high precision updates to attitude.

1.2.5 Star Tracker

Star Trackers, also referred to as Star Cameras, are imagers which take pictures of the sky and locate and identify stars to determine the attitude of a spacecraft. There are a variety of methods and algorithms for star tracking. A simple method is accomplished by forming a star triad, three stars that are visible in the image joined into a triangle, and comparing the triad formed against a star catalogue. The location of stars on the image sensor is determined to a sub-pixel level accuracy through a process known as centroiding. This yields an attitude vector which is accurate to arcsecond level. However, this process has several limitations, a minimum of three stars are required to form a triad and if the Sun or Moon enters the field of view the sensor becomes over saturated and individual stars are not distinguishable.

Most nanosatellites make use of a combination of the above sensors to increase reliability and robustness of their attitude determination systems. However, they are limited by the mass and power restrictions that small satellites face. A study in 2010 found that a majority of nanosatellites use sun sensors and magnetometers as they are the simplest sensors and most easily meet the volume, mass, and power restrictions imposed [10].

The accuracy that is afforded by these sensors is not sufficient for many scientific applications which require precise attitude knowledge. This is a developmental roadblock for nanosatellites, as unless they are able to produce scientific data and perform missions similar to larger microsatellites they remain a tool only for education and outreach. The next step in nanosatellite development is to create the tools necessary to produce valuable scientific data. As seen in Figure 5 less than 5% of nanosatellites use Star trackers which are the most accurate attitude determination sensor. Therefore the development of high accuracy small attitude sensors, such as star trackers, is essential for nanosatellites to continue to increase in functionality and reliability.

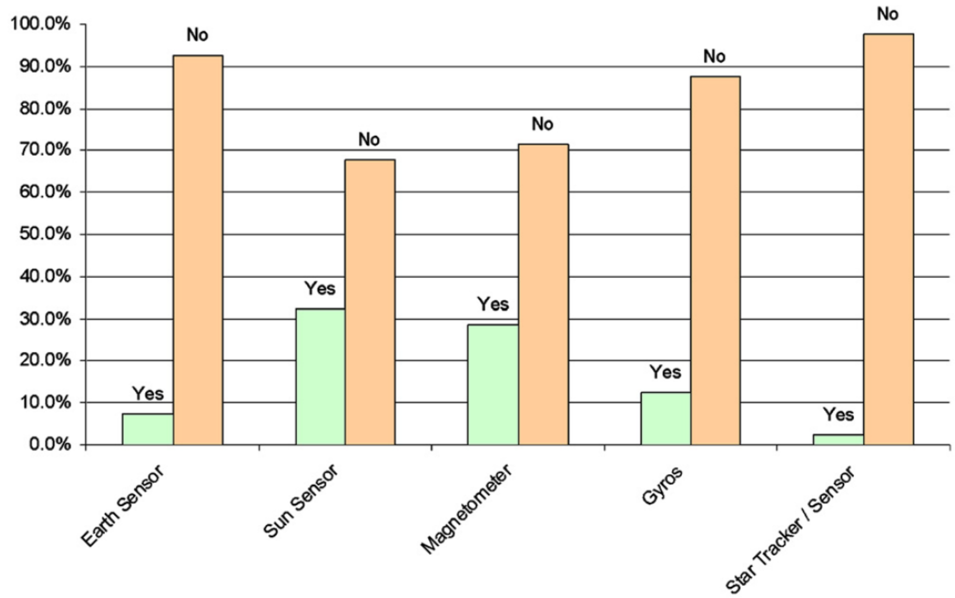

Figure 5 - Attitude sensors onboard nanosatellites. Image Credit: [10]

1.3 Star Tracker

1.3.1 Types of Star Trackers

There are several methods of star tracking that have been employed over the development of star tracker technology including: star trackers that look at a single star, V-slit star trackers and modern multi-star trackers.

Single Star Trackers

Single star trackers are used in conjunction with other attitude sensors such as sun sensors, which provide only two degrees of knowledge, to provide information on the last degree of freedom. A single bright star is selected from the Field of View (FOV) of the sensor which is oriented 90° to the sun sensor. This type of star tracker was utilized on the Voyager missions shown in Figure 6.

Figure 6 - Voyager Star Tracker and hood assembly. Image Credit: [11]

V-Slit Sensors

V-Slit sensors work by detecting the position and brightness of a star as it passes across two different sensor areas which are not parallel to each other as in Figure 7. This provides complete attitude knowledge, however imposes the requirement that the spacecraft be spinning so that the star passes over each slit. As a star passes across the first slit it generates a voltage proportional to the brightness of the star. When the star passes across the second slit the time is recorded and then the brightness, position and time are used to determine the attitude of the spacecraft [12]. These were commonly used on spin stabilized spacecraft such as Magellan and Galileo.

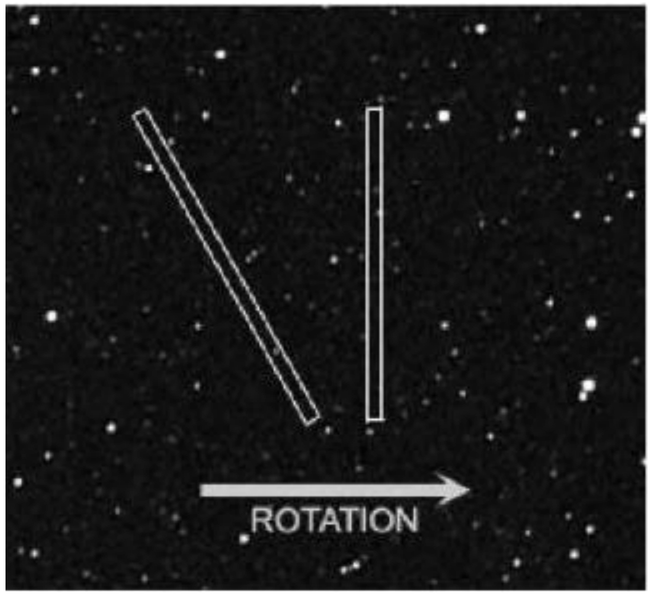

Figure 7 - V-Slit star sensor operation. Image Credit: [13]

Modern Multi-star Trackers

Modern multi-star trackers use current sensor technology to image large areas of the sky and track multiple stars. This allows for higher accuracy attitude determination and removes other restrictions such requiring additional attitude knowledge or spinning spacecraft. These sensors can work either by identifying and tracking specific stars or by imaging and tracking star triads.

1.3.2 Star Tracker Historical Development

Star trackers are the most accurate, commonly used attitude determination sensor for spacecraft. Therefore they are used on any mission where accurate attitude knowledge is required, such as for space telescopes and interplanetary missions. The principle behind the operation of a star tracker is that the stars that it images are considered to be inertially fixed, meaning that they do not appear to move as the sensor moves due to the extreme distance between the stars and the sensor. Using this knowledge, if a star is identified as being in a certain region of the sky, and that star is then imaged, it can be concluded that the camera must be pointing in that direction of the sky.

Electronic sensors for measuring directions using the stars have been utilized since the middle of the twentieth century. Originally they were used for large telescopes for pointing control and with the implementation of photomultiplier tubes in the 1940s applications expanded to bomber aircraft and missiles which required accurate pointing knowledge to determine their true heading [14].

The high accuracy exhibited by even these early sensors led to a strong space flight heritage. This was driven by the development of early interplanetary missions which required high pointing accuracy in order to communicate information back as their distance from Earth became very large. The earliest star sensors were restricted to tracking a single star at a time or required the satellite to be rotating, however, this began to change with the introduction of solid state imagers in the mid-1970s.

With the introduction of Charge-Coupled Devices (CCD) based image sensors the number of stars that could be imaged greatly increased. CCD sensors possess a very high fill factor per pixel, approaching 100%, allowing for high sensitivity. This means that almost the entire area of the pixel is sensitive to light. The simplicity of their design also allowed for CCD sensors to be smaller than those using photomultiplier tubes, with larger arrays of pixels. This turned CCD sensors into the dominant optical imaging sensor for applications requiring high sensitivity such as astronomy, spectroscopy and star trackers.

The first generation of star trackers using CCD sensors was still restricted to small FOVs and tracking only a few stars. Furthermore, processing of the images had to be done on the main computer, the star tracker was very heavy, and it required a lot of power. An example is the ASTRO star tracker made by Jet Propulsion Laboratory which weighed 41kg and used 43W of power [15].

The second generation of star trackers, which emerged in the 1990s, began taking advantage of the advancements in microprocessors which allowed for star trackers to perform star identification and pattern recognition autonomously from the rest of the satellite. Continued advancement led to a reduction in mass to less than 5 kg and in power to around 10W. In addition better electronics allowed for more stars to be viewed and for larger field of views to be used [15].

Subsequent generations of star trackers have been alluded to, although there are no clear distinctions as to what separates them from previous generations. It can be observed that some differences between previous and current generations are the use of multiple sensors and Fields of View (FOV) to increase sky coverage [16]. Another difference is the increase in use of Active Pixel Sensors (APS) based on CMOS technology.

1.3.3 Nanosatellite Imager Missions

Several nanosatellites have used cameras for a variety of purposes including outreach, increasing awareness of space and space programs, as well as attitude determination. The most common application remains as a technology demonstration for COTS cameras on nanosatellites. A study of nanosatellites that have used cameras was performed and is listed in Table 2.

.

Table 2 - Sample of Nanosatellite Imager Missions

Satellite	Launch Date	Institution	Resolution	Lens	Purpose
COMPASS-1 [17]	April 2008	Aachen University of Applied Sciences	640x480	Commercial	Outreach/Tech Demo
KySat-1 [18]	March 2011	University of Kentucky	640x480	Commercial	Outreach/Tech Demo
KySat-2 [19]	November 2013	University of Kentucky	2592x1944	Commercial	Stellar Gyroscope
CSTB-1 [20]	April 2007	Boeing	640x480	Information Not Available	Geolocation
ITUpSAT1 [21]	September 2009	Istanbul Technical University	640x480	Commercial	Tech Demo
CUTE 1.7 + APD [22]	April 2008	Tokyo Institute of Technology	640x480	Information Not Available	Tech Demo
AAU CubeSat [23]	June 2003	Aalborg University	1280x1024	Custom	Tech Demo

From this study it is concluded that most imagers are low resolution and rely on commercial lenses. This is a trend which can be seen among most nanosatellite as cameras are primarily included as non-mission-critical payloads and therefore development resources are minimal.

There are, however, several groups that are either developing or have flown cameras for the purpose of star tracking, including the CANX-1 satellite developed by the University of Toronto Institute for Aerospace Studies Space Flight Laboratory which included two imagers, one of which was used as a star tracker [24]. The University of Würzburg has developed STELLA, an autonomous star tracker that functions within the restrictions of a nanosatellite. STELLA draws just 200mW however its mass is still greater than 120g; including electronics for image processing [25]. California Polytechnic State University developed an imager to be used for multiple purposes including star imaging [26]. The University of Stellenbosch has developed a CubeSat based star tracker that uses 350mW and has a mass of around 100g [27].

1.3.4 Commercial Small Satellite Star Trackers

In addition to the development of cameras for nanosatellites the space industry has been developing smaller star trackers using newer technology to decrease the amount of satellite resources that they use. However, most of these sensors still use too much power and are too large for use on nanosatellites. A study of the smallest commercial star trackers can be seen in Table 3.

Table 3 - Commercially available small Star Trackers

	Dimensions(mm)	Power Consumption(W)	Mass(g)	Flight Heritage
Micro Advanced Stellar Compass [28]	DPU - 120x100x40 CHU – 50x50x50	4.3	800	FASTSAT BRITE SWARM
Space Micro MIST [29]	Information Not Available	3	500	None
Berlin Space Technologies ST-200 [30]	35x35 footprint	0.7	74	None
BCT Nano [31]	100x67.3x50	<1.0	350	Planned for INSPIRE
Sinclair Interplanetary ST-16 [32]	59x56x31.5	<1.0	85	BRITE-PL SkySat-1

From Table 3 it can be observed that the majority of small star trackers are still too large for use on most nanosatellites and the only ones that are potentially suitable for use are the ST-200, BCT Nano and ST-16, seen in Figure 8, due to their low power requirements. The other sensors simply draw too much power for a use on a nanosatellite.

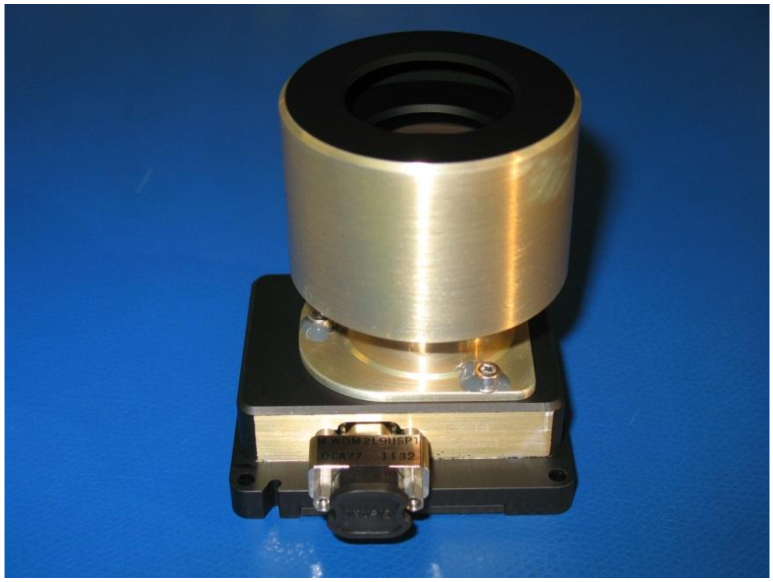

Figure 8 - ST-16 star tracker with baffle. Image Credit: [32]

1.4 CMOS versus CCD

1.4.1 CCD Operational Background

When comparing CMOS to CCD the advantages of one over another arise from the difference in technology and architecture. CCD technology is based on metal-insulator-semiconductor capacitors which collect, store and transfer charge through an array of pixels. Charge collection is done using photogates or photodiodes but the process is similar where electron hole pairs are generated in the depletion region of a semiconductor material [33]. The pixel has a simple design which allows it to maintain a fill factor near 100%, creating as many charge carriers as possible from the incident light on the area of each pixel. This also leads to excellent uniformity as each pixel behaves the same way to the same incident light.

CCD unlike CMOS does not have any readout electronics in each individual pixel. This requires that the charge collected at the pixel level be transported to a readout circuit. The charge is then transferred through the array of pixels which requires that each pixel be connected to the next one in the row. During this transfer some of the charge is inevitably lost since the transfer function is not 100% efficient. For an array of size 1000 pixels by 1000 pixels the pixel furthest from the readout circuit can go through up to 2000 transfers depending on the design of the sensor.

The final step is going through the readout circuitry where the transferred charge is converted into a voltage which represents the number of photons incident on the pixel. The additional readout circuitry converts the signal into a voltage, amplifies it, and outputs the data to a microprocessor where image processing occurs. A typical CCD image sensor can be seen in Figure 9.

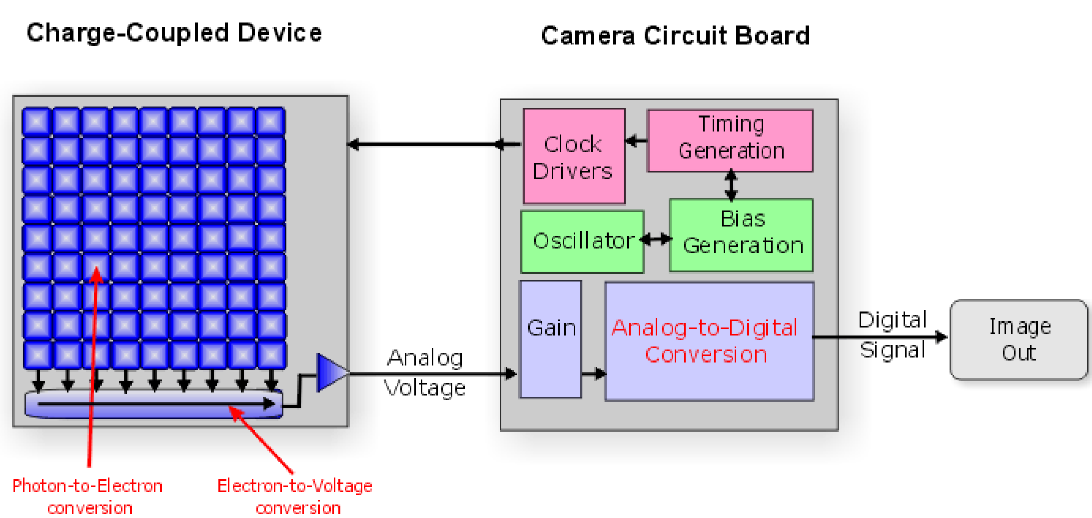

Figure 9 – A typical CCD sensor architecure. Image Credit: [34]

1.4.2 CMOS Advantages

CMOS technologies provide several advantages over CCD based image sensors, the majority of which are due to the readout process being done in chip rather than on separate readout electronics. Since CMOS are System on a Chip (SOC) they are considerably smaller than a CCD which requires an additional unit for image output in addition to the monolithic sensor. This gives CMOS sensors an advantage in mass when the entire camera system is taken into account. This also allows CMOS to integrate multiple different types of readout electronics, image processing blocks, data compression blocks or others directly onto the sensor delivering superior functionality for the system [35].

Since each pixel has its own readout circuit an entire image can be read out almost simultaneously, depending on whether there is a rolling or global shutter, which is ideal for high speed applications. Furthermore, since each pixel has its own readout circuitry, individual regions can be read out independent of an entire image or multiple regions can be read out at once, known as windowing [36]. This is useful in applications involving tracking of individual features from within an image such as star tracking where the location of stars from frame to frame changes very slowly. This allows for even faster readout as less data needs to be read from the sensor allowing for higher update rates and more accurate tracking.

Another advantage from reading out each pixel individually is that each pixel has a great deal of independence from the others. As a result when a pixel becomes oversaturated it does not bleed over into the pixels next to it since there are no paths for charge carriers to take. This greatly reduces an effect known as blooming, the overflow of charge carriers from one pixel to another, which is a common problem in a CCD sensor. Smearing is another effect of bright objects that appears in CCD images. It is created by the readout process when charge is not completely transferred from one pixel to the next, resulting in vertical streaks or lines appearing. An example of this can be seen in Figure 10. The image on the left was taken with a CCD and is unedited, the image on the right has had antiblooming and anti-smear software used to increase the quality of the image [37].

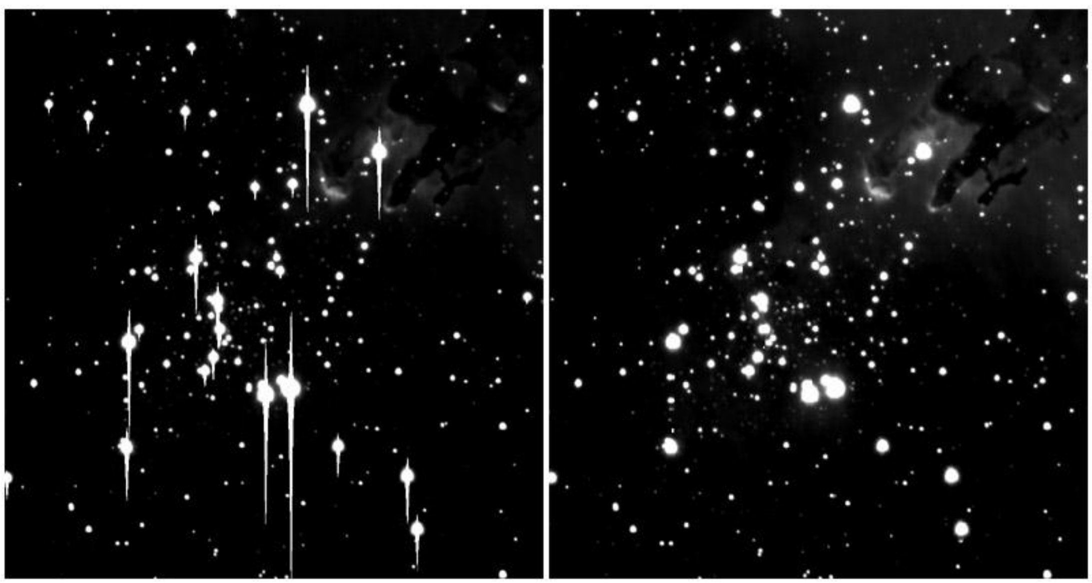

Figure 10 - Example of smearing and blooming, original image on left, image with filter on right. Image Credit: [37]

In addition, CMOS operate at a lower voltage than CCD, which leads to lower power consumption. Furthermore, CMOS only requires a single supply voltage, while CCDs often require multiple supply voltages, increasing complexity.

Lastly CMOS sensors are the most commonly used imaging sensor in production today due to the advantages previously outlined. As such they are produced for a variety of industries and purposes which has increased both the quantity and the quality of

CMOS image sensors in general. This has resulted in a drop in price for these sensors as they are produced on a much greater scale than CCD sensors, and the same sensor can be used for multiple purposes due to its flexibility [35].

1.4.3 CMOS Technology Disadvantages

CCD technology possesses several advantages over CMOS technology due to its different architecture; primarily CCDs produce better quality images, especially in low light situations. This is due to their increased sensitivity and their superior noise function. Sensitivity is defined as the amount of charge produced per photon incident on a pixel. It is affected by two factors, the Fill Factor (FF) of the pixel and the Quantum Efficiency. Fill Factor is the ratio of pixel area which is photosensitive to the total pixel area. In CCD sensors FF approaches 100% while on CMOS, depending on the specific sensor, FF ranges from 30%-80% [38].

Quantum Efficiency is the ratio of charge carriers in the depletion zone that are collected relative to the total number of photons incident on the pixel [35]. Quantum Efficiency is wavelength dependent and for CMOS sensors typically ranges from 30%-40%, CCD sensors meanwhile have Quantum Efficiencies approaching 80% depending on the type of sensor [39]. However, when techniques like anti-blooming are applied to CCDs their Quantum Efficiency can fall to below that of a CMOS [40].

Noise sources severely limit the quality of images in low light situations for CMOS sensors due to their read out circuitry and greater sensitivity to thermal noise. This limits the lower level of sensitivity that is achievable from these sensors in low light situations [35]. Therefore the cutoff brightness of a CMOS sensor is higher than that of a CCD.

1.5 Thesis Statement

The primary objective of this thesis is to select and characterize a CMOS sensor and lens for use as a star imager. The thesis focuses on selecting low-cost Commercial-Off-The-Shelf components that meet the power and mass restrictions of typical nanosatellites requirements. The imager must be capable of operating in the space environment with minimal modifications. There are three research objectives, (1) to determine what magnitude stars are visible, (2) determine the uncertainty of the position of imaged stars, and (3) to determine potential sky coverage for the star tracker. This is achieved through characterization of the lens and sensor and verified with a series of in lab and night sky image tests.

1.6 Outline

This thesis is presented in 7 main chapters. The first is an introduction which provides an overview of development of nanosatellites and small attitude sensors with a focus on star imagers as well as introduces the focus of this research.

The second chapter is a background to star tracking and CMOS operations as well as the selection process of the hardware sensor and lens.

The third chapter is a simulation to determine the sky coverage that can be expected from the selected sensor based on a variable FOV and minimum detectable brightness. Systems Toolkit is integrated into the simulation to determine sky coverage for a hypothetical CubeSat.

The fourth chapter specifies the hardware implementation, FPGA designs, breakout board designs, and environmental testing.

The fifth chapter details the calibration processes and results.

The sixth chapter analyzes images taken at night in low light pollution using the calibration data from chapter five.

The final chapter summarizes the contents and provides a discussion of the applications of the research and future work that can be done to improve the camera.

Chapter 2 CMOS and Star Imaging Background

2.1 CMOS Operation background

A CMOS image sensor detects photons by way of the photovoltaic effect in the same way as a CCD sensor. The photovoltaic effect states that when a light is shone on a surface, in the case of image sensors the semiconductor silicon, that valence band electrons become excited and jump to the conduction band. This creates electron hole pairs which are moved by the electric field of the depletion region creating the potential [41] [42]. A typical CMOS sensor configuration can be seen below in Figure 11.

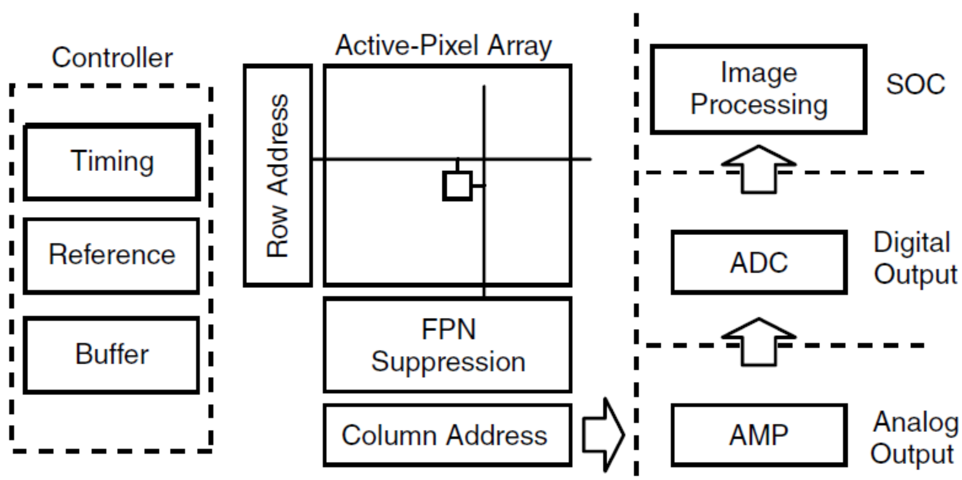

Figure 11 – Typical APS CMOS architecture. Image Credit: [43]

Most CMOS image sensors are known as system-on-a-chip (SOC) sensors meaning that all the components of the sensor are integrated together onto the same chip. This includes the pixel array, read out architecture, analog to digital (ADC) converters and image processing. Image processing that is performed on the sensor itself can include

Automatic Exposure Control (AEC), Automatic Gain Control AGC), Black Level Correction (BLC) and others [43]. The row and column address busses allow for the selection of individual pixels or regions of the sensor to be read out. From here, depending on whether the sensor has a global shutter or rolling shutter, read out can be done two different ways. For a rolling shutter, read out is done in two distinct steps: there is a pixel readout that takes place on the pixel itself and a column readout which reads all the pixels in a row at one time before outputting them. This produces a rolling effect as each column is read out one after another. A global shutter has only one readout step: all readout is done on the pixel and all pixels are read at the same time. Another way in which CMOS technology differs is in the design of the pixels in the image sensor itself, an image of which can be seen below in Figure 12.

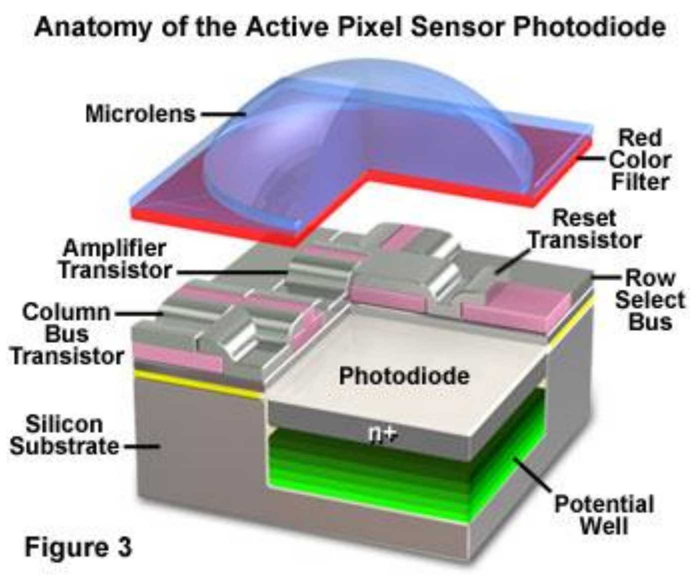

Figure 12 - An Active Pixel Sensor CMOS pixel. Image Credit: [44]

Each APS CMOS sensor is comprised of thousands of the pixels seen in Figure 12. An important feature is the fraction of the pixel area that is reserved for the photodiode; this is the light sensitive area of the pixel and is referred to as the Fill Factor.

As a result of the FF not being close to 100%, a micro lens is used to focus the incident light onto only the area that is photosensitive to increase the efficiency of the pixel.

The remainder of the pixel surface area is dedicated to read out electronics that consist of a number of transistors. The simplest CMOS pixel is known as a 3T pixel and is named for having 3 transistors on the die in each pixel. The three transistors are the source-follower (amplifier) transistor, reset transistor and the row-select transistor. When taking a picture the reset switch is turned off to start the collection of charge on the photodiode and then is turned on, causing the charge to be read out as a voltage. While off, charge is collected by the natural capacitance of the silicon photodiode, the source-follower, and the reset and is converted to a signal voltage which is stored by the row-select transistor when the reset switch is closed [45] [42]. The source-follower acts as an amplifier which increases the signal current. The row-select transistor is then turned on when the entire row is to be read out. The entire pixel array cannot be read out simultaneously because each element of the column bus can only hold one pixel at a time. Therefore the read out must be staggered and each row is read one at a time to produce what is known as an electronic rolling shutter.

The 3T pixel is popular due to its simplicity and the ability to be produced in large quantities making it ideal for low cost applications. However, there are several drawbacks to the implemented design such as high noise and image lag. High noise is due to the sense node connecting to the n+ doped area of the photodiode, producing dark current and thermal noise (kTC). Image lag is when a bright object produces a signal that saturates a pixel and the following image shows a residual effect. This is caused by the reset operation not entirely emptying the pixels charge before the following integration period begins [45].

2.2 Noise Sources

All imagers are susceptible to noise from a variety of sources. This noise causes the signal that is read out of the pixels to vary from the true signal created by the photon flux incident on the sensor. As a result, when imaging stars, the point spread function of the star is distorted, causing the centroiding location to be incorrect. This in turn leads to a less accurate determination of the attitude of the spacecraft. There are a number of noise sources that CMOS technologies are susceptible to which are grouped into two categories, temporal and spatial. Temporal noise is from dark current noise, shot noise, reset noise and amplifier noise. The remaining noise sources are typically categorized as being Spatial Noise because they are time invariant. They include dark current, photodiode sensitivity, and the characteristics of the on chip electronics like the ADC and amplifier [45] [43] [41]. Some noise sources such as Fixed Pattern Noise (FPN) and dark current noise can be measured and their effect on an image reduced. Other noise sources are addressed mainly through the architecture of the pixel itself and therefore cannot be easily removed. These still have an impact on the performance of the sensor and when other noise sources are removed they are the remaining sources of noise the image sensor must address.

2.2.1 Fixed Pattern Noise

Fixed Pattern Noise (FPN) is a result of the inconsistencies between pixels in the image sensor with respect to their response to a uniform light source as well as difference in parameters of individual transistors. This is due to a number of factors that have to do with the design and manufacturing of the image sensor. The substrate is a doped semiconductor and it is not possible to ensure doping uniformity across the entire substrate, therefore the creation of electron-hole pairs is spatially dependent and the effect of amplifiers is non-uniform. The thickness of coatings as well as the exact size of the detector also varies slightly which produces a different response to incoming light. This results in some pixels always producing an image level that is above or below the actual scene level. FPN can be broken into two parts, the Dark Signal Non-Uniformity (DSNU) and Photo-Response Non-Uniformity (PRNU) for scenes with and without illumination.

One technique for removing FPN involves taking a large number of images of a uniform illumination level and averaging the values to get a value for each pixel that is not dependent on the temporal noise sources. This value can then be compared to all the other pixels and a correction for each pixel can be produced [46]. This can depend on exposure time therefore the test must be completed for various exposure times.

2.2.2 Dark Current Noise

In an ideal imager if the sensor is completely covered and no light is incident on the photosensitive surface then the resulting image would be completely dark. However, this is not the case due to dark current. Dark current is a property that all semiconductors have. It is the generation of a current by thermal excitation of electron hole pairs between the conduction and valence bands. This current is generated in three locations on the Silicon substrate; in the depletion region, in the neutral material below the depletion region and at the interface between Silicon and Silicon Dioxide layers [41]. The quality of the Silicon used for the substrate can help decrease the dark current but it is generally accepted that the only way to decrease dark current is through cooling the sensor. It is rare for a nanosatellite to have any thermal control that would allow for the control of the temperature of the sensor and adding a dedicated thermal control system for just the imager would take up valuable space or power that nanosatellites do not have available.

The amount of noise generated due to dark current has been shown to be directly proportional to the exposure time of the image when the exposure time is greater than the frame time [47]. For exposures shorter than the frame time most pixels have a constant dark current, when exposures are longer than the frame time dark current increases linearly. In either case hot pixels exhibit linearly increasing noise due to dark current regardless of exposure time. In the case of imaging dim objects for applications like star tracking, longer exposure times can be helpful to allow the sensor to collect more photons. That must be traded off against the additional dark current that is generated by the sensor.

2.2.3 Other Noise Sources

Shot Noise

Shot Noise is caused when charge carriers are spontaneously created and cause a current to flow across a potential barrier. Shot Noise comes from two sources, incident photons and Dark Current. The incident photons come at unknown times and therefore cannot be predicted nor accounted for, making them a temporal noise source. The Dark Current portion comes from randomly created electron hole pairs in the depletion region that bleed over the potential barriers [33].

Reset Noise

Reset Noise occurs during the readout process of the imager. When the pixel value has been read out the reset transistor is cycled on and off, Reset Noise is caused by the natural resistance of the transistor due to thermal excitation during this process. This results in the reported value fluctuating and the system reading out the wrong value.

Amplifier Noise

Amplifier noise comes from the source-follower transistor and is made up of two components: 1/f noise and white noise. 1/f noise is also referred to as flicker noise and is generally considered to be caused by the creation of energy levels within the band gap due to the inconsistencies of the silicon lattice structure at the surface, as well as from tunneling noise from electrons in the oxide layers [41]. 1/f noise increases with the readout time of the sensor [48]. White noise is also referred to as Johnson noise and is another thermal noise caused by the resistance of the amplifier. It appears as a random fluctuation in the signal output by the amplifier and is temporal in nature.

2.3 Aberrations

Aberrations are distortions of an image on the image plane of the sensor caused by the lens and the sensor itself. Unlike noise, no information from the image is lost; it is merely translated on the image plane or has its point spread function altered. In the case of star tracking, it is important to correctly locate the star on the image plane as both the distance from it to other stars is used to identify star triads. Once the triad is identified, its position is used to determine the attitude of the satellite.

2.3.1 Distortion

Distortion is introduced by the lens system and produces a translation of image information on the image plane. It produces either pincushion or barrel distortion which appear as in Figure 13. Distortion can cause misidentification or prevent identification of star triads entirely by translating the position of the star from where it is in the star catalogue.

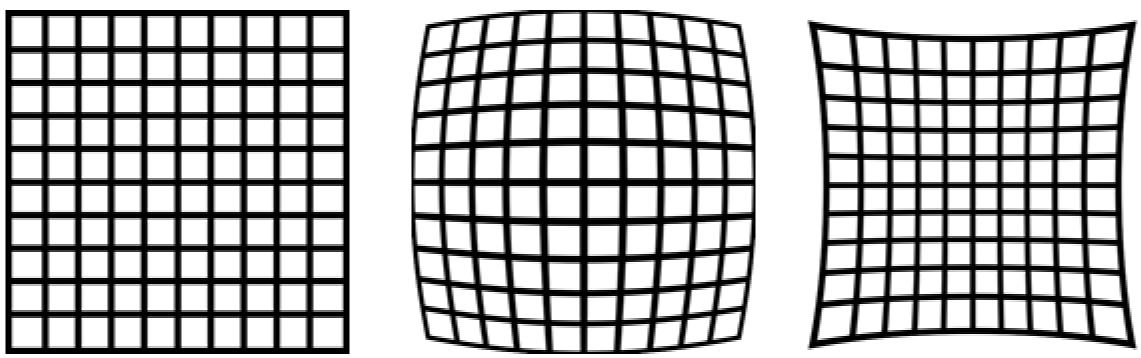

Figure 13 - Sample distortions due to lens systems, original grid (left), barrel distortion (centre), pincushion distortion (right)

2.3.2 Astigmatism

Astigmatism is caused by the lens focusing vertical lines and horizontal lines at different distances. The result is that a point source will appear to be elliptical rather than circular on the imaging plane. The aberration is not present at the centre of the field of view and increases as you move away from the centre [49] [50].

2.3.3 Field Curvature

Field Curvature is caused by the curved lens focusing light onto the flat plane of a digital image sensor [50] [49]. This causes rays that are away from the centre of the field of view to come into focus in front to the image sensor resulting in the image having an elliptical deformation which can decrease the accuracy of the centroiding operation. The aberration is not present at the centre of the field of view and increases with the field of view.

2.3.4 Lens Coma

Coma is an aberration due to imperfections in the lens which results in point sources that are not in the centre of the Field Of View being distorted [49]. The result is that point sources appear with elongated tails with a bright head.

2.4 Hardware Selection

To choose the imager that will have the best performance on orbit a set of figures of merit must be selected which meet the restrictions of the satellite. This requires examining the characteristics of camera modules which are commonly presented on datasheets that will be relevant for star imaging. These include: Signal to Noise Ratio (SNR), Dynamic Range, sensitivity, Field of View (FOV), pixel size, power requirement, resolution and operational temperature range. Many of these values are inter-related and are based on the operations and noise sources outlined previously.

Pixel size is the area that each pixel takes up including its electronics which is typically dependent on sensor resolution. As pixel size decreases it has been shown that the minimum luminance required to create an equivalent SNR increases [51]. Larger pixels therefore require fewer incident photons to create the same SNR. This increases the likelihood of the signal of faint objects being detected above the noise, allowing for the imaging of higher magnitude stars.

Signal to Noise ratio is important in poorly lit situations as it is the ratio of the incoming signal of the image that you are taking to the Root Mean Square (RMS) noise that is always present [52]. The higher the ratio the better the image quality will be. This is also a way of representing the minimum detectable signal with higher SNRs allowing for the imaging of dimmer objects.

Dynamic Range is the ratio of the brightest signal to the faintest signal over which the response of the imager is a constant [52]. This is important in situations where there are some bright and some dim or faint objects being imaged. The larger this value the clearer images will be when there are both bright and dim objects in view.

The sensitivity of the imager in Volts/Lux second is the signal produced if the imager was exposed to a light source of 1 Lux for 1 second. The higher this value the more responsive the imager will be, as a dimmer source will produce a larger signal which will have a higher SNR. This depends on the Noise Equivalent Illuminance of the sensor which is the signal illuminace that produces a SNR of one with an integration time of half a second.

The Field Of View (FOV) contributes to determining the sky coverage and the performance of the camera. Most commercial-off-the-shelf cameras that have been used on other CubeSat missions have very wide FOVs that are meant for Earth imaging. For the purpose of a star tracker a narrower field of view is preferable in order to limit the angular range of the image. This helps limit the effects of aberrations, many of which increase quadratically with FOV. Furthermore with larger FOVs the area of the sky represented by each pixel increases greatly which decreases the potential accuracy of the sensor when locating the centre of a star. Most cameras come with standard mounts which allow for the exchange of standard lenses.

Meeting the restrictions on a nanosatellites power and mass budget are also important characteristics to consider in selecting a camera module. It is preferable to use as little power as possible and at a voltage commonly found on nanosatellites - 3.3 or 5 volts. Higher voltages require additional electronics to convert the voltage which adds components and inefficiencies.

Temperature changes experienced on orbit can range from -40°C to +60°C for a high inclination low Earth orbit. With the use of COTS components the performance of the camera has not been characterized for the space environment and therefore the expected operational temperature range should be maximized.

The output format of data from the imager and the interface which is used to communicate with the sensor must also be considered. For performing star tracking raw image data is preferred due to the simplicity of being able to read each pixel value easily. The interface for communicating should be simple to allow for easy and rapid development. A number of commercially available camera modules were considered and the relevant characteristics are listed in Table 4 below.

Table 4 – List of commercial camera characteristics. All cameras have resolution of 640x480 pixels

	Pixel size(μm)	SNR(dB)	Dynamic Range(dB)	Sensitivity (V/Lux*s)	Power(mA)	FOV(°)	Temperature Range (°C)	Mass (g)	Output Format	Interface
CoMedia C328 [53]	5.6x5.6	46	62	3	60 @ 3.3V	N/A	-20 - +60	10	JPEG RAW	UART
OVM7692 [54]	1.75x1.75	38	66	0.96	120 @ 2.8V	64	-30 - +70	N/A	RAW	SCCB Parallel Serial
Saelig μcam [55]	5.6x5.6	45	60	3	62 @ 3.3V	N/A	-15 - +70	10	JPEG RAW	UART
Quasar C3188a [56]	7.6x7.6	>48	>72	2.5	<120 @ 5V	82	0-40	N/A	RAW	TWI Parallel
OVM7690 [57]	1.75x1.75	38	66	0.96	100 @ 3V	64	-30 - +70	N/A	RAW	SCCB Parallel
Videology 24B752XA [58]	6x6	N/A	55	4.8	77 @ 5V	N/A	-40 - +85	14	RAW	TWI LVDS Parallel

2.4.1 Selected Imager

The Videology 24B752XA camera was selected due to its superior sensitivity and a greater operational temperature range and can be seen in Figure 14. The OVM cameras both possess very low sensitivity due to small pixel size, while the remaining cameras that were not chosen have smaller operational temperature ranges which pose a risk for operating on orbit.

The Videology camera uses an Aptina MT9V022 monochrome image sensor with a resolution of 752x480 pixels. Its board is 29mmx29mm and comes with a metal type S lens mount. A metal lens mount is important as plastic would outgas in a vacuum and could potentially damage components including the optics of the lens. The image sensor also supports windowing as well as pixel binning. Pixel binning is done by taking a group of 4 or 16 pixels and averaging their values, reducing the resolution while increasing the SNR. Pixel data can be read from the pixels in either 10 bit linear mode, or 12 to 10 bit companding. Companding is a process by which quantization levels are made non-linear to increase the range of incoming signals that can be read.

The Videology camera is controlled through a TWI interface; this is used to change the settings on the camera such as resolution, automatic camera settings and which output method is used. The image data is output in a raw format via either the Low-Voltage Differential Signal interface or a 10 bit parallel interface.

Figure 14 - Videology 24B752XA Camera Module without lens mount. Image Credit: [58]

2.4.2 Automatic Camera Settings

The Videology camera has a number of automatic settings designed to produce a usable image under various conditions; these include Automatic Gain Control (AGC), Black Level Control (BLC), and Automatic Exposure Control (AEC).

The exposure time of an image is important as it determines the amount of time that the sensor will be collecting photons before being read out. For star imaging this has an increased importance due to the low levels of incident light that the sensor will be exposed to. The selected camera has an automatic exposure control that determines the exposure settings for each image taken by the camera. This is done by reading out the pixels in blocks before an image is taken and determining the mean and peak luminance of each block, then comparing the values in sequential readouts and determining the best exposure time to use the full dynamic range of the camera [43]. Due to the low light level when imaging stars this can result in the sensor being over-exposed, raising the noise floor which eliminates low level signals from the image data. Therefore it is preferable to turn off the AEC and manually set the exposure time to ensure that extremely long exposures are not used.

Automatic Black Level Correction is performed to determine what an un-illuminated, or dark, pixel should look like in an image. It is typically done on the sensor by having several rows of pixels that are optically dark and do not get illuminated. When an image is taken these pixels are read out and their value is determined to be what an un-illuminated pixel should return [43]. In a low-light application like star tracking these pixels can become dominated by noise in long exposures which can cause misrepresentation of black pixels in the produced image. Therefore long exposures should be avoided to reduce the misrepresentation of pixels.

Automatic Gain Control is used to boost signal levels in low-light images so that a picture is usable. When low signal levels are detected the automatic gain control is turned on and adjusts the gains of the ADCs on the sensor to boost the signal level. As this is done on the pixel level the noise is also amplified, producing images in which low level signals are lost in the noise.

2.4.3 Lens Selection

The lens is an important part of the imaging system as it must capture the incoming light and focus it onto the focal plane of the sensor. For use as a star imager it is important that the lens have the fewest aberrations possible so that it will preserve the stars shape and location. It is also preferable to find a lens with the lowest f-number possible as the brightness at the image sensor with respect to the brightness of the imaged object decreases with the square of the f-number. The f-number is the ratio of the focal length to the entrance diameter [52].

Any lens considered should use an S-mount as this is the mount type used on the selected camera. The lens barrel and optical element should be made of metal and glass respectively as plastic components will outgas onto the optics in the space environment which will decrease the image quality. Due to the restrictions on size for nanosatellites a custom lens design was not considered as the limit on design parameters restrict the design space greatly. Lastly only fixed focus lens were selected as the lens will need to remain at the same focal length while on orbit. Using these guidelines a number of COTS lenses were examined in Table 5.

Table 5 - COTS lens characteristics

	Focal Length (mm)	F-Number	Distortion (%)	Mass(g)	FOV (°)	MTF (lp/mm @ 20% contrast)	Lens Length to focal plane (mm)
Infinite Conjugate µvideo lens [59]	3.66	2.5	-42	4	82.5	150	19.01
	4.4	1.9	-26	7	65.8	123	30.26
	6.4	1.9	-11	7	43.7	127	39.78
	7.2	1.8	-8	5	39.2	106	30.43
	8.0[1]	2.5	-10	5	46	150	23.63
High Resolution Miniature Lens [60]	3.0	2.0	-55	5.9	126.0	N/A	20.4
	4.3	1.8	-55	5.9	83.1	N/A	21.6
	5.6	2.0	-15.5	4.0	65.3	N/A	25.2
	8.0	2.0	-4.6	6	43.0	N/A	19.9
Miniature CMOS Lens [61]	3.9	2.8	-29	N/A	95	N/A	20.35
	5.7	1.59	-7	N/A	56	N/A	15.53
	7.5[2]	2.8	-2	N/A	55	145[3]	11.3

The 7.2mm Infinite Conjugate µvideo lens from Edmund Optics was selected, shown in Figure 15, due to the combination of having a low F-Number, low distortion and a lower FOV. An additional benefit to the Edmund Optics lens is that it is designed for use in an infinite conjugate system. When imaging stars the light that comes in is

[1] Values for this lens are given for a ½" format sensor
[2] Values for this lens are given for a 1/2.5" format sensor
[3] Value given for MTF @ 32% contrast

collimated as it is from a source an infinite distance away. This results in the light rays coming in parallel to each other. An infinite conjugate system is where either the image plane or the object plane are located an infinite distance from the lens system [52]. Typically these systems use plano-convex/concave lens while a finite conjugate system uses bi-convex lenses [62].

Figure 15 - Edmund Optics 7.2mm Infinite Conjugate lens

Chapter 3 Expected Sky Coverage Simulation

Critical to determining the potential viability of low cost CMOS imagers as star trackers is determining the required sky coverage and expected performance gain. A simulation in MATLAB was developed to calculate the expected sky coverage with multiple variables. This involved changing the minimum brightness of stars visible as well as the FOV of the camera which are the principle drivers of sky coverage.

3.1 Simulation Definition

The first component of the simulation which must be determined is to define what constitutes sky coverage. In the context of a star tracker, sky coverage refers to whether or not enough stars are visible in the Field of View for the star tracker to determine the pointing direction of the sensor. This is driven by the expected algorithms that are used for star tracking. Many algorithms use star triads to determine the pointing direction, these usually require a minimum of three stars. Therefore the simulation defines star tracking as being possible whenever 3 or more stars are visible. A secondary objective of imaging stars for the purpose of outreach only requires the imager to be capable of seeing some stars; in this case any time that a star is visible constitutes sky coverage.

3.1.1 Algorithm Selection

In order to accurately simulate the celestial sphere the simulation looks at all parts of the sky. However, to look at every part of the sky requires examining an infinite number of possible directions in which the sensor could be facing. Therefore an algorithm is chosen which can approximate searching the entire celestial sphere. A common algorithm used for such problems is the Monte Carlo method which utilizes repeated sampling of a search space in a random way to produce numerical results.

3.1.2 Monte Carlo Method

The Monte Carlo Method uses stochastically generated numbers as inputs to a system to produce a probabilistic solution [63]. There are four steps that most Monte Carlo algorithms share:

1. Select inputs to the system and set limits
2. Randomly generate inputs, random generation can be weighted
3. Use inputs to solve a deterministic system
4. Collect results from multiple iterations for probabilistic solution

Using this information, it was decided that on each iteration a random Right Ascension (RA), Declination (DEC), and Orientation Angle (OA) for the FOV are produced. These three variables define the FOV direction for this simulation. When producing random coordinates in the Spherical coordinate system it is important to ensure that the spatial distribution of points is uniform across all areas of the sphere. Essentially at higher declinations there need to be fewer points to avoid bunching near the poles which will introduce a bias into the results. The equations used to generate the values are given below:

$$RA = 360 * u$$

$$Dec = (\cos^{-1}(2 * v - 1)) - 90$$

$$\mathrm{OA} = \mathrm{w} * 180$$

$$where\ u, v, and\ w\ are\ randomly\ generated\ values\ = [0,1]$$

The above equations generate a camera bore sight angle for each iteration of the simulation. To simplify the simulation, each time a camera bore sight is generated the sky coverage is calculated for different Fields of View and for different stellar magnitudes. The diagonal size of the FOV is changed from 20°-40° in intervals of 2°. This is to determine the point at which increasing the FOV yields diminishing returns for sky coverage. For each FOV the simulation then determines the sky coverage based on the sensor being capable of detecting different stellar magnitudes. This is done to determine the sky coverage for different levels of sensitivity of imager and for different FOVs for the lens. Sensors with a minimum detectable brightness of stellar magnitude 3, 4, and 5 are simulated for.

Lastly because this is a Monte Carlo Method the number of iterations that are run is important for ensuring that there is no bias in the randomly generated FOV directions. To determine the number of runs to be used the random generator was run for a varying number of runs and then the produced points were plotted. It was found that one million iterations produces an appropriately spread out random point generation so that no area of the sky would be sampled a statistically fewer number of times than any other area of the sky.

3.2 Simulation Method

There are 4 steps involved in the simulation method.

1. Generate random boresight and rotation angles
2. Rotate star field by the boresight angles to the x axis
3. Determine sky coverage for different magnitudes and different field of views
4. Rotate star field back to original configuration using boresight angles

The simulation uses the Monte Carlo method to produce a series of camera bore sight angles, as well as an orientation angle for the rectangular FOV. Of importance to the simulation is the coordinate system used to define these generated angles as well as their relationship to the star locations provided in the Bright Star Catalogue [64]. The star catalogue is provided in the Earth Centered Inertial Frame with J2000 coordinates. The Earth Centered Inertial Frame (ECIF) has its origin at the centre of mass of Earth, its x-axis points in the direction of the mean vernal equinox, the z-axis points to the North Celestial Pole and the y-axis completes the right handed system [65]. In this case the J2000 coordinates means that the directions for the equinox and the North Celestial Pole are defined at midnight January 1 2000.

The other system that was considered is the Earth Centred Earth Fixed (ECEF) system. In this case the z-axis is aligned with the International Reference Pole (IRP) and the x-axis is aligned with the International Reference Meridian (IRM) and the y-axis again completes the right handed system [65]. Due to the x-axis being defined along the IRM the x-axis is rotating along with the Earth. This system is ill-suited for use with systems that are imaging inertially fixed targets since their coordinates will be dependent on the current epoch which complicates calculations. For this reason the ECIF system is chosen, this provides the simulation with static coordinates for the stars which simplifies the visibility determination process.

In order to limit the number of computations required by each iteration of the simulation the stars are sorted into a number of variables each holding one magnitude of brightness. When checking star locations later this ensures that a star is not checked more than once when the algorithm searches for stars of varying brightness.

On each iteration of the simulation, 3 random variables are generated: a Right Ascension which is the angle measured counter-clockwise from the positive x-axis in the x-y plane, a Declination which is the angle measured counter-clockwise from the x-y plane, and an Orientation Angle which is the rotational angle around the simulated bore sight where 0° follows a small circle parallel to the x-y plane.

With the RA and DEC it is possible to determine the area of the sky that is visible to the camera given that the size of the FOV is also given. Typically lenses used in imaging systems are circular, this is for two reasons. The first is that circular lenses are much easier to make and calibrate, especially in more complex multi-lens systems. The second reason is that when using a rectangular lens with a rectangular image sensor, the lens would have to be precisely centred to ensure that the entire sensor is illuminated; with a circular lens the margin for error is greater since the circular lens projects onto an area around the sensor as seen in Figure 16. The drawback is that the entire FOV of the lens is not utilized as some tolerance must be left towards the corners of the sensor area.

Therefore the FOV used in the model will be rectangular as well to ensure the affinity to a real sensor.

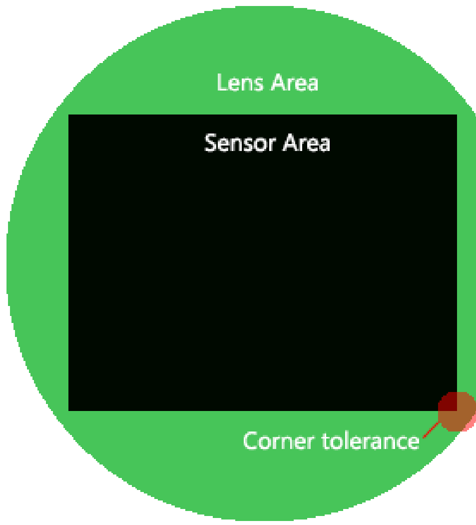

Figure 16 - Rectangular sensor area compared to circular lens area.

This introduces some complexities into the simulation due to the fact that the star positions are given in the spherical coordinate system. A way to project the rectangular FOV onto the spherical surface where the stars are is required. This is non-trivial because a rectangular FOV will always see the same solid angle of the sky, however, as declination increases or decreases the amount of sky in spherical coordinates that it sees will change. For example at the equator a diagonal FOV of 36° produces a horizontal FOV of 28.8°, meaning that in the horizontal direction the camera sees 28.8° wide or 1/25 of the entire circumference of the sky, when coupled with a 4:3 aspect ratio sensor. However, at a declination of 45° the same sensor and FOV will still see 28.8° wide but the circumference of the sky that it will image will be 40° or 1/9 of the total circumference of the coordinate system as seen in Figure 17.

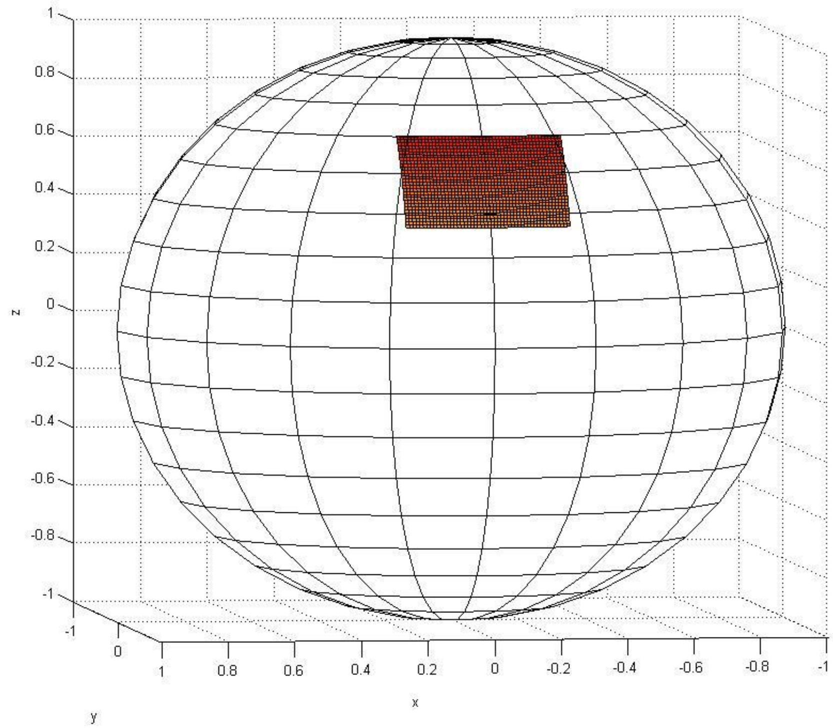

Figure 17 - Rectangular FOV on a sphere

To get around this, the star positions are calculated in Cartesian XYZ coordinate system during the sorting stage using the equations below. These coordinates are calculated assuming a unit sphere can be used to represent the distances of each star since they are considered to be at infinite distance. This is done because a Cartesian coordinate system is not subject to the numerical distortion that the spherical coordinates are as you approach the poles.

$$x = \cos(declination) * \cos(Right\ Ascension)$$

$$y = \cos(declination) * \sin(Right\ Ascension)$$

$$z = \sin(declination)$$

The FOV visible by the camera is then computed in Cartesian coordinates when the boresight is aligned to the x axis to simplify the simulation. The FOV is originally given as a diagonal value in degrees, which is then converted into a horizontal and vertical component using the known aspect ratio of the image sensor using the following equation.

$$HFOV = FOV * \frac{640}{800}$$

$$VFOV = FOV * \frac{480}{800}$$

With these values the boundary conditions of the FOV is calculated in Cartesian coordinates. Again assuming a unit sphere the boundary conditions are then calculated as follows

$$x = \cos\left(\pm\frac{HFOV}{2}\right)$$

$$y = \sin\left(\pm\frac{HFOV}{2}\right)$$

$$z = \cos\left(\pm\frac{VFOV}{2}\right)$$

In the above equations the x and y calculations are performed using a Declination and Right Ascension of 0°, this eliminates the distortion present at high declinations, this is possible because the values are just used as boundary conditions. These boundary conditions provide six corners from which a cube is constructed whose contents represent the visible sky.

The final variable used in the simulation is the orientation of the FOV. This is defined as the angle between the cameras horizontal and the small circle at the given declination. This again is non-trivial due to the rectangular FOV being used. If the FOV is simply rotated then the boundary conditions previously calculated are no longer useful. This is because as you travel along one of the vertices of the cube, if it has been rotated, there will be more than one changing variable. The vertices are no longer represented by a single number then but as a function of multiple variables. This greatly increases the computational complexity of the lookup algorithm. Therefore it was decided to simply rotate the star field around the boresight by the FOV orientation angle. To do this a number of rotations are required using the standard cosine rotation matrix.

$$R_x(\theta) = \begin{bmatrix} 1 & 0 & 0 \\ 0 & \cos\theta & -\sin\theta \\ 0 & \sin\theta & \cos\theta \end{bmatrix}$$

$$R_y(\varphi) = \begin{bmatrix} \cos\varphi & 0 & \sin\varphi \\ 0 & 1 & 0 \\ -\sin\varphi & 0 & \cos\varphi \end{bmatrix}$$

$$R_z(\gamma) = \begin{bmatrix} \cos\gamma & -\sin\gamma & 0 \\ \sin\gamma & \cos\gamma & 0 \\ 0 & 0 & 1 \end{bmatrix}$$

To do this a total of 3 rotations are required and are executed in the following order:

1. Rotation about the z-axis by the RA of the boresight
2. Rotation about the y-axis by the DEC of the boresight
3. Rotation about the x-axis by the OA

When determining if a star is in the FOV of the camera its Cartesian coordinates are compared against the Cartesian coordinates of the boundary conditions of the FOV. If the star is within the x, y and z boundaries then it is recorded as visible. The total number of visible stars is then counted and stored. Once each star has been checked to see if it is in view the star field must be rotated back to the original orientation for the next step in the Monte Carlo simulation. This is done by performing the above 3 rotations in reverse order and with the reverse angles.

3.3 Simulation Results

The simulation results can be viewed in two main parts. The first looking at how the coverage changes with respect to sensor sensitivity and the second with how the coverage changes with respect to FOV. These two factors are the main determining factors for the simulations results. The distribution of generated Right Ascension and Declinations, as seen in Figure 18, shows there are fewer points generated at latitudes further away from the equator to prevent polar bunching of the simulated coordinates.

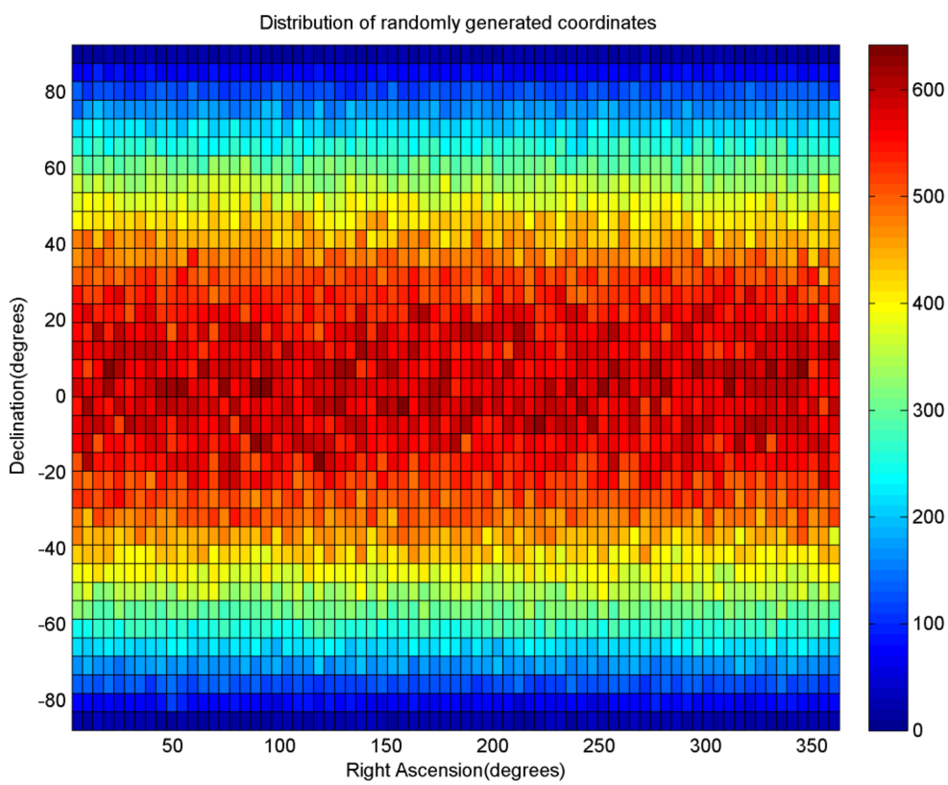

Figure 18 - Distribution of randomly generated coordinates

First the sky coverage was plotted against the varying FOV for each different minimum brightness level that was simulated. Before we examine the results it is worth pointing out that as FOV increases the amount of sky that an individual pixel views also increases. This is a limiting factor for the accuracy of a centroiding algorithm which depends on the size of the pixel and the area of the sky that is visible. The plot can be seen below in Figure 19.

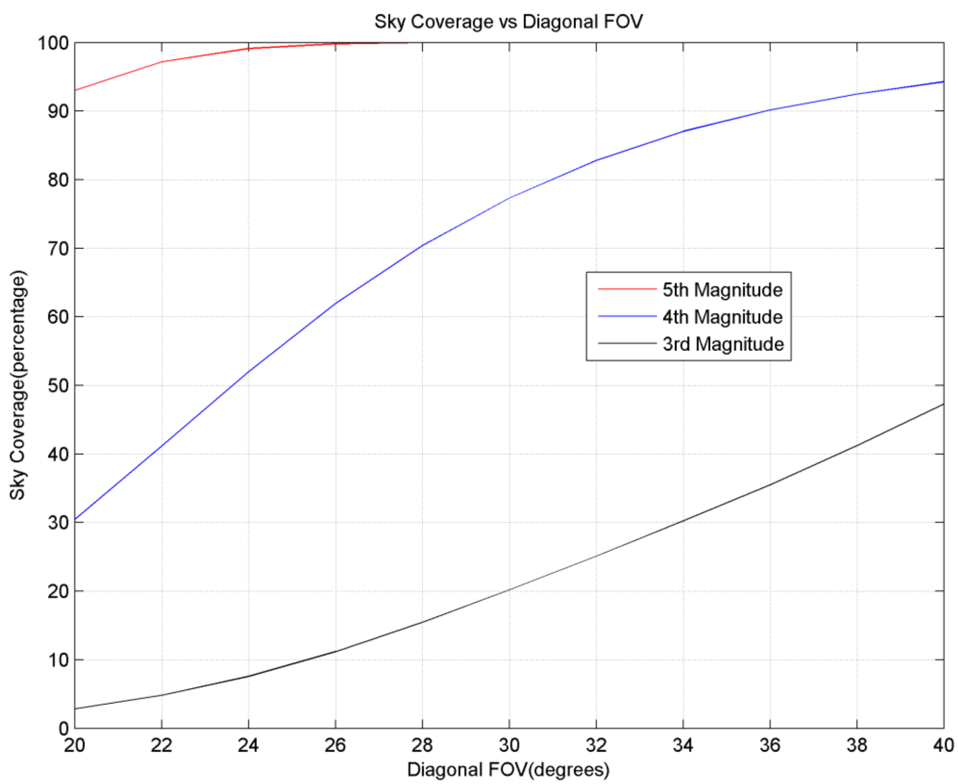

Figure 19 - Sky coverage vs. diagonal FOV

From the above plot it is clear that the sky coverage trends differently as FOV increases depending on the minimum detectable brightness for the sensor. When the sensor can only detect 3rd magnitude and lower stars the sky coverage will increase at an increasing rate with FOV. This suggests that for sensors that have a low minimum detectable brightness it is beneficial to increase the FOV.

For 4th magnitude and lower the sky coverage increases nearly linearly until around 28° at which point increasing the FOV produces less gain in sky coverage each successive time. Therefore for a sensor capable of viewing 4th magnitude stars a FOV around 30° is likely all that is required.

For 5th magnitude and lower the sky coverage even for 20° FOV is greater than 90% and for 26° FOV a sky coverage of 100% can be attained. Therefore a FOV greater than 20° can only increase the sky coverage by a small amount while decreasing the accuracy of the centroiding algorithm.

With the application of a star tracker with respect to this thesis being restricted to that of nanosatellites it is reasonable to assume that a small low power sensor with low sensitivity is likely to be used. For this reason it is likely that for a small satellite a large FOV is desirable so that the 3rd magnitude sky coverage is greater.

The number of stars visible at any given time is seen in Figure 20 for 3rd, Figure 21 for 4th and Figure 22 for 5th magnitude stars where the diagonal FOV is 30°. What becomes clear from the plots is the gain in sky coverage that is made in increasing the sensitivity of the sensor. When the sensitivity of the sensor increases from 3rd to 4th magnitude stars the sky coverage increases from 20.21% to 77.33%. Furthermore if the camera is being used only for star imaging, where only a single star needs to be visible, then the sky coverage increases to 97.15% from just 74.96%. For 5th magnitude stars it is immediately apparent that sky coverage is near unity at 99.997% with a 30° FOV and for use as simply a star imager coverage is complete as there are always at least 2 stars visible. The ability to construct multiple triads can also help increase the accuracy of a star tracker, therefore the more stars that are visible in any image, the greater the certainty with which the attitude can be determined. Therefore coverage with 6 or more stars visible can be very valuable and increase from 1.48% to 28.99% to greater than 98%.

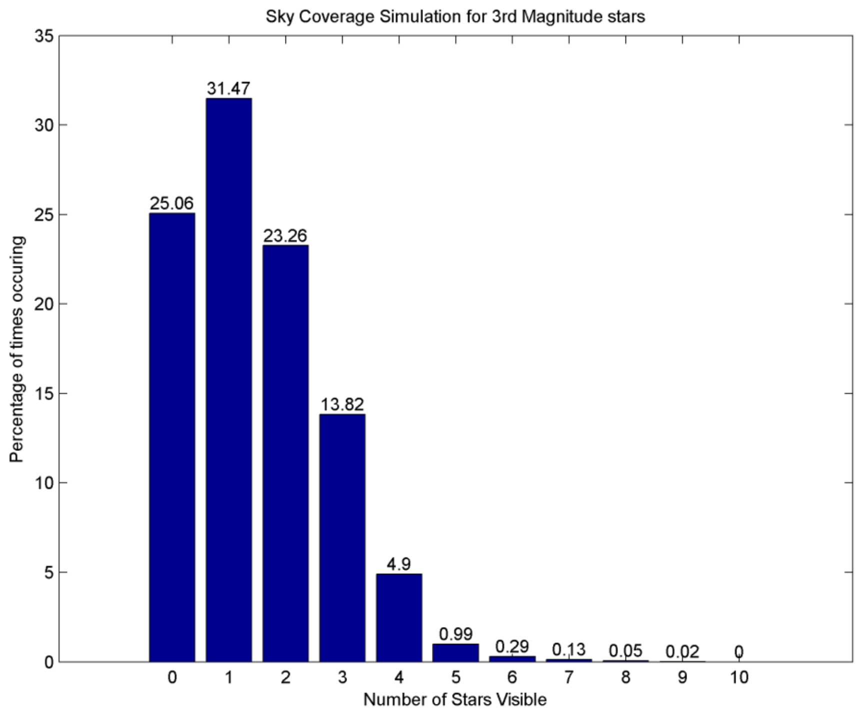

Figure 20 - Sky coverage for 3rd magnitude stars for 30° FOV

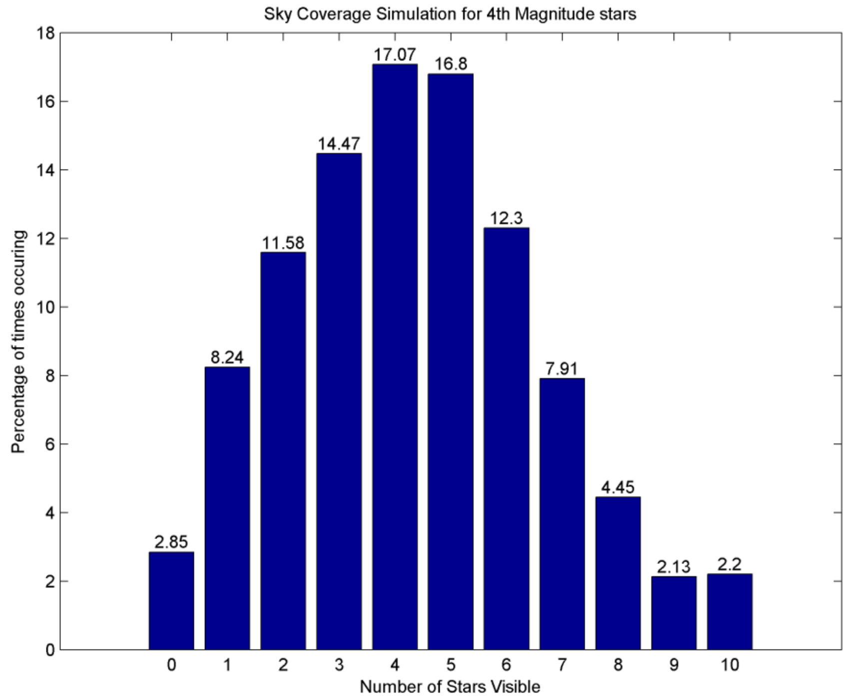

Figure 21 - Sky coverage for 4th magnitude stars for 30° FOV

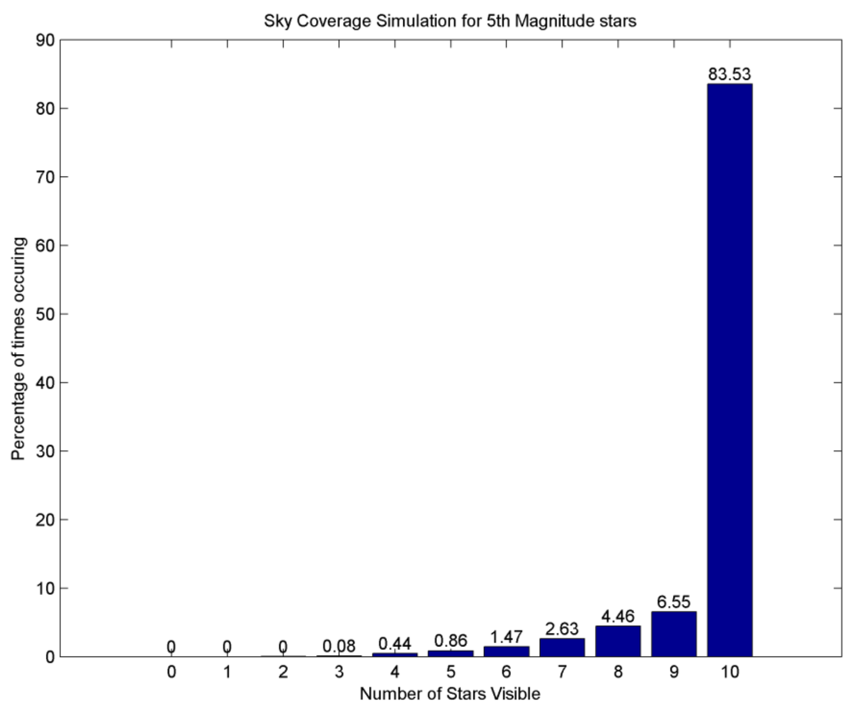

Figure 22 - Sky coverage for 5th magnitude stars for 30° FOV

3.4 Comparison to Previous Studies

Predicting sky coverage has been examined before as it is an important part of determining whether or not to add a star tracker to an attitude determination system. Most simulations use a circular FOV to determine the area of the sky that is being viewed. This is simple from a computational standpoint as only the angular distance between a boresight and a star needs to be calculated, no rotations are necessary. However, this method results in a larger FOV being simulated for than is actually seen by the sensor.

A similar simulation [27] yielded similar results as seen in Figure 23. It is important to note that the simulation below uses a circular FOV. The conversion from circular to diagonal is given by the following equation and values are given in Table 6.

$$\mathrm{CFOV} = \sqrt{\frac{48DFOV^2}{25\pi}}$$

Table 6 - Equivalent Circular FOV

Diagonal FOV (°)	Equivalent Circular (°)
20	15.64
24	18.76
28	21.89
32	25.02
36	28.14
40	31.27

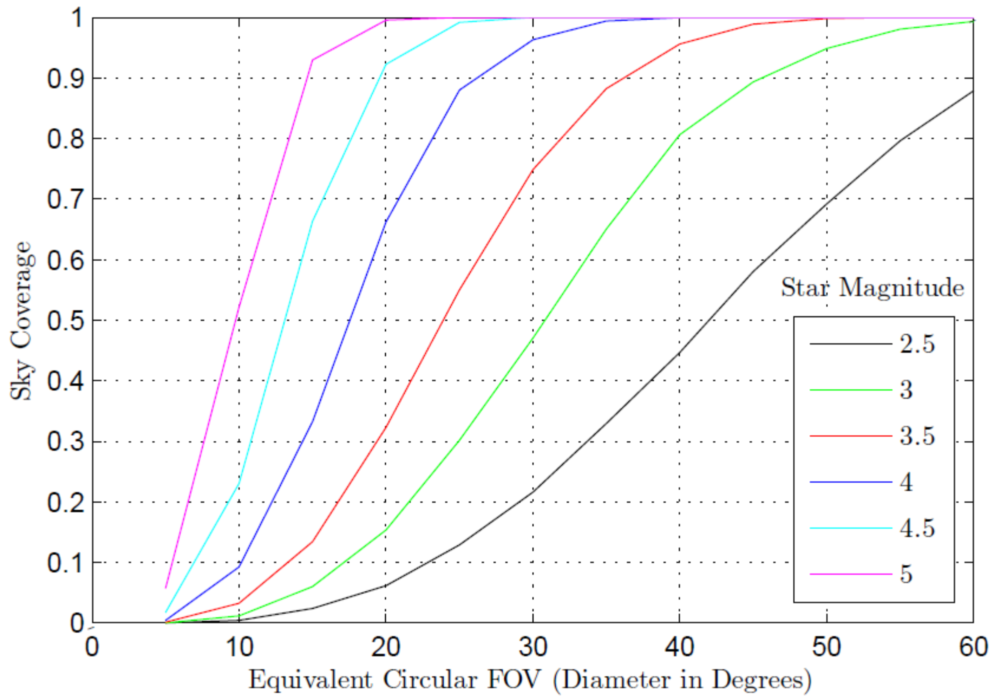

Figure 23 - FOV vs. Sky Coverage. Image Credit: [27]

A comparison shows that Figure 19 has lower sky coverage than the results shown in Figure 23. This is expected as a DFOV has a smaller area on the sky than the CFOV which will produce lower sky coverage, particularly when viewing low magnitude stars. For 3rd magnitude stars the diagonal FOV produces sky coverage 7% lower than the circular FOV. This is a significant difference, while for higher magnitude stars where coverage is already greater than 90% the difference is less pronounced.

3.5 Orbital Simulation

Systems Tool Kit® [66] (STK) is a computer program that can be used to simulate the position and attitude of a satellite on orbit and can be linked to programs such as Matlab. By integrating the sky coverage simulation with STK it is possible to determine the sky coverage experienced by a satellite with a specific orientation at specific points in its orbit. Since stars are not evenly distributed across the celestial sphere the orbital characteristics of a satellite will greatly influence the expected sky coverage as an area with many stars could be seen repeatedly or not all. For nanosatellites this effect can be very important due to the short mission durations, meaning a satellite may spend its entire operational lifetime in an area with poor sky coverage. This can be used to verify the functionality of a star tracker or aid in determining the suitability of the star tracker for a specific mission.

3.5.1 Scenario Details and Results

STK can be controlled through Matlab by opening it as a service. Matlab commands STK to create a scenario with a time period and then creates the satellite and sensor. A sample of previous nanosatellite missions was performed and it was found that the majority of missions have an altitude of 600-700km (Figure 24) and that most are in high inclination or sun-synchronous orbits. Therefore the simulation uses a 650km altitude sun-synchronous satellite with the Right Ascension of the Ascending Node, Argument of Perigee, and True Anomaly set to 0°, the scenario period is set to August 1-30 2014. The satellite is assumed to be in a nadir pointing configuration with the star tracker on the zenith face. In addition to returning the vector for the sensor, vectors for the Sun and Moon are also returned. This is to determine if either object is in the FOV of the sensor which would likely blind the sensor and prevent it from seeing any stars.

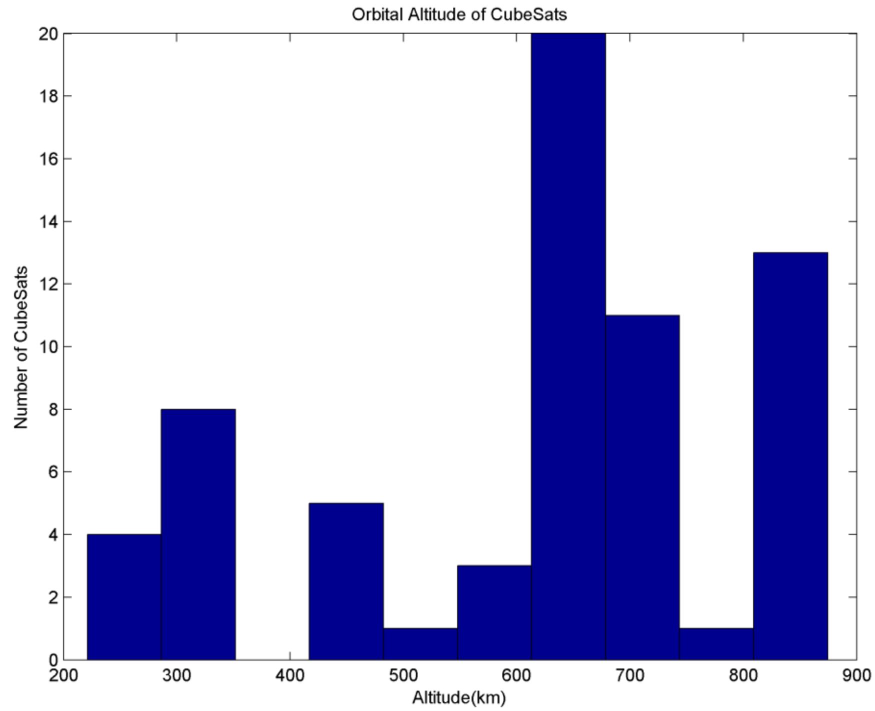

Figure 24 - Orbital altitude of CubeSats launched before April 2013

The total number of stars visible is calculated in a similar way with the exception that the number of stars visible is set to 0 when either the Sun or Moon is in the as in Figure 25.

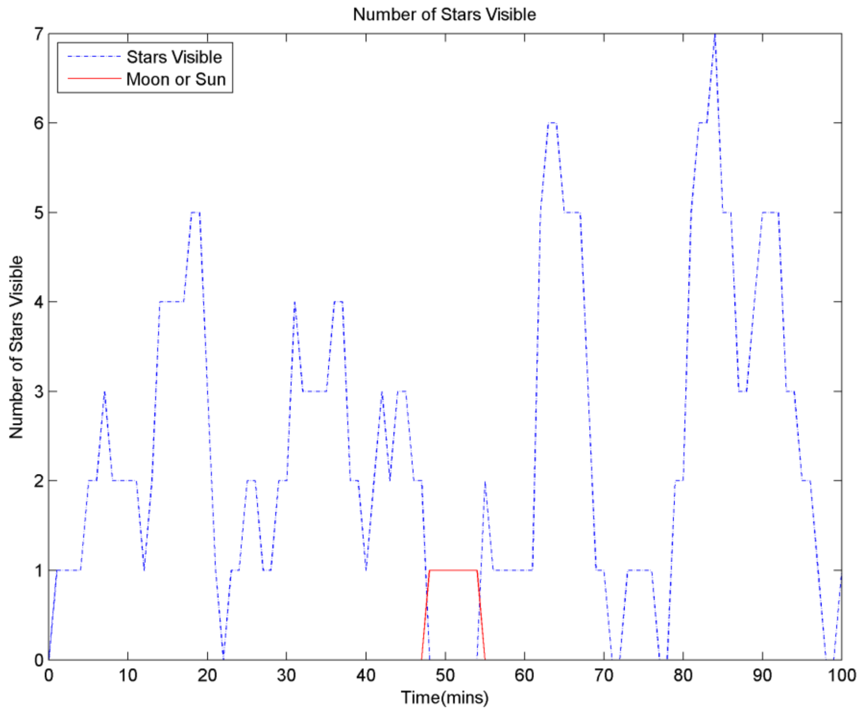

Figure 25 - 3rd magnitude stars visible and Sun and Moon visibility for FOV=40°

The simulation also shows that the sky coverage is lower when the limiting magnitude of visible stars is 4 for the month which was simulated as seen in Figure 26. For a FOV of 24° the sky coverage is 13% lower than the original simulation. This is likely due to the area of the sky which was seen by the sensor, with this particular orbit the same area of the sky was seen repeatedly, having few stars between magnitude 4 and 5. This shows the influence of the local variation of star density on the results of the simulation.

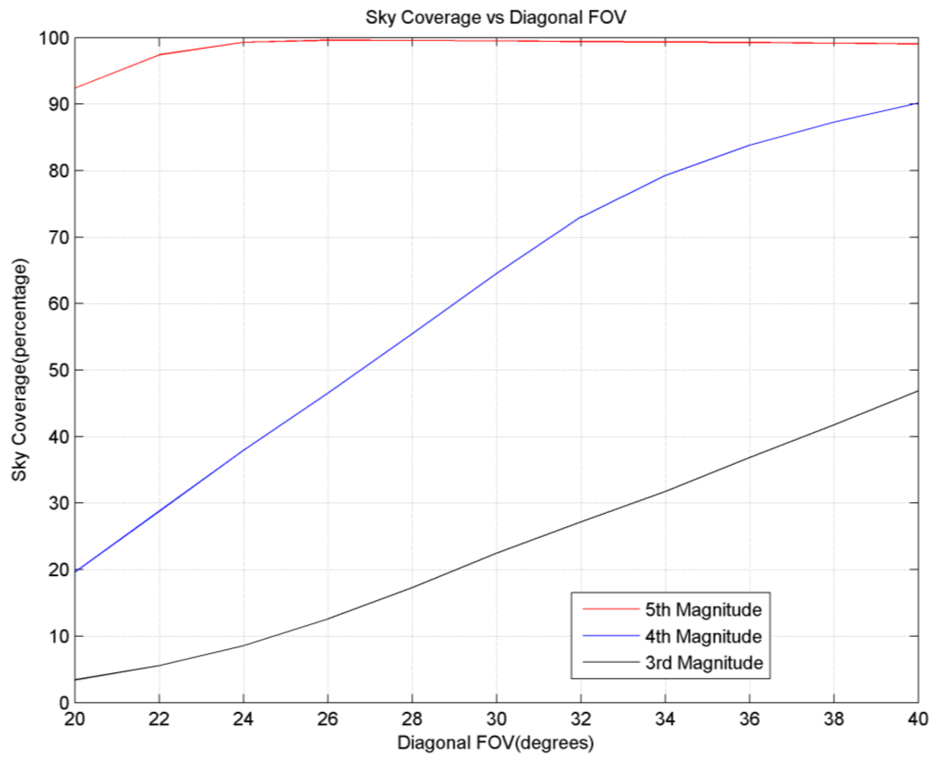

Figure 26 - Sky coverage vs. diagonal FOV for STK simulation

3.6 Summary of Sky Coverage Simulation

The sky coverage simulation was developed using a Monte Carlo algorithm to simulate the sky coverage that could be expected from a sensor with different FOVs. The simulation also takes into account the different possible orientations of the senor as well as the limiting magnitudes that the sensor can detect. A rectangular, rather than circular, FOV is used to better reflect the area of the sky that the sensor can see. When compared to similar studies using circular FOVs the expected sky coverage is, as expected, lower as a result of the smaller area of the sky that is being imaged. Integrating STK has allowed for the testing of actual orbits as a means of determining the feasibility of using a star tracker on a specific mission by determining the sky coverage that would be expected.

Chapter 4 Camera Interface Implementation

4.1 Imager Interface

The Videology 24B752XA is capable of outputting digital image data by two methods, a parallel 10 bit data output or a 12 bit serial signal. Most small satellites have a limited number of pins available on microcontrollers and on communication stacks, for this reason the serial communication is being implemented as it reduces the number of wires required from 14 to as low as 3, depending on the exact implementation. This however, adds the complication of requiring an added step to the readout where the data rate is slowed down as the output of the serial communication is too fast for a simple microcontroller. Therefore a Field Programmable Gate Array (FPGA) is used which deserializes the datastream, captures a single image and outputs it to a computer. The camera settings are controlled by a Two Wire Interface (TWI) connection, a block diagram of the system can be seen in

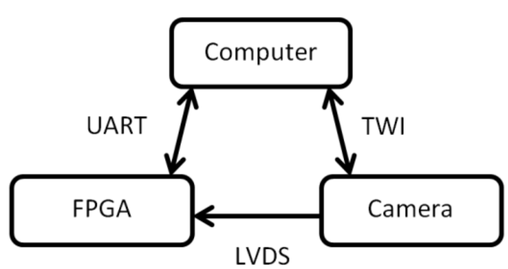

Figure 27 - Block Diagram of Imager interface

4.1.1 Camera Image Data Output

The serial communication implemented is Low-Voltage Differential Signaling (LVDS) which describes the electrical protocol of the camera output signal. LVDS uses a twisted pair to transmit data over long distances using low voltages. A typical LVDS signal is centred on 1.2V with a voltage difference between the twisted pair of only 350mV. This difference is produced by using a constant current of 3.5 mA with the direction of the current through the two wires, which are connected by a resistor at the receiver, determining the output.

The twisted pair signal allows for wire lengths of 10m with low noise effects since any effect on one wire is felt equally on the other, having no impact on the differential signal. Furthermore since a constant current is drawn the power usage circuit experiences less interference since the demand on it is always the same. LVDS is a high speed communication protocol commonly reaching speeds of 400Mbps at cable lengths of 10m [67].

The camera outputs one pixel of data each clock cycle over the LVDS line with a pixel clock of 13.5MHz. Each packet has 12 bits: a start bit, 10 pixel data bits, and a stop bit. This equates to a bit rate of 162Mbps which is too fast for most microcontrollers to handle, furthermore the non-standard 12 bit serial packet is not supported in most serial communication protocols therefore an FPGA is used to receive the LVDS signal.

4.2 FPGA Implementation

Receiving the high speed signal requires hardware dedicated to reading the incoming signal. To do this a design on an FPGA is implemented to read the incoming signal, store a picture and then output the picture at a speed a typical microcontroller can accept.

An Altera DE2-115 development board was selected to implement the FPGA design. It has a Cyclone IV EP4CE115 FPGA on it with 114 480 logic elements and 3 888 kbits of memory which is more than enough for this application [68]. Furthermore the development board also has 2Mb of SRAM for storing pictures before they are sent to a microcontroller [69]. Programming of the FPGA is done in the Quartus II environment which includes a number of features such as pre-designed functions, known as Megafunctions, for some interfaces.

The implementation on the FPGA has 5 modules: (1) LVDS Deserialization, (2) Frame Data Counting, (3) Data Buffer, (4) SRAM Data Storage and Retrieval, and (5) Image Output.

4.2.1 LVDS Deserialization

LVDS Deserialization (LD) Module requires the use of the ALTLVDS_RX Megafunction which reads in the LVDS signal at 13.5MHz clock rate which is provided to the development board from the camera. The function works as a blackbox with several parameters given, in this case the incoming clock speed as well as the deserialization factor which is 12. The function then outputs the deserialized signal to the Frame Data Counting Module. To ensure that the signal is properly aligned a data alignment signal is taken as an input from the Frame Data Counting Module. The block diagram is shown in Figure 28.

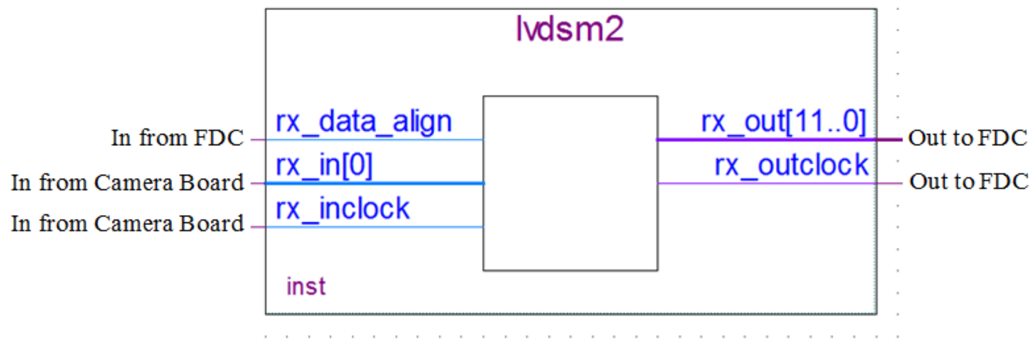

Figure 28 - LVDS Deserialization Block Diagram

4.2.2 Frame Data Counting

The Frame Data Counting (FDC) Module is implemented to find the beginning and end of a frame as well as to count the number of lines in a frame. The output of the camera's data includes blanking in both the vertical and horizontal fields to separate each line and each frame; it can be seen in Figure 30. The Frame Data Counting Module counts the number of rows to ensure that it matches the expected number that is being output for each frame. This is done using the Line and Frame Valid signals from the camera board, which are put through shift registers to ensure the timing of their signal is synchronized with the data which has gone through the LVDS Deserialization module. It also aligns the output of the LVDS Deserialization Module so that the start bit is in the first position and the stop bit is in the last position by outputting an alignment pulse that is used by the LVDS Deserialization module. It then outputs both the line count and the deserialized data, minus the start and stop bit which is shown in Figure 29.

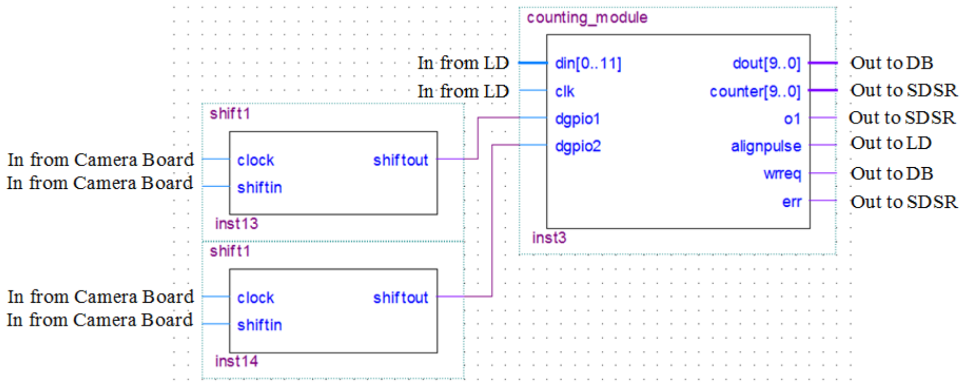

Figure 29 - Frame Data Counting Block Diagram

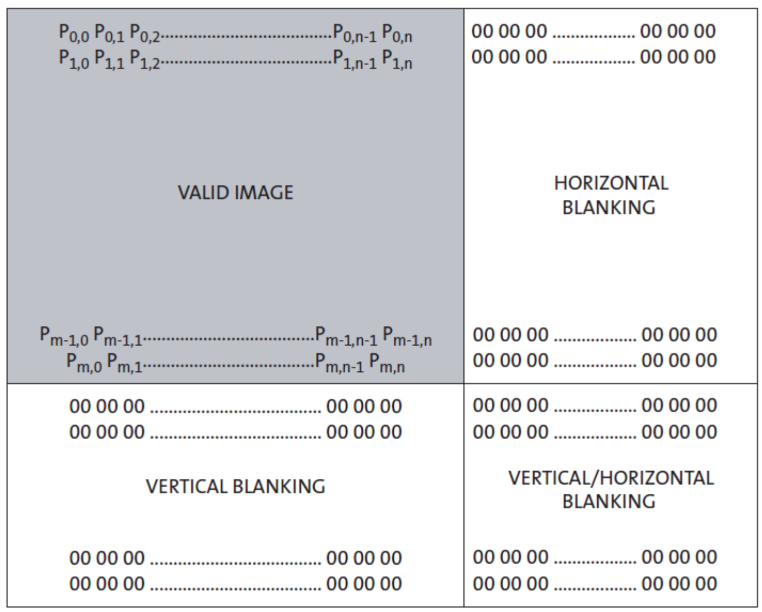

Figure 30 - Spatial Readout of Image Data. Image Credit: [70]

4.2.3 Data Buffer

The Data Buffer (DB) is designed to act as an intermediary between the FDC and the SRAM Data Storage and Retrieval Modules due to the different operational speeds that are used in each module. The FDC runs at the same speed as the incoming data from the camera, 13.5MHz while the next module runs at 50MHz. Therefore a First-In First-Out (FIFO) is implemented from a Megafunction to store data before it is sent on.

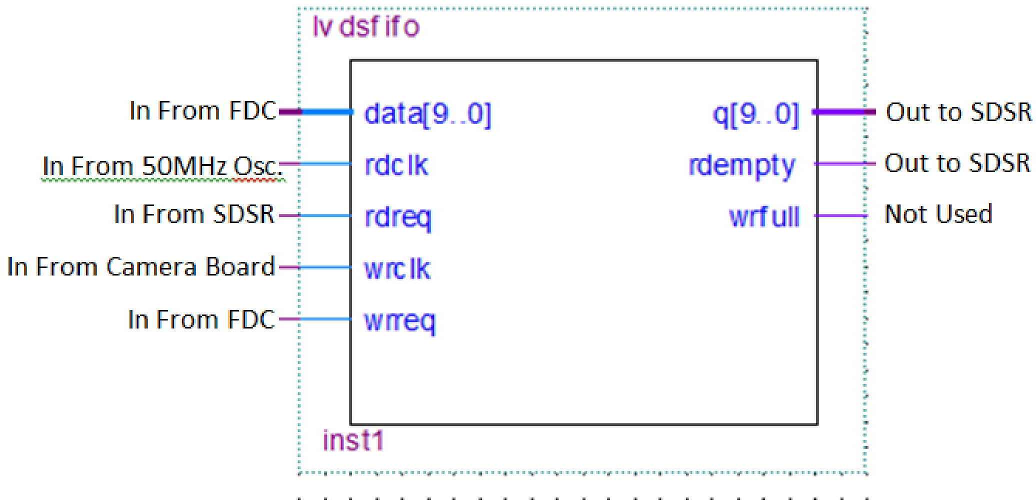

Figure 31 - Data Buffer Block Diagram

4.2.4 SRAM Data Storage and Retrieval

The SRAM Data Storage and Retrieval (SDSR) is designed to store an entire frame at a time since the FPGA does not have enough memory units on board to store an entire image at once before sending it. The SDSR uses 10 states to define its operational status at any time. The first 6 states are used for reading in an image while the last 4 are used for outputting an image and there are two state loops which are used. The block diagram and software flow diagram are in Figure 32 and Figure 33 respectively.

The first state is IDLE, which is the default state of the module. While in this state the SRAM is not enabled and is not set to receive or output any data and the address is set to 0, the start of the SRAM. The Idle state is left when it receives a command to take a picture. However, the Data Buffer is always being filled with data and therefore must be continually emptied even when no picture has been requested, otherwise the first data retrieved from the buffer would be old, therefore the Idle state as well as the WAIT FOR START state are reading from the buffer and throwing away the data.

The second state is WAIT FOR START which enables the SRAM chip and then waits for the start of the next full frame before it begins reading data from the Data Buffer. When the next full frame is ready it starts the first state loop of the SDSR.

The first state loop is composed of the DATA, INCREMENT ADDRESS WRITE and WAIT states. The DATA state is used to retrieve data from the Data Buffer and then writes the data immediately to the SRAM at the current address. The INCREMENT ADDRESS WRITE state follows the DATA state and increments the address of the SDSR, if the address is less than the size of one image it then goes to the WAIT state, otherwise it exits the state loop. The WAIT state is used to check if there is data in the Data Buffer, because the SDSR operates at a higher speed than the FDC, the Data Buffer is being emptied faster than it is being filled, if there is no data it simply loops back on itself until there is, at which time the state changes to DATA again.

The DONE CAPTURE state immediately follows the first state loop, it disables write capabilities to the SRAM and resets the address to 0; it then begins the second state loop.

The first state in the second state loop is the READ SRAM state which is used to retrieve data from the SRAM at the current address. The second state is WRITE FIFO which checks to see if the FIFO in the Image Output module is full or not. If it is full then the state waits until part of the FIFO is emptied before it writes to it and moves on to the next state. This is due again to the difference in speeds that the modules operate at, the SDSR runs at 50MHz while the Image Output module runs at just 115200kHz. The final state is the INCREMENT ADDRESS READ, this state increases the address by one and checks to see if the entire image has been read from the SRAM, if it has the state loop is exited, otherwise it returns to the READ SRAM state.

The final state is DONE OUTPUT which is right after the second state loop; it resets the SRAM address to 0 and turns off the output from the SRAM as well as shutting off the SRAM chip before returning the SDSR module to the IDLE state.

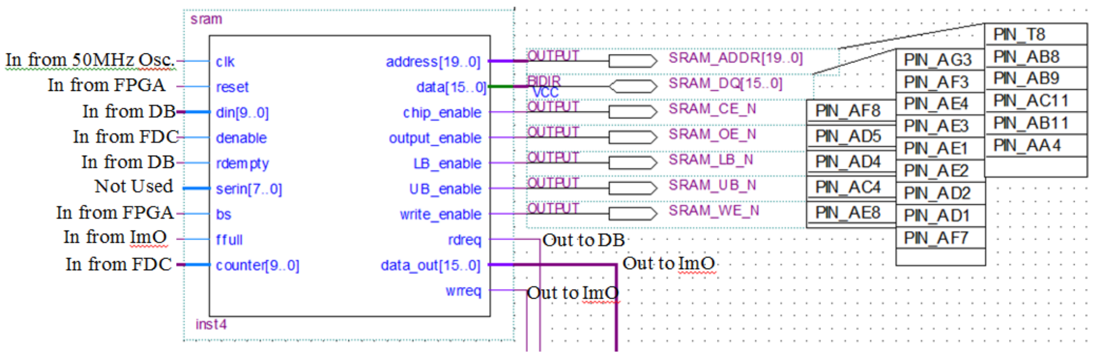

Figure 32 - SRAM Data Storage and Retrieval Block Diagram

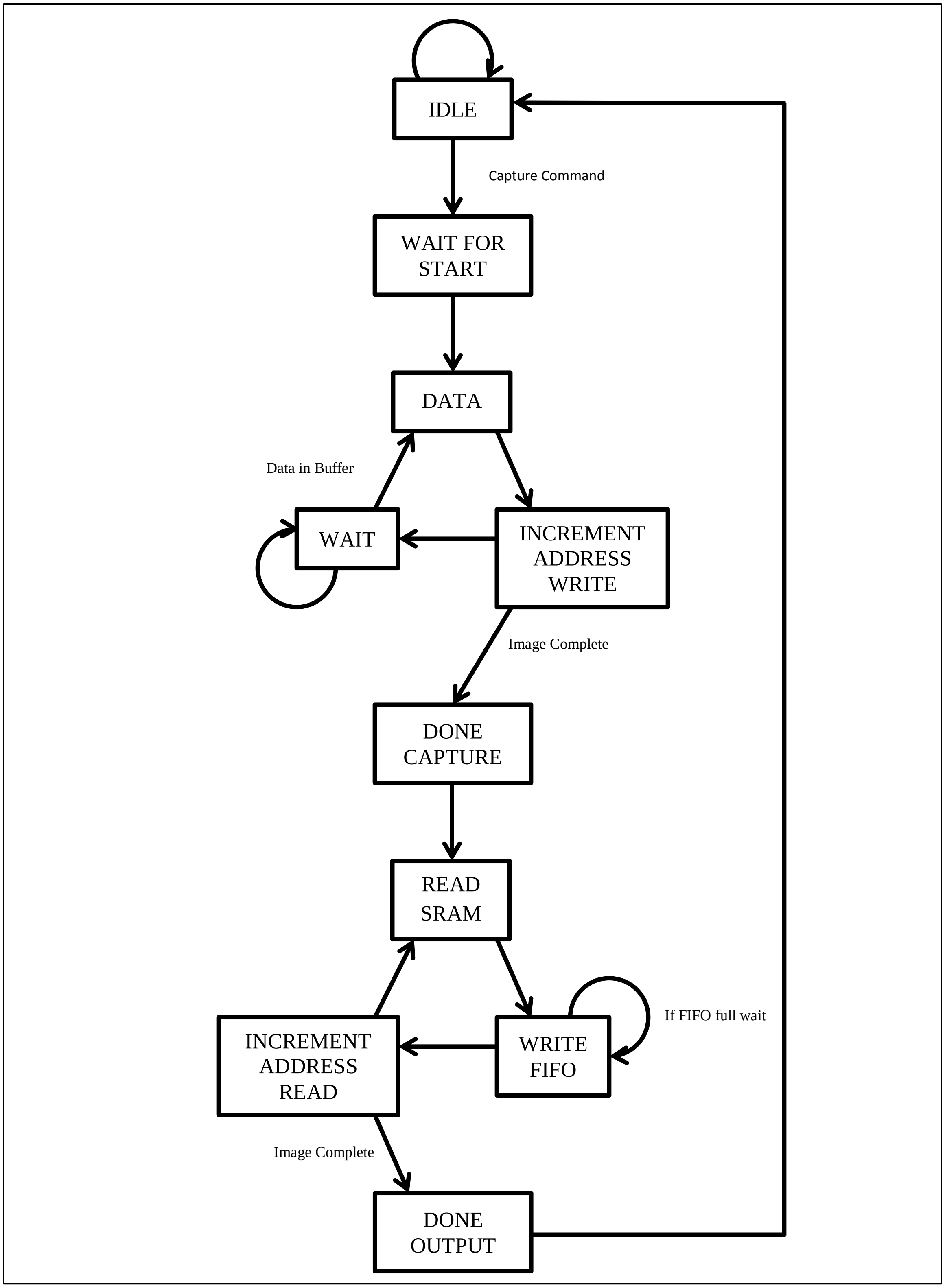

Figure 33 - SRAM Flow Diagram

4.2.5 Image Output

The Image Output (ImO) Module consists of two main parts, a buffer and a serial output module. The buffer uses a FIFO like the one used in the Data Buffer module as an intermediary step due to the SDSR module running at 50MHz while the serial output module runs at only 115200 kHz. The serial output module takes the data from the SDSR and serializes it before outputting via GPIO to the computer. The serial output module adds a start and stop bit with no parity to produce a standard UART signal. However, since the data is coming through as 10 bits and a UART only has 8 bits of payload data two separate packets must be sent for each pixel. This data is then recombined into a single value on the computer that receives the data.

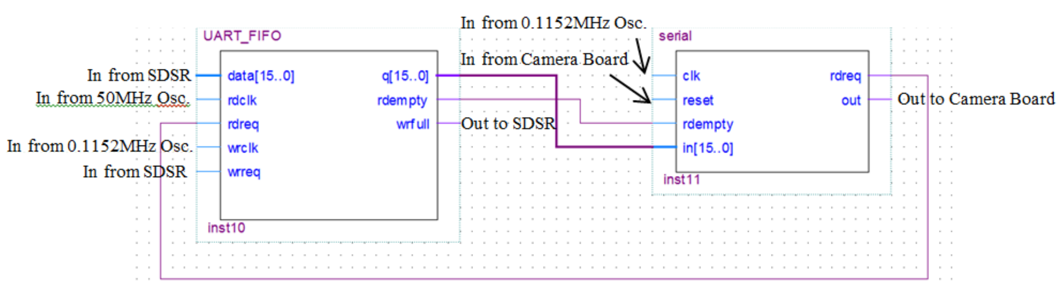

Figure 34 - Image Output Block Diagram

4.3 Camera Breakout Board Design

In order to interface the camera with the FPGA, a breakout board was designed and manufactured. The board includes an IC for converting the LVDS signal, an SMA connector for the clock signal and a 40-pin ribbon connector for connecting to the FPGA. Connections for I2C communication for programming the camera are also present. The schematic, Figure 35, and board layout, Figure 36, were completed in Eagle.

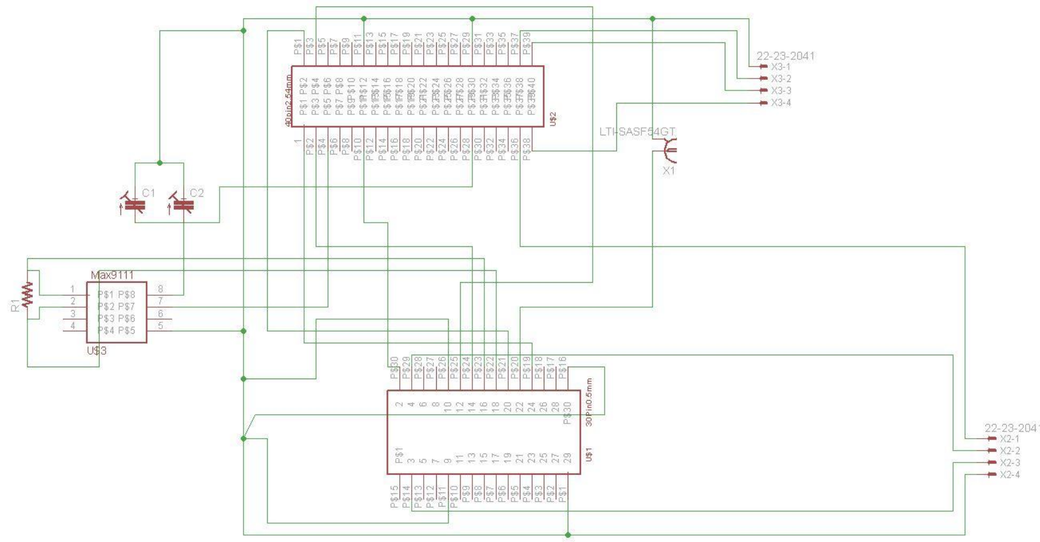

Figure 35 - Camera breakout board schematic

The camera breakout board has two layers, with the camera connector on the bottom and all connectors and components on the top side of the board. There are four mounting holes to securely connect the camera to the board as the camera connector does not have a locking mechanism.

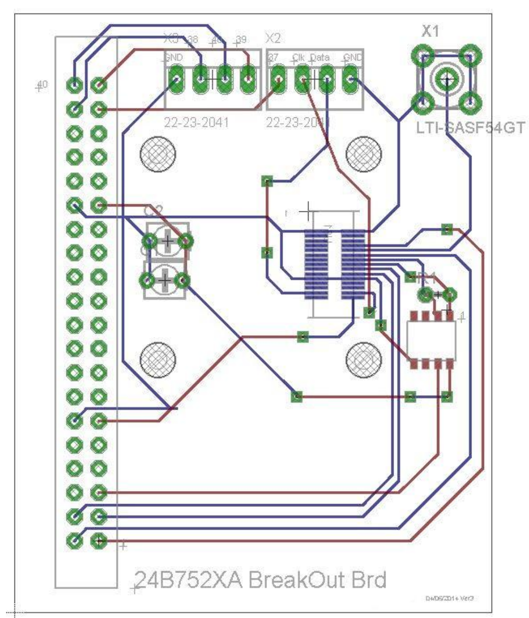

Figure 36 - Camera breakout board layout

The board uses a Max9111 single line LVDS receiver to receive the two line LVDS signal from the camera and converts the signal levels from LVDS to TTL levels for output to the FPGA board. In addition the two line differential signal is converted to a single line serial signal to limit the number of connections needed to the FPGA. The MAX9111 was chosen for its low skew, its support of up to 500Mbps signals, and its extended operational temperature range (-40°C to +85°C) which ensures operation in the expected environmental conditions [71]. The board was manufactured and can be seen in Figure 37.

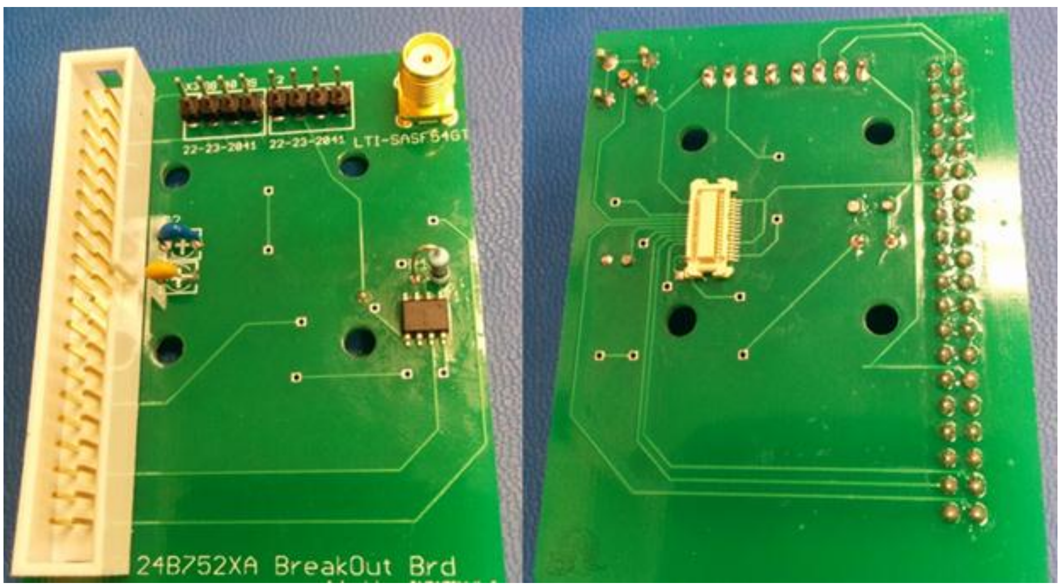

Figure 37 - Camera Breakout Board Top View (Left) and Bottom View (Right)

4.4 Environmental Testing

The space environment introduces factors which can affect the performance of components such as wide temperature requirements, vacuum, and radiation effects. The use of COTS components requires these effects to be considered in the design of space systems.

4.4.1 Radiation

The effects of radiation on objects in space have been well studied and CMOS technologies are known to have superior intrinsic radiation tolerance compared to CCDs. Radiation effects can be split into two categories, Single Event Effects (SEE) and cumulative effects.

Cumulative effects are caused by a buildup of charge in the gates or oxide layers of the substrate. It is contributed to by both ionizing radiation, Total Ionizing Dose (TID), and non-ionizing radiation, Non-Ionizing Energy Loss (NIEL). However, NIEL is not a factor for CMOS technologies. This causes a variety of effects including changing of the electrical characteristics, generation of leakage currents, and generation of electric fields in the doped silicon. However, as CMOS technology has advanced, these effects have been limited by decreasing feature size. This has mostly eliminated TID effects in the gate layers and limited damage in other oxide layers to being observed with MRad doses [72]. These dose levels are much higher than a typical nanosatellite which can expect <0.5krad over a one year mission for a camera system at 700km and 90° inclination [73].

SEEs are caused by single high energy impacts on a silicon substrate that cause a change in the state of a transistor/logic gate. They can cause latchups and burnout with sufficient energy. SEEs have also decreased with the advancement of CMOS technologies but are not seen as a large issue given the short lifespan of a nanosatellite.

4.4.2 Thermal

To determine the performance of the camera in the space environment it must be tested under the conditions that it is likely to see in space. Therefore thermal cycling tests are performed over a temperature range of -40°C to +70°C, the range commonly seen by small satellites with no thermal control that are in Low Earth Orbit.

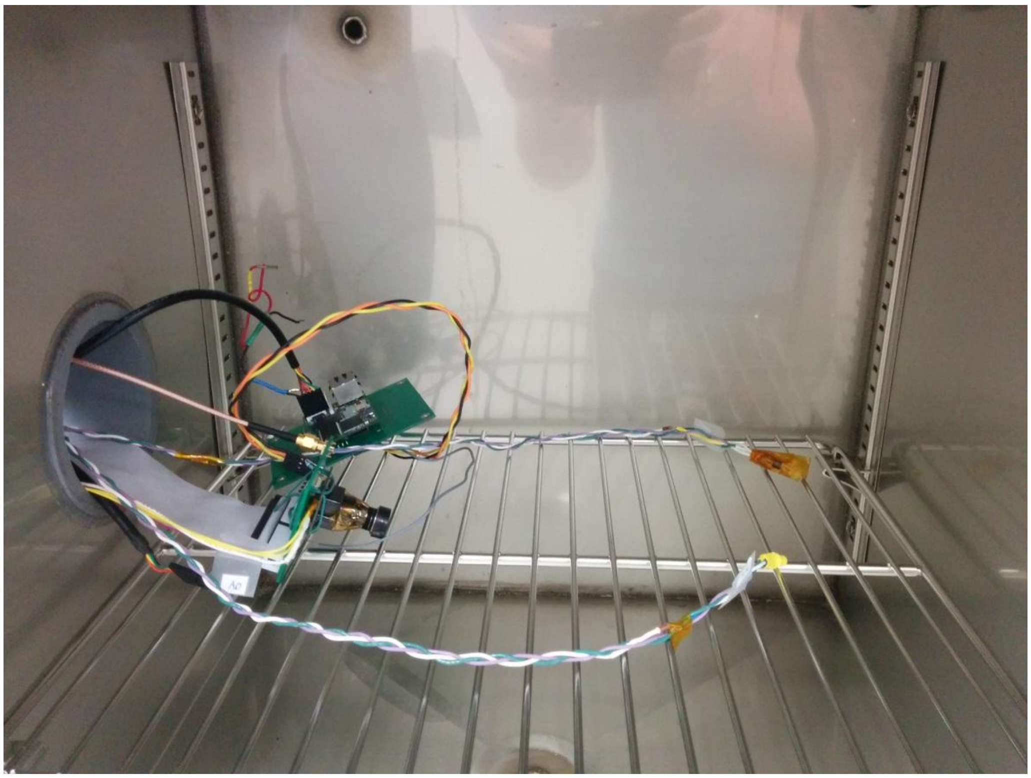

Figure 38 - Thermal test setup

The test is performed in a thermal chamber, as in Figure 38, programmed to the following temperature profile:

1. Ramp to 25°C, soak 30 minutes
2. Ramp to -15°C, soak 1 hour
3. Ramp to -30°C, soak 1 hour
4. Ramp to -40°C, soak 1 hour

5. Ramp to 25°C, soak, 1 hour
6. Ramp to 60°C, soak 1 hour
7. Ramp to 70°C, soak 1 hour
8. Ramp to 25°C, soak 1 hour

Each temperature change is followed by a 1 hour soak so that the temperature in the chamber and of the camera has stabilized. Afterwards the camera is turned on and 5 photos are taken with the lens cap on and averaged to determine the average scene level. The standard deviation of each average scene is then taken and compared between the temperatures to see how the sensor is affected by the change in temperature. The test was performed with automatic settings disabled, a digital gain of 0xf4, analog gain 0x40, and exposure time of 480 rows.

Table 7 - Standard deviation change with temperature

Temperature(°C)	25	-15	-30	-40	25	60	70	25
Mean Frame Value(LSB)	50.9	46.4	36.2	45.8	45.8	45.3	44.8	45.1
Standard Deviation(LSB)	19.8	16.8	16.0	15.8	18.0	46.5	62.8	18.0

Table 7 shows that the mean value of the frame does not change a lot with the change in temperature. However, the effect of kTc noise on the sensor is clear from the standard deviation, which changes directly with the temperature.

4.5 Summary of Camera Interface Design

The design of the camera system includes three main parts, the camera, the FPGA, and the microcontroller. The microcontroller has the role of being the OBC of the satellite and is there to receive an image for processing. The FPGA is responsible for processing the raw data stream from the camera and outputting it in a usable format for the microcontroller. The FPGA design uses 5 main blocks to take the high speed incoming data, extract a single image, and output to a microcontroller using a slower form of communication. Each block is responsible for specific tasks and ensure that one image at a time is stored and output on command from the user.

Environmental considerations are taken into account to ensure the operation of the camera in the space environment. Radiation is not a concern for short duration missions that nanosatellites are typically operating for due to advances in the design of the sensor itself. Thermal testing showed that the selected image sensor remains operational over the range of temperatures expected on orbit.

Chapter 5 In Lab Calibration

To determine the characteristics of the camera 4 tests are performed: Flat-Field Illumination, Shutter Closed, Point Source, and Checkerboard Pattern

5.1 Flat-Field Illumination

The Flat-Field Illumination test is used to help determine the FPN of the sensor. This is done by repeatedly taking pictures of a white screen with a Lambertian reflectance and averaging the value of each pixel across all the pictures. By averaging across a large number of images the temporal noise sources that cannot be completely eliminated through the technology used to construct the sensor is averaged out of the dataset. The chosen camera features a global shutter, this limits the characterization of the FPN to the pixel level, as no column readout circuitry is used. As this test uses an illuminated surface it is characterizing the PRNU of the sensor.

A Lambertian surface appears to have the same brightness when viewed from any angle due to Lamberts Cosine Law [74]. This ensures that wherever the sensor is it sees the same scene and should produce a uniform readout of all pixels.

To calculate the FPN correction the average value of each pixel across all the images is taken.

$$\overline{P_{i,j}} = \frac{\sum_{k=1}^{N} P_{i,j}^{k} P_{i,j}}{N}$$

Where N is the number of images taken and $\overline{P_{ij}}$ is the average value for each pixel across all the images taken, i and j are the row and column number respectively. The average pixel value across all images is then calculated and is used as the true measurement of the scene illumination level.

$$\bar{P} = \frac{\sum_{k=1}^{N}\sum_{i=1}^{C}\sum_{j=1}^{R} P_{i,j}}{N * C * R}$$

Where C is the number of columns in the image, R is the number of rows and $\bar{P}$ is the average pixel value across all frames. The FPN correction can then be calculated as follows.

$$FPN_{i,j} = \overline{P_{i,j}} - \bar{P}$$

This test was performed twice, once with the Automatic Settings turned on and once with the settings turned disabled and the test configuration is in Figure 39.

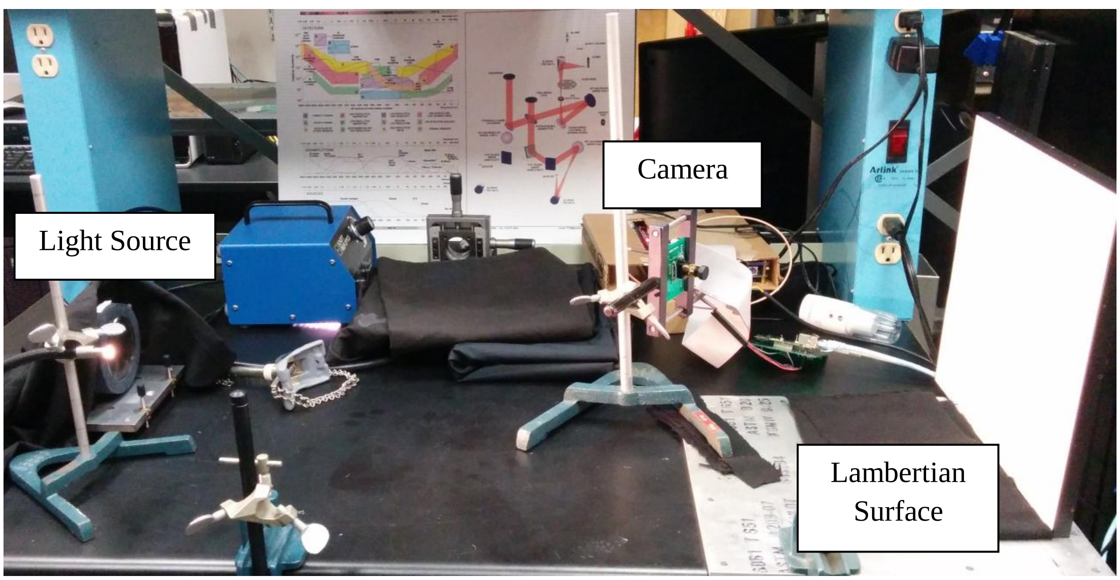

Figure 39 - Flat field illumination test configuration

5.1.1 Automatic Settings Enabled

The test is performed with the Automatic Gain Control and Automatic Exposure control turned on. In addition the Digital Tiled Gain setting, which affects overall scene brightness, was set to 0xf7. Twenty images were taken under identical illumination conditions with the entire screen illuminated. The test images show that with the automatic settings on the illumination does not appear to be uniform over the frame and is dimmer towards the corner of the image as in Figure 40.

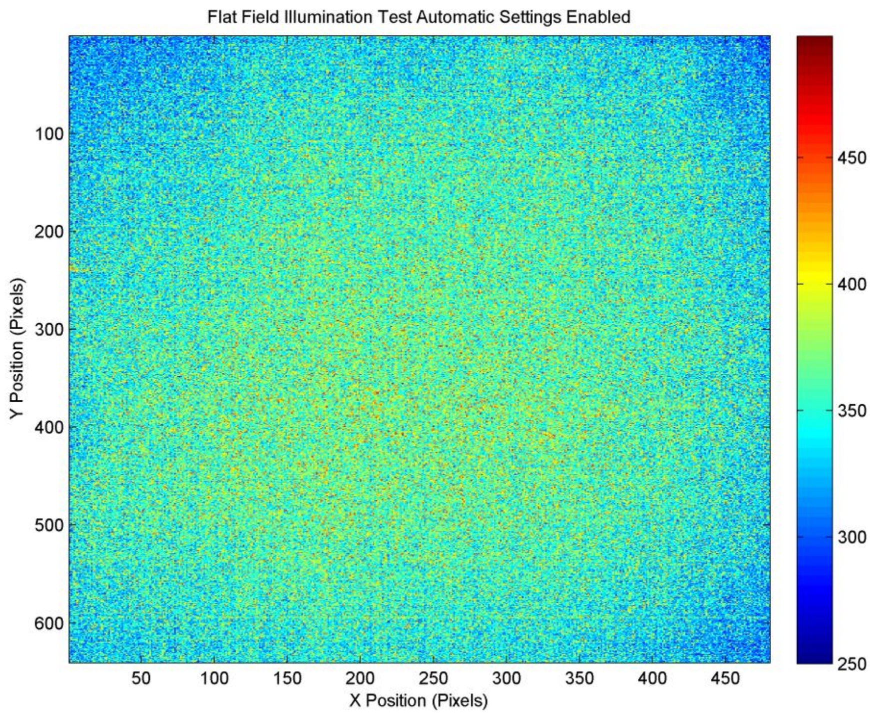

Figure 40 - Flat field illumination test automatic settings enabled

The standard deviation across the entire image array for all the images was found to be 23.968; however, the maximum standard deviation across all images on a pixel by pixel basis was only 1.468 with a mean of 0.496. Standard deviation was also found to be higher towards the centre of the image as seen in Figure 41.

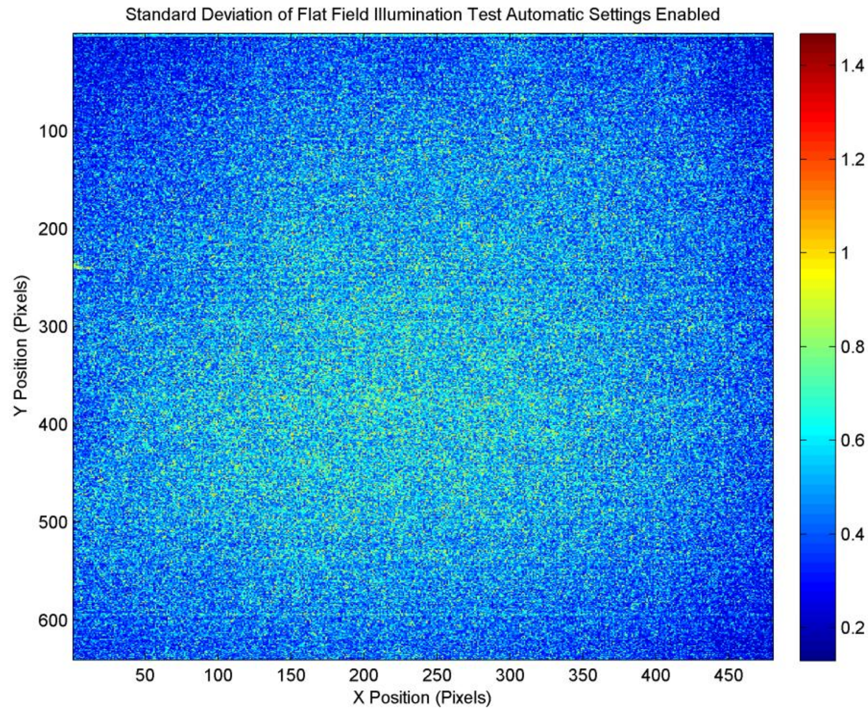

Figure 41 - Standard deviation of flat field illumination test automatic settings enabled

The FPN correction is then calculated with the largest corrections occurring towards the corners and at the centre as seen in Figure 42. The wide range of the correction values demonstrates the difficulty in producing a consistently dark image with the automatic settings enabled.

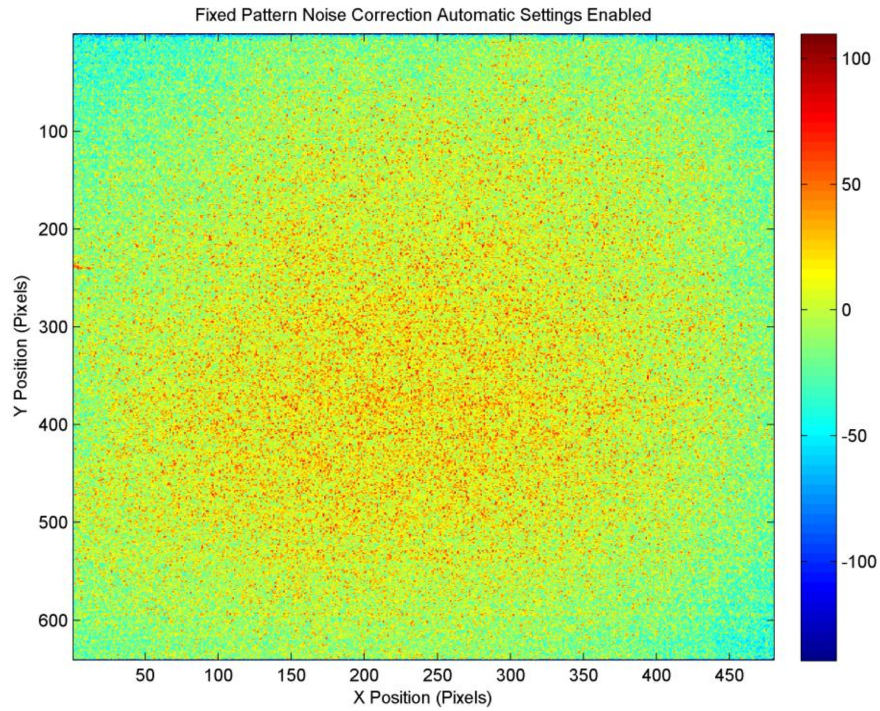

Figure 42 - FPN correction automatic settings enabled

5.1.2 Automatic Settings Disabled

The test is then repeated with identical lighting conditions with the Digital Tiled Gain setting was lowered to 0xf2, this is due to the pixels getting saturated at higher gain settings. Ten pictures were taken of this setup and each picture produced an entirely uniform field, with each pixel having an identical value. The difference frame to frame of the level of brightness was very stable and had a standard deviation of 0.8933. Therefore with the automatic settings disabled no FPN correction should need to be applied to images, a much superior option to the corrections required

Table 8 - Flat Field Illumination levels with automatic settings disabled

Frame	1	2	3	4	5	6	7	8	9	10
Level	497	495	495	494	494	495	495	495	494	496

5.2 Shutter Closed

The Shutter Closed test is performed by taking a picture with the shutter closed to prevent any light from being collected. This is done to determine the dark noise as well as the FPN (DSNU) which manifests as pixels that register values well above the rest of the pixels and are termed hot pixels. In the case of star imaging these hot pixels must be identified as the rest of the image will typically have a very low signal level so it is easy for these hot pixels to be misidentified as stars. The noise that is dominant in this test varies with exposure time, therefore the test is be repeated with various exposure times with 20 images taken at each exposure level. For this test a hot pixel is considered to be any pixel which deviates from the average scene value by more than 5σ in the majority of the test images.

Exposure time for this camera is calculated using the following equation:

$$t_{int} = N_{rows} * t_{row} + t_{overhead}$$

Where N_{rows} is the number of rows being integrated across and is the value set to change the exposure time. t_{row} is the time taken to integrate each row and $t_{overhead}$ is the extra time required for the camera to process each image. Given a clock speed of 13.5MHz and an output of 640 columns with 43 blanking columns the exposure time is calculated for three different numbers of rows which correspond to different exposure times:

Table 9 - Shutter Closed Test Results

Exposure Time (rows)	480	960	1440
Exposure Time (s)	0.0243	0.0486	0.0729
Number of Hot Pixels	6	96	476
Average scene value Enabled (max. 1023)	61	61	61
Average Scene Value Disabled (max. 1023)	41	41	41

This test was performed at room temperature with the AEC and AGC disabled and then with them enabled. The analog gain was set to its maximum value (0x40) and the digital gain was set to a value of 0xf7 which is a medium gain level. As exposure times were increase it was found that the number of hot pixels increased at a non-linear rate as in Figure 43. Exposure times greater than 1440 rows were not used as the number of hot pixels present became significant with longer exposure times. For the exposure times tested the number of hot pixels was the same for both enabled and disabled settings. The percentage of pixels which appeared hot for each exposure time were: 0.00195%, 0.03125%, and 0.1617% respectively.

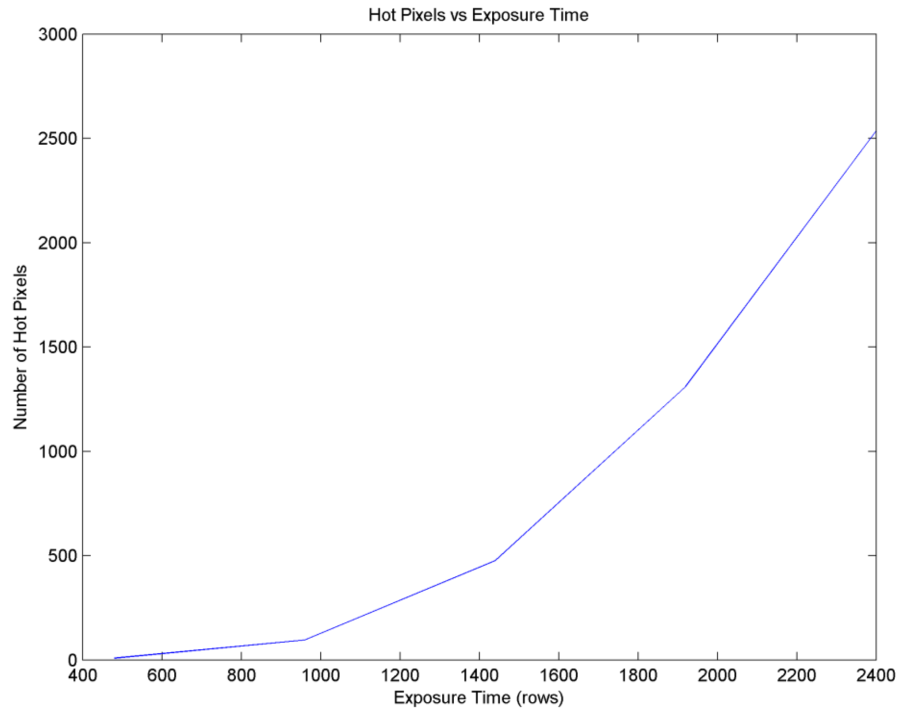

Figure 43 - Number of hot pixels versus exposure time

The distribution of the hot pixels is random and consistent between images, however, as exposure time is increased the number of pixels which sometimes record hot values increases. For an exposure time of 1440 rows 83% of pixels are hot in every frame while for 960 rows 90% of pixels are hot in every frame sampled. For 480 rows the same 6 pixels are hot in every frame taken. This is explained by the increase in likelihood of random noise causing a hot pixel as exposure time is increased.

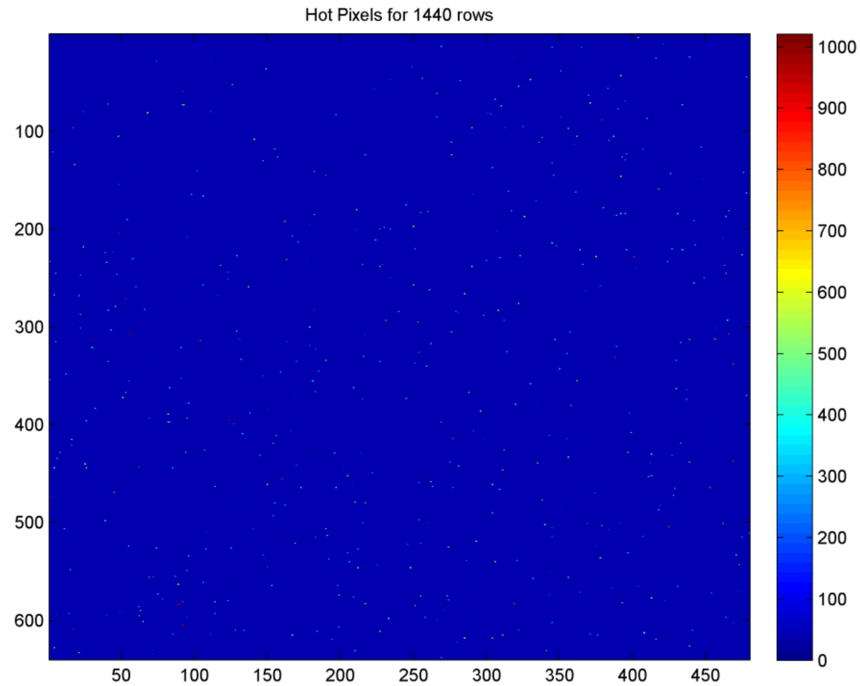

Figure 44 - Hot pixels for exposure time of 1440 rows

The row-wise noise correction algorithm was left on for this test as it is not possible to disable it. This feature uses the optically dark frames to calculate the expected noise level and subtracts it from the row as it is output from the pixel, it then adds an offset. The default offset is 42 which is what produces the average of 41 for the tests that the remaining automatic settings are disabled for. When the automatic settings are enabled it is clear that the AGC is causing an increase in the overall signal level of the image.

5.3 Point Source Illumination

Imaging of a point source is examined to characterize the sensors Point Spread Function (PSF). The PSF is a measurement of the sensors response to an impulse input, ideally it would be perfectly circular and the exact size of the point source however, this is not the case as the distortions introduced by the lens and sensor distort it. This is tested using a light source, collimating lens, and a pinhole mask. The collimating lens is used to collimate the light into parallel light rays which limits the spread of the light out in a conical shape. The pinhole mask is used to block the light except for a very small area which simulates an impulse input for the sensor. We then assume that the sensor is continuously sampled meaning that the sensors physical pixel size is irrelevant. The response of the imager, or the image produced, is then the Point Spread Function (PSF) of the camera.

This test was performed with the automatic settings disabled, the analog gain set to 0x40, and the digital gain set to 0xf4. An exposure time of 480 rows was used for these images. The pinhole mask had 5 pinholes in it which produced multiple impulse inputs as seen in Figure 45 and as a Matlab plot in Figure 46. This image was taken with a bright light source to test the system setup, the pinholes which are farthest from the centre of the camera boresight appear dimmer due to their misalignment with the lens.

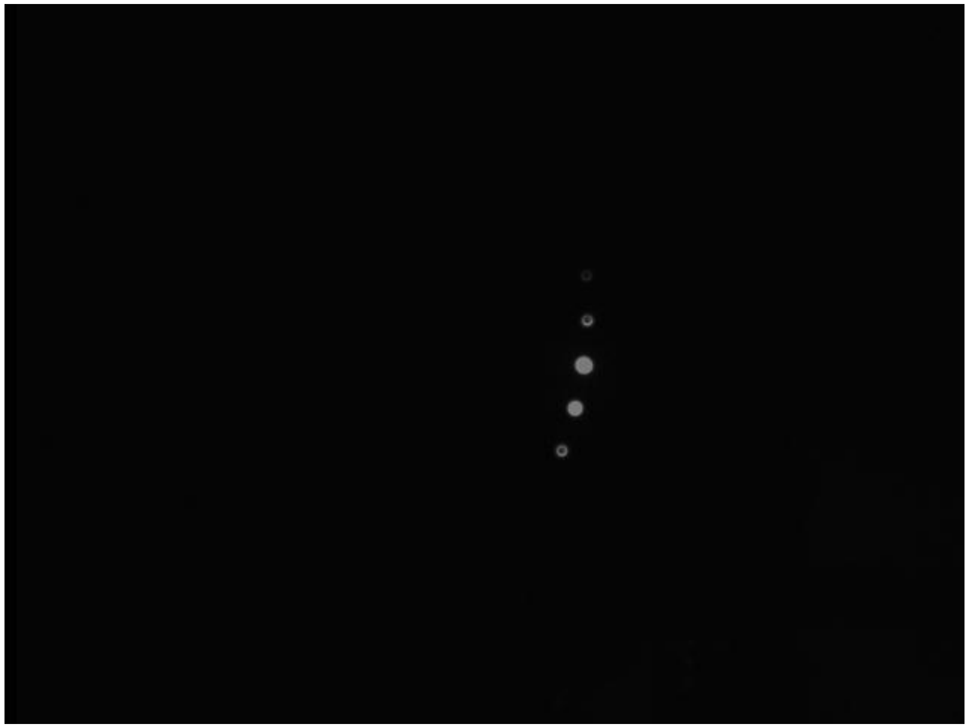

Figure 45 - Test picture with pinhole mask

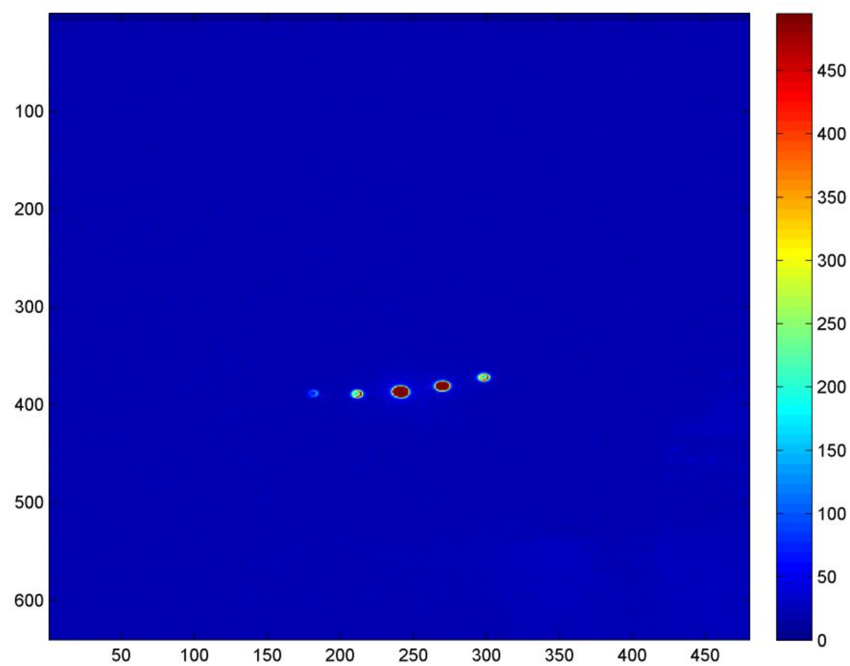

Figure 46 - Test picture with pinhole mask Matlab plot

With a reduced brightness from the light source a number of images were taken to characterize the point spread function, the images were analyzed in Matlab and a plot was produced to visualize the PSF in Figure 47. The produced PSF does not resemble an impulse input with Airy disk pattern around the peak of the signal; it instead has a peak close to the rim of the Airy disk. When the brightness was increased the disk was filled in and produced a circular peak as in Figure 48.

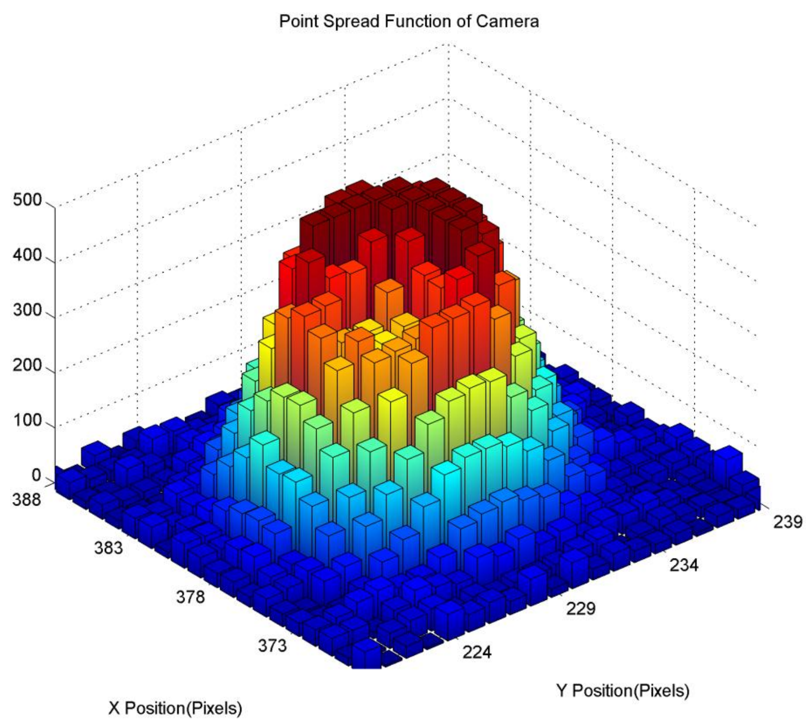

Figure 47 - PSF for dim light source with mask.

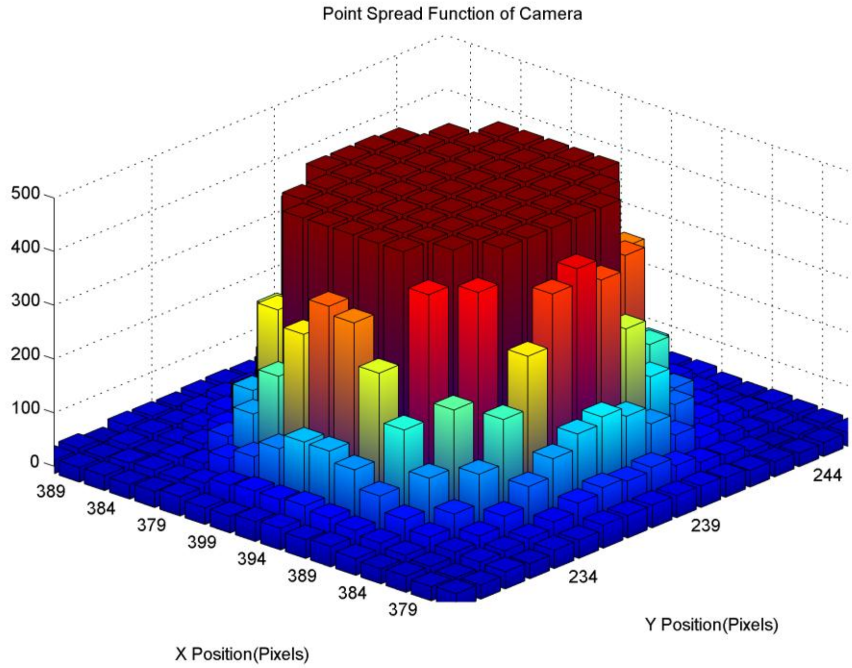

Figure 48 - PSF for bright light source with mask.

The test was then repeated with an identical setup however without the pinhole mask resulting in the entire lens being illuminated. The brightness of the light source was then varied the same way as with the mask and the results are in Figure 49 and Figure 50. Figure 49 possesses a similar shape as Figure 47 with the peak not coming in the centre of the illuminated area but towards the rim of the Airy disk. Figure 50 has the same shape as Figure 48 with the exception that the illuminated area is much larger and the pixels are saturated.

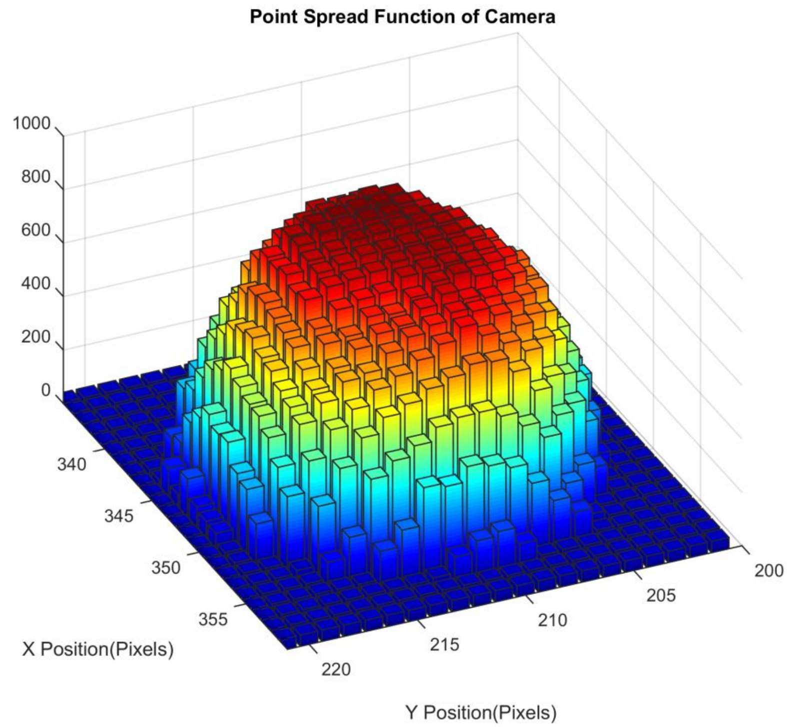

Figure 49 - PSF for dim light source with no mask.

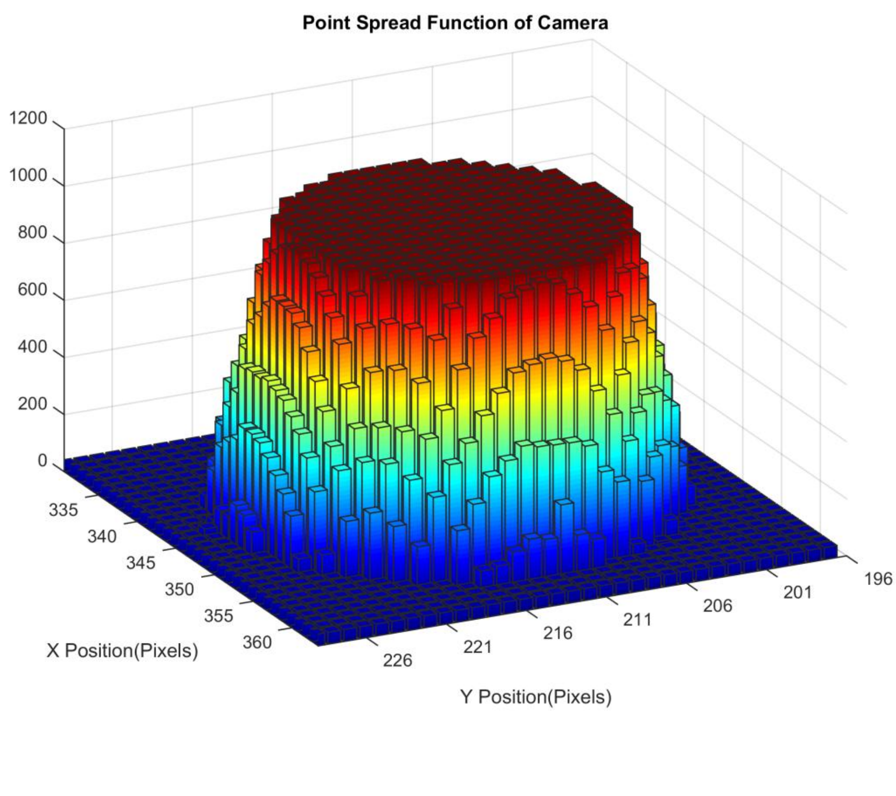

Figure 50 - PSF for bright light source with no mask.

5.4 Checkerboard Pattern

It is possible to remove aberrations from the system by imaging a known spatial pattern and comparing the image obtained, which will be distorted, to the original spatial pattern. This is done using a publicly available toolbox for Matlab known as the Camera Calibration Toolbox [75], which was developed at the California Institute of Technology.

To use the toolbox a series of images, 22, are taken of a checkerboard pattern from different angles and distances. A checkerboard pattern is used because the spatial pattern is easily discernible and has straight edges making it easy to identify distortions. An image used in calibration can be seen in Figure 51. The corners of the pattern are selected manually and the program automatically detects the number of squares in each direction. The calibration is done in two steps: first an initialization using a closed-form solution to the camera parameters, the second a least-squares optimization to minimize error in the reprojection of the corners using the calibration parameters. The calibration parameters include 9 intrinsic parameters and 120 extrinsic parameters.

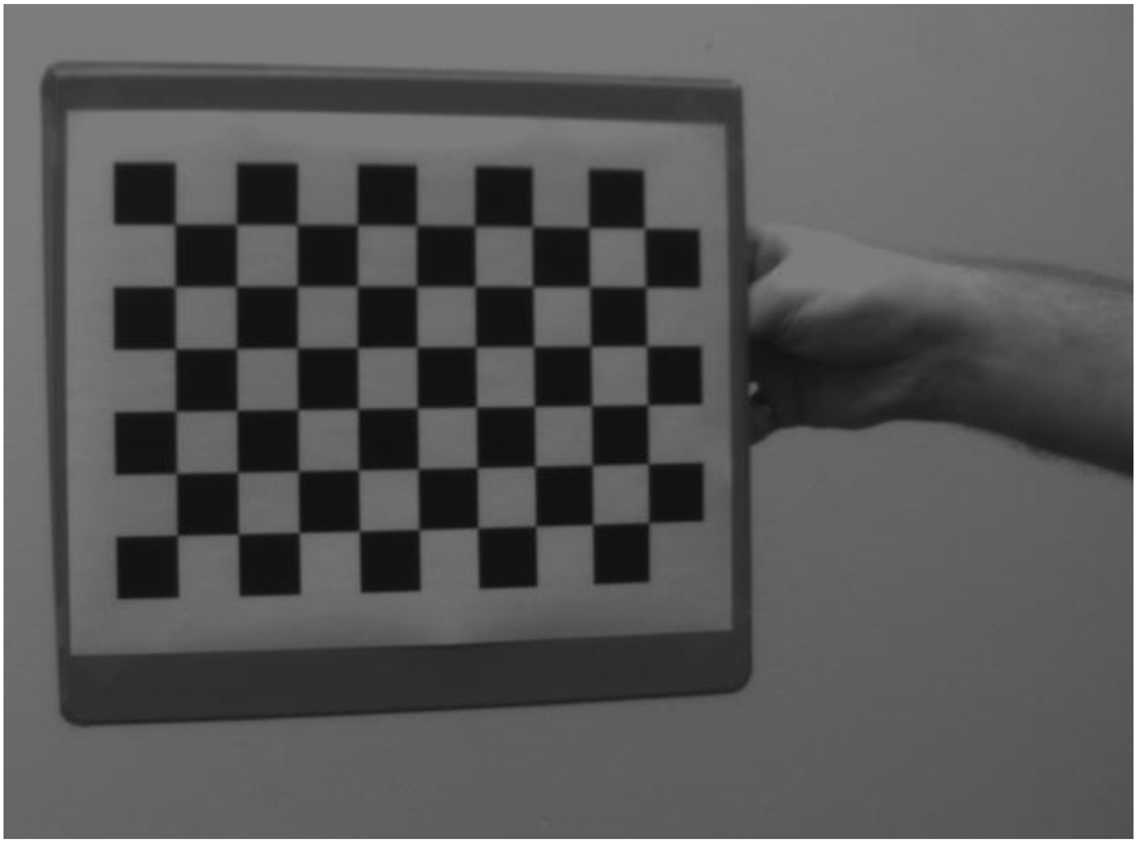

Figure 51 - Image of checkerboard used in calibration

5.4.1 Calibration Results

The calibration produces the focal length of the camera, the principal point of the camera, the pixel error as well as the radial and tangential distortion coefficients. The procedure also produces a plot of the spatial relationship of the checkerboard pattern in each frame to each other in Figure 52. It is important that the checkerboard patterns are spread out in different orientations and angles to ensure that the camera is properly characterized; in this case many orientations and positions are visible.

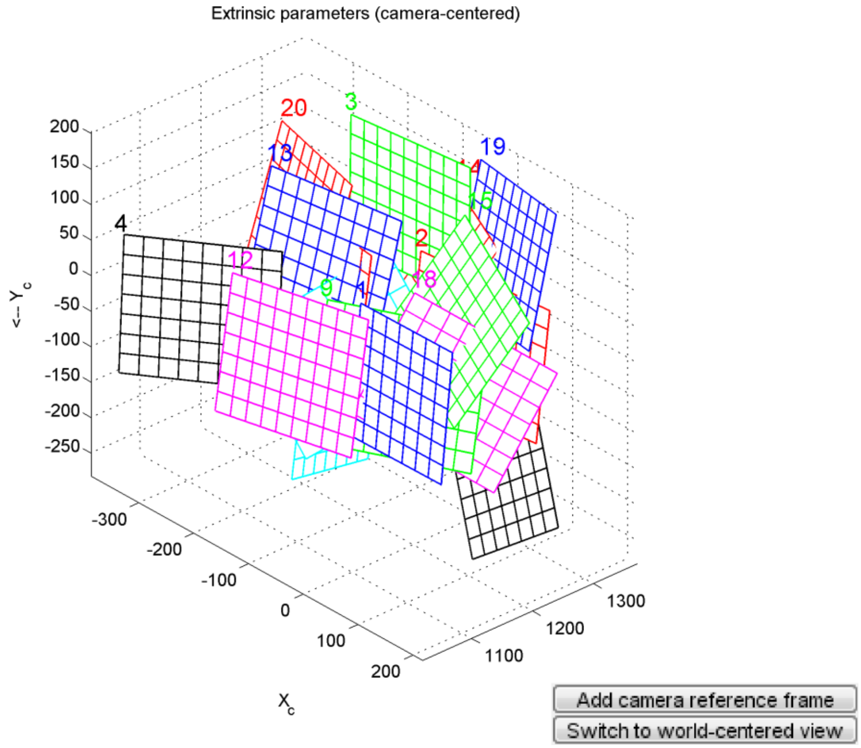

Figure 52 - Spatial position of each checkerboard pattern

The complete results are in Figure 53. The focal length is given in pixels in the x and y dimension and can be multiplied by the pixel size to get the calculated focal length. With a pixel size of 6µmx6µm the calculated focal length is 7.410mm±0.158mm in the x direction and 7.400mm±0.145mm in the y direction. These values are very similar due to the pixels being square and are close to the focal length of the actual lens which is given as 7.2mm. The difference between the actual and calculated focal length suggest that the lens was slightly defocused during the test.

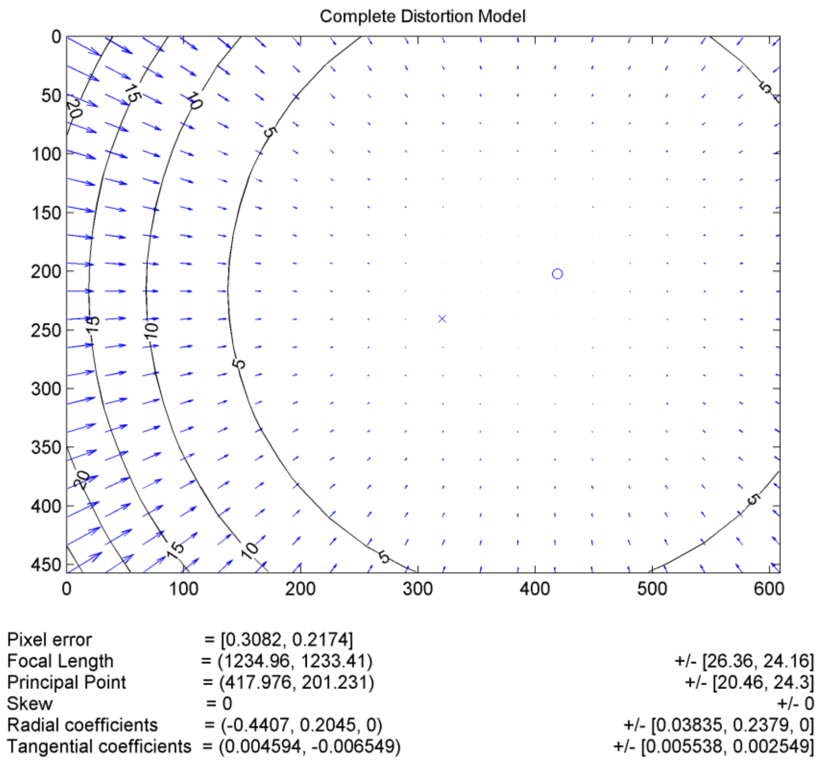

Figure 53 - Complete distortion model

The principal point is given in pixels and represents the origin of the distortions; it is marked as a circle in Figure 53. In this case it is not aligned with the centre of the image which is marked with an x. This is due to the area of the image sensor that is read out and the position of the optically sensitive area of the sensor relative to the centre of the lens boresight. These misalignments produce an uneven distortion pattern across the sensor which has a maximum in the corners of the left hand side of the image.

The Radial and Tangential distortion coefficients are also given and the tangential component is considerably smaller than the radial component shown in Figure 54 and Figure 55. The tangential component has an elliptical shape unlike the circular shape of the radial distortion. Tangential distortions are produced by the imperfect alignment of the lens components as well as manufacturing defects. The effects of this distortion are minimal compared to the radial components.

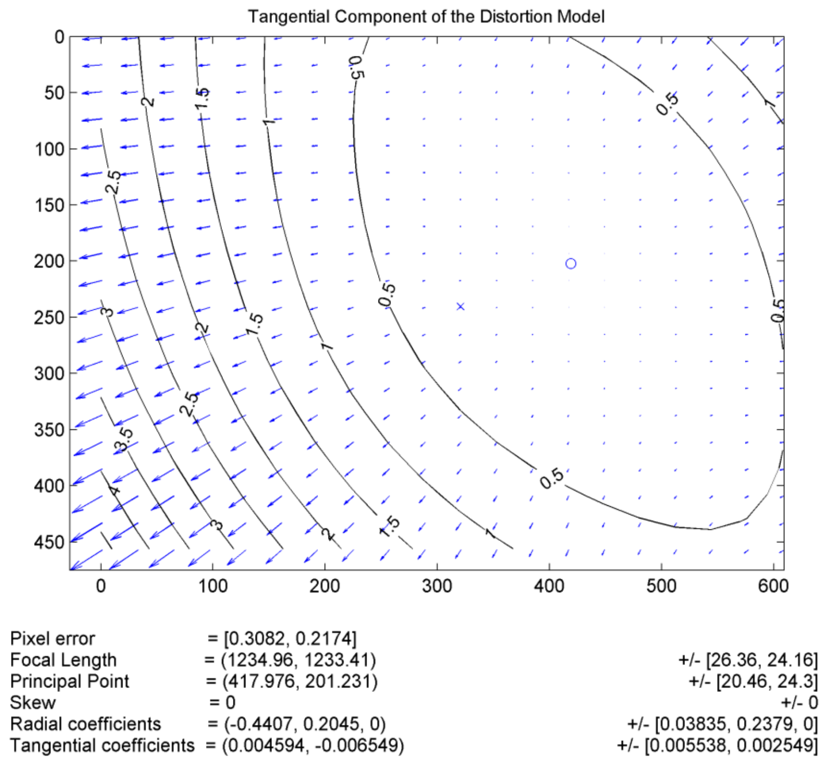

Figure 54 - Tangential component of distortion model

Radial distortion is caused by the aberrations produced by the lens itself including distortion, astigmatism, field curvature, and lens coma. The selected lens is known to have a high barrel distortion which contributes to the greater radial distortion.

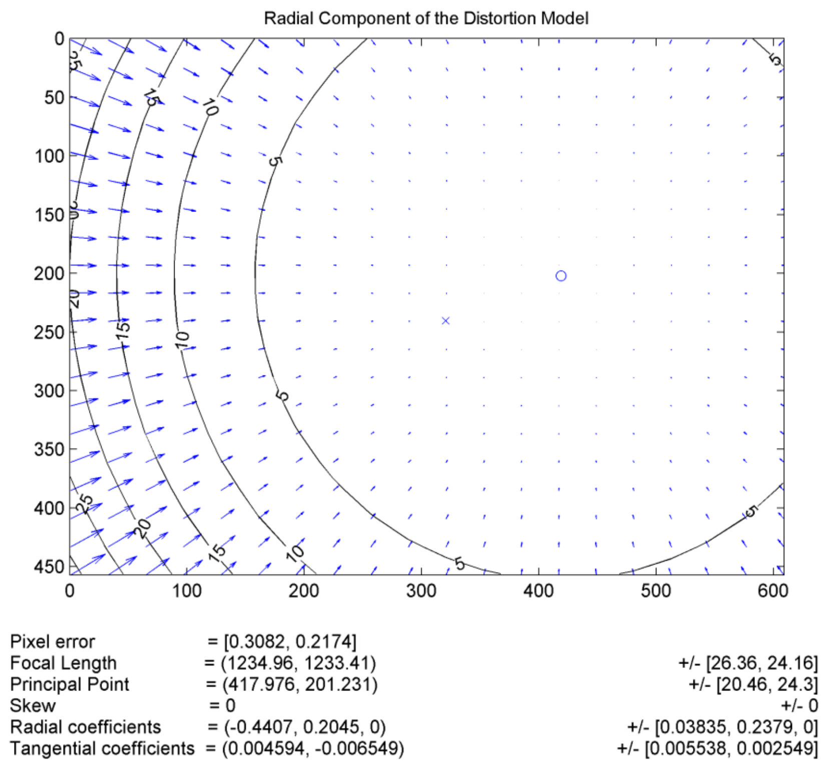

Figure 55 - Radial component of distortion model

The pixel error is the estimated error in position of an object in the image and is given in pixels. The calculated error has a standard deviation of 0.3082 pixels in x and 0.2174 pixels in y which is the reprojection error over all the images used in the calibration. The errors in individual images varied from -1.5 to 1.1 in x and -1.2 to 0.65 in y and are in Figure 56. This pixel error corresponds to an error of 54.54” in x and 38.48” in y.

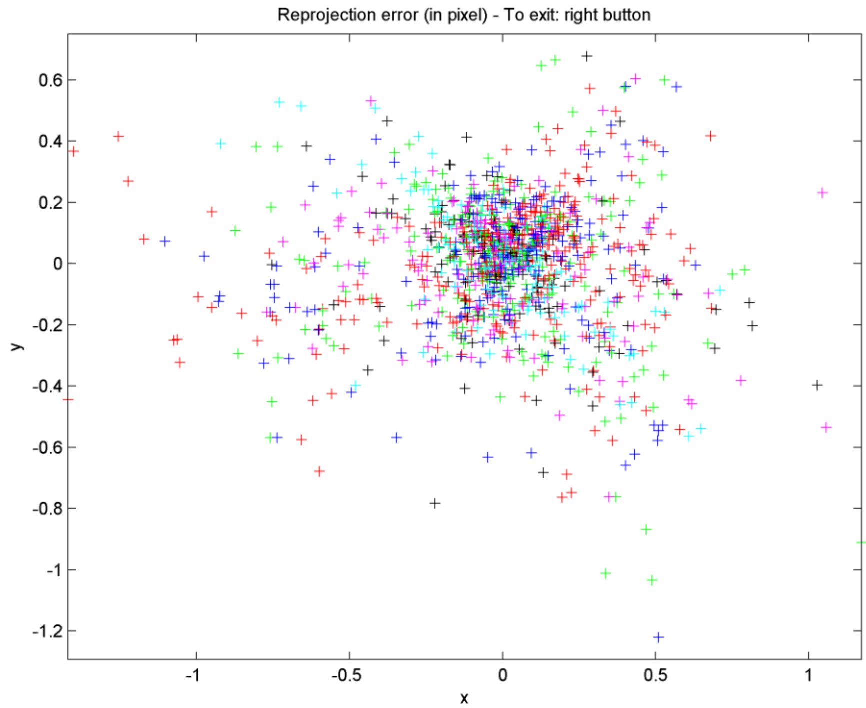

Figure 56 - Reprojection error

5.5 Summary of Camera Calibration

Using 4 different tests the cameras characteristics have been experimentally determined. The Flat-Field Illumination test showed that the PRNU is uniform with the automatic settings disabled producing an entirely flat image level. With automatic settings enabled there is a considerable amount of noise in the image, showing the gain in image quality from turning off the automatic settings. The test with the shutter closed provided a control image with automatic settings disabled that showed the DSNU that was present in the imager. Different exposure times were used to identify the number of hot pixels as well as their prevalence. The same pixels consistently recorded higher than average values for each image which makes it easy to identify and eliminate the pixels values from eligibility as stars. This test also revealed that the sensors Automatic Black Level Correction could not be shut off but could be adjusted by changing the offset. The Point Source Illumination test provided a PSF for the camera system that showed that under low illumination levels the signal would not appear as an impulse input but rather as a ring with a preference to one side. The Checkerboard Pattern test allowed for the characterization of the aberrations in the system as well as estimating the pixel error of the system. It also provides a method for removing distortions from images which will be used with test images allowing for the accurate determination of star positions.

Chapter 6 Night Sky Images

To determine the capabilities of the camera in situ is not possible as there is no direct analogue for the space environment that has no atmospheric or light pollution effects available. Therefore night time tests are performed in a low light pollution area to as closely approximate the on-orbit lighting conditions as possible.

6.1 Location

Using a map service which shows light pollution overtop of Google maps like Dark Sky Finder [76] allows for the selection of a site which will allow for the viewing of stars of magnitude 5. The location selected is marked with a star in Figure 57.

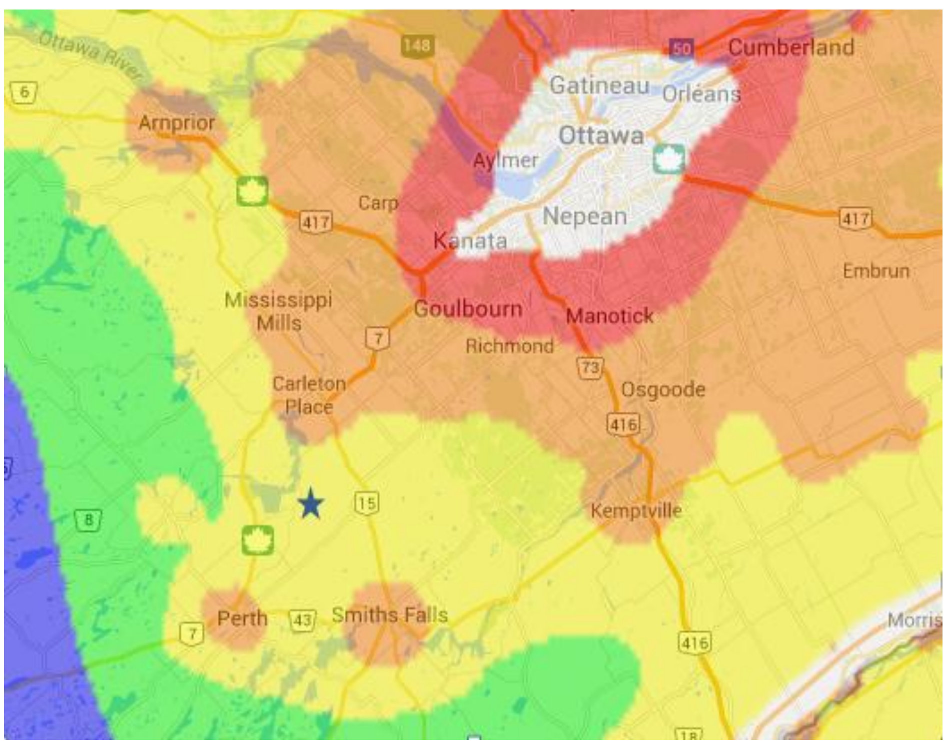

Figure 57 - Light pollution map of selected test location. Image Credit: [76]

The location was chosen for having low light pollution allowing stars of magnitude 6 and brighter to be seen with the naked eye. The location also has access to power and internet allowing for troubleshooting and longer testing times overnight. Its coordinates are 44.9968°N 76.0895°W at 65m.

6.2 Images

Images were taken with automatic settings disabled, analog gain of 0x40, and digital gain of 0xf4. These settings were used for all images, and are the same settings used in the tests from Chapter 5, to maintain consistency and to give the greatest likelihood of detecting a star. Areas of the sky were selected to be imaged based on the presence of multiple stars or for having a single bright star that could easily be seen to verify the functionality of the camera.

Night sky imaging was performed on two separate nights, with many images taken of different parts of the night sky. The images presented were chosen for the bright star that was visible in them.

The first image is of Vega which is a star of magnitude 0.0, images were taken with exposure times of 480 and 960 rows respectively and can be seen in Figure 58 and Figure 59. Neither image has had any kind of correction performed and Vega is visible in both images inside the circle.

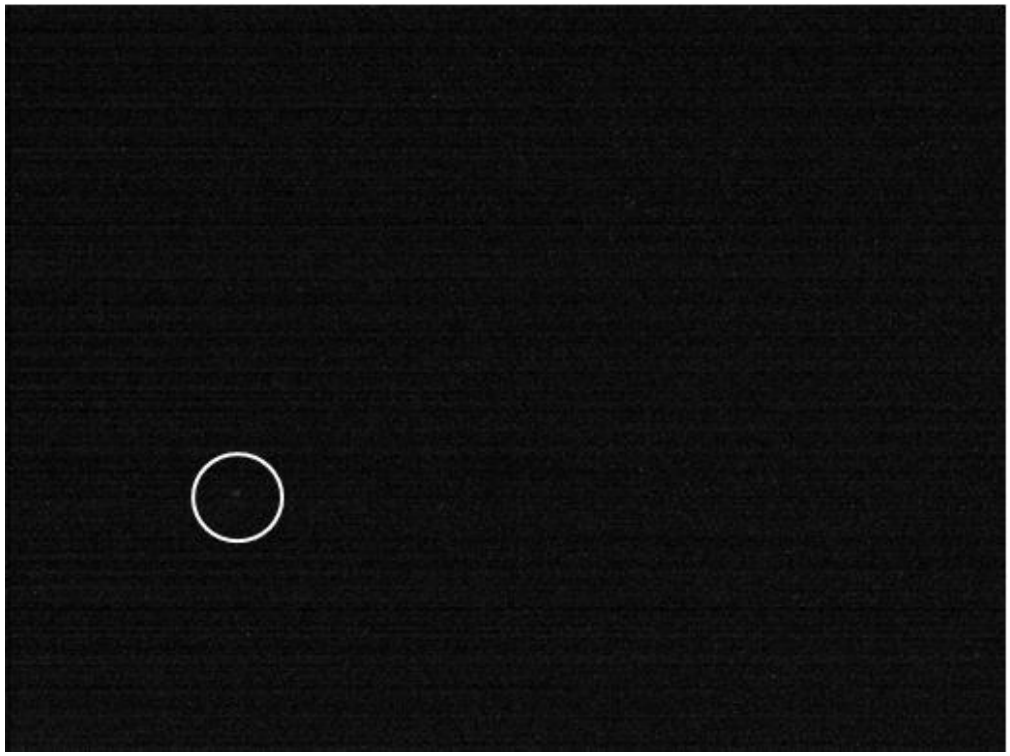

Figure 58 - Image of Vega exposure time 480 rows

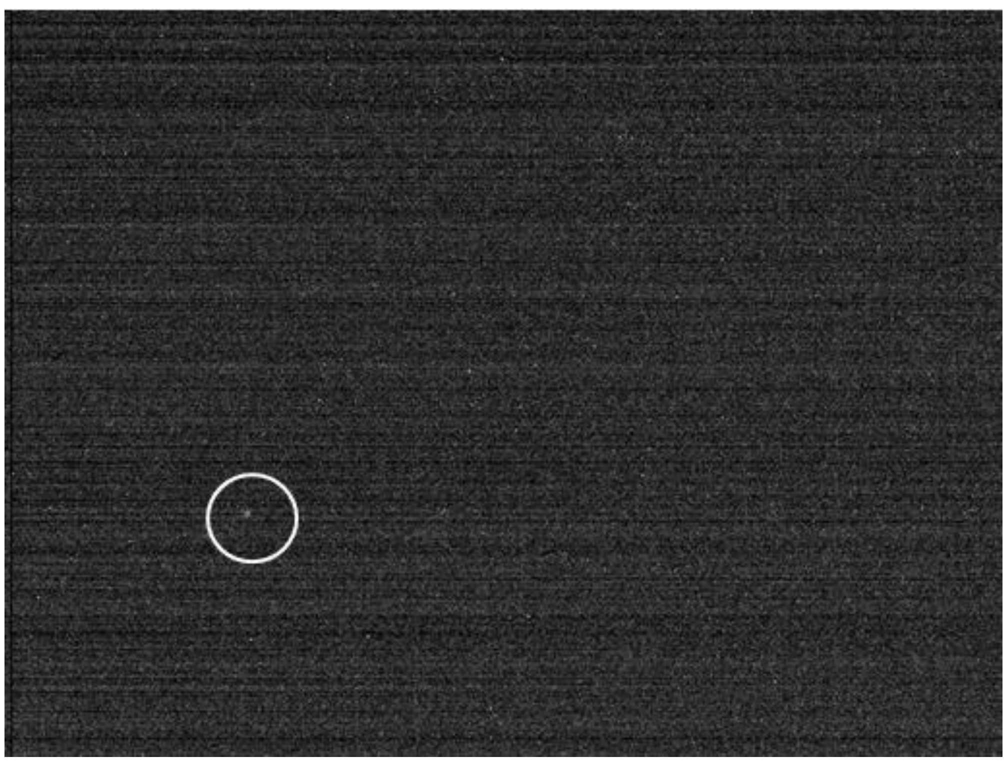

Figure 59 - Image of Vega exposure time 960 rows

6.3 Analysis

The calibration data collected in Chapter 5 is then used to reduce noise, remove distortions and analyze the images. This is done by first removing the hot pixels, and then using the camera calibration program to undistort the image. The resulting pattern is then compared to the expected PSF. Using Stellarium [77] it was possible to determine the brightness of the star that was imaged. Vega is a magnitude 0.0 star which at the time of imaging was low on the horizon; Stellarium provided an estimated extincted magnitude of 0.74.

6.3.1 Exposure Time 480 Rows

This image had a low noise level due to the short exposure time which produced few hot pixels and overall a dark scene. With the picture undistorted the hot pixels were removed and the standard deviation of the pixels value dropped from 29.265 to 29.118. However when using the noise patterns that were attained during tests with the shutter closed to reduce image noise an increase in the standard deviation and in total noise was observed. Therefore the correction was removed and not used.

After removing distortions the PSF of the star appears as a single peak with pixels around the peak roughly forming a ring of values above the background pixel value. The peak appears closer to the edge of the ring as it did in the tests in the lab and can be seen in Figure 60.

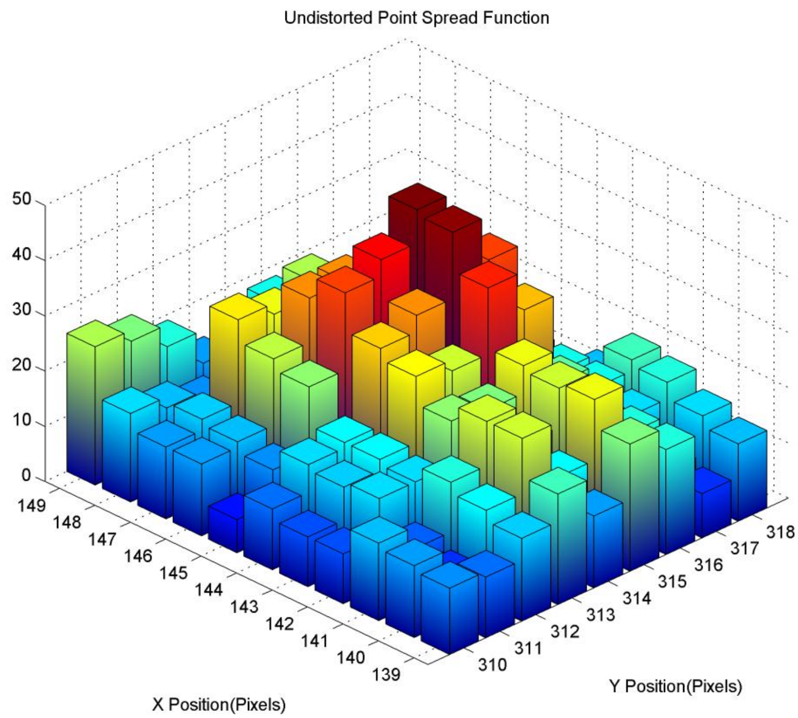

Figure 60 - PSF for undistorted image for exposure time 480 rows

6.3.2 Exposure Time 960 Rows

This image had more noise in the scene due to the increased exposure time, however attempts to remove the noise did not improve the image quality as the noise that is present is mostly random and was not the same as the noise that was observed when testing the camera with the shutter closed. The same hot pixels were removed and the image was undistorted. The increase in noise is likely due to stray light entering the lens. While the location selected was very dark there were still buildings nearby as well as the remainder of the testing equipment which all generate some light. The corrections from the shutter closed test were also applied but did not decrease noise levels in the image. This is likely due to the source of the noise being other than the dark noise that was accounted for in the test.

A feature that is more noticeable in the 960 row exposure than the 480 row exposure is the effect of the BLC algorithm. This algorithm is designed to remove noise from each row of the sensor individually producing a flat image, however, in practice it was found that this process results in lines being generated in the image lowering the quality of the image. This effect was also present in the 480 row exposure but is much less pronounced.

The PSF from the longer exposure shares the shape of the PSF from lab testing more closely than the short exposure from Figure 61. This suggests that as brightness of an object increases that the PSF will not extend outward from the peak but will instead form a ring before filling in to produce a full bright spot as in Figure 48.

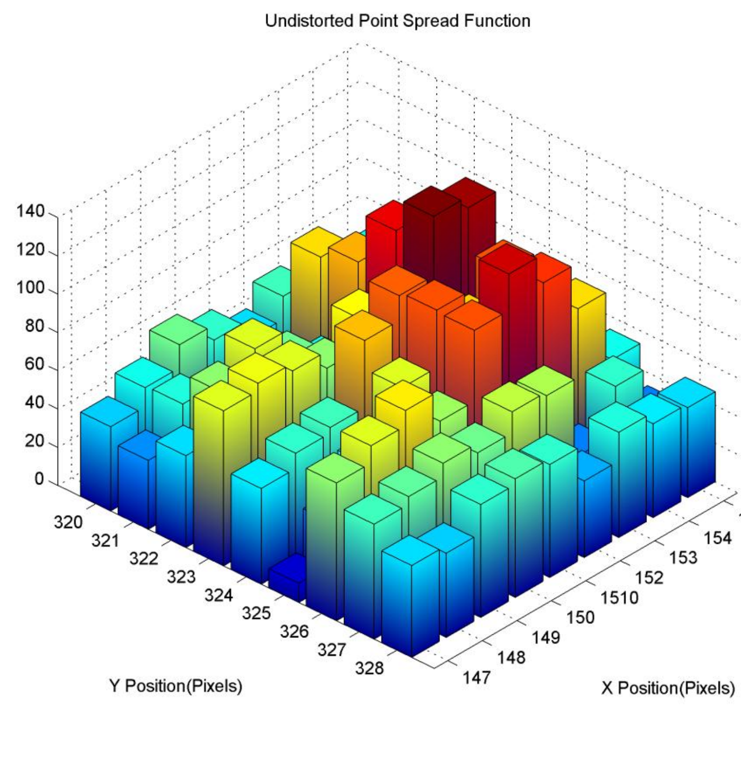

Figure 61 - PSF for undistorted image for exposure time 960 rows

6.4 PSF in Star Tracking

Knowing that the PSF of the imager is consistent between the lab tests and the field tests means that the position of a star on the sensor can be determined to sub-pixel accuracy using centroiding. By taking the peak pixel and finding the mean position of the values in an area around it the location of the star can be determined to less than one pixel. With the ring shaped PSF that has been observed it is important to include the entire shape in the centroiding algorithm to ensure that the location of the star is accurately determined. Since the peak does not occur in the exact centre of the ring the centroiding algorithm must use an area that is not centered on the peak or part of the stars signal could be missed. Therefore any centroiding algorithm would need to expand non-uniformly from the peak of the signal with a greater expansion in the –X and –Y directions.

6.5 Summary of Night Sky Images

Testing of the camera at night allowed for the comparison of real images to the test images that were taken under controlled conditions in the lab. The corrections that were generated in the lab for dark noise in low light settings were not able to be successfully applied. The night sky tests showed that while testing in a terrestrial environment there is a limited ability to limit the noise the sensor observes leaving only the brightest stars visible. The PSF gained from the night sky tests have a similar shape to the PSFs gained in the lab testing. The PSF for the camera appears to consistently be a ring shape with a peak towards one side. The consistency between lab and night sky images means that it is possible to use the signal from the star for a centroiding algorithm that is designed to expect the PSF that has been observed.

Chapter 7 Conclusions and Future Work

7.1 Conclusions

The Primary objective of the thesis was to develop a camera system using COTS components and then characterize it. The Videology 24B752XA imager was selected based on meeting the restrictions of nanosatellites, specifically aiming to meet the restrictions of a 1U CubeSat. It has low power requirements and low mass and volume allowing it to fit into nanosatellite budgets. It is also designed with a wider operational range than normal sensors allowing it to function over the expected temperature range on orbit.

The Edmund Optics 7.2mm lens was selected for having a wide FOV and a low mass. It is also made of aluminum and will therefore not outgas in a vacuum preserving the optical components.

The camera system is set up with an FPGA to receive the data stream from the camera before outputting it to a microcontroller which serves as a stand-in for an OBC or similar nanosatellite hardware. The camera outputs image data via an LVDS protocol at a bit rate of 190Mbps to a custom designed breakout board which converts the signal to TTL levels that the FPGA can use.

The FPGA acts as a data processor that takes the high speed serial data stream, extracts an image and then outputs the image data via a standard UART signal. The

FPGA has five main blocks responsible for different parts of the data processing. The first block, LD, deserializes the data to take advantage of the parallel computing power of the FPGA. The second block, FDC, extracts the image data using the blanking rows to determine where each picture begins and ends as well as counting the number of pixels that have been read in each image. The third block, DB, acts as a buffer between the parallel output of the FDC and the high speed operation of the SDSR which operates at a faster speed to ensure that the data output from the image does not get backed up and result in lost data. The fourth block, SDSR, uses the onboard SRAM module to store a single image at a time before sending it back out. The fifth block, ImO, takes the image data from the SDSR and outputs it at a slower rate for the microcontroller.

The image sensor, lens, breakout board, and FPGA together constitute the camera system developed using COTS components to fulfill the primary objective of the work.

The camera system underwent four tests to characterize it. Tests were performed with a flat scene to determine FPN, with the lens cap on to determine dark noise at various exposure times. It was shown that under illumination the sensor produces a uniform response however when not illuminated some pixels have a much higher signal response. Tests were also performed with a point source to approximate the response to an impulse input like a star. Lastly the camera was calibrated using a checkerboard spatial pattern to determine the distortions introduced by the lens and sensor. The camera was also tested in a thermal chamber to ensure its operation over the temperature range expected on orbit.

The three primary research objectives have been accomplished at varying levels through the testing and calibration presented in this thesis. Determining the minimum detectable brightness for the imager was not performed in a controlled laboratory setting due to the lack of a controlled calibrated light source. Instead the minimum brightness was tested in the field with images taken in a location with clear dark skies. However this is still only a limited analog to the actual night sky that would be seen from space. Atmospheric attenuation and light pollution are still present at the location selected causing the stars to appear less bright than they otherwise would. Stars with a magnitude of 0.74 were visible in testing.

The position of the star on the sensor must be interpreted in the proper way in order to correctly identify the stars for the purpose of star tracking. Incorrectly identifying the position of the star will prevent the algorithms for star triad identification from working. Calibration of the camera was performed using the publicly available Camera Calibration Toolbox for Matlab. The toolbox allows for images to be undistorted and then estimates the error remaining. For the chosen camera and lens the error is less than one arc-minute in both the x and y directions. Verification of this through night time testing was difficult as taking an image with multiple stars depended greatly on the star constellations visible at the time of testing and the ability of the camera to image the dim objects.

The total sky coverage to be expected from the star tracker was determined using a Matlab simulation. The simulation uses a rectangular FOV of various sizes and orientations to determine the number of stars visible. The simulation uses a Monte-Carlo approach to simulate all possible camera boresights and orientations. The results, as expected, show that a star tracker benefits greatly with the increased FOV. Furthermore it provides a basis for selection of system components based on desired coverage requirements.

Situational sky coverage is also determined using STK to produce camera boresights for a typical Nanosatellite on orbit. This is useful because the area of the celestial sphere that a satellite in a sun synchronous orbit will see changes very slowly and the distribution of stars across the sky is not uniform. For satellites with short mission durations, such as nanosatellites, coverage can be compromised by the orbit selection and star tracker may not be viable. In addition to determining the number of stars within the FOV linking to STK also allows for the determination of whether the Sun or Moon are in the FOV which prevents other stars from being detected. In those cases sky coverage is not available.

7.2 Future Work

There are several areas in which the project can be continued and improved. The first is the testing of the minimum brightness. Due to a lack of testing equipment it was not possible to determine the minimum brightness that the camera detected in a controlled lab environment. This is important in order to help gauge the performance of the camera in the field where there is limited control over the environmental conditions which will impact the appearance of stars.

The camera currently outputs to an FPGA development board which is large and requires a 40 pin connector between the camera breakout board and the FPGA. Integrating the FPGA and an SRAM module onto the camera breakout board would decrease the system size and prepare the system for use on a mission. Currently the camera has to be programmed via I2C by a separate microcontroller which serves as a stand in for an OBC, programming an I2C interface for the FPGA to program the camera on startup would lessen the number of pieces of equipment necessary during testing. FPGAs are well suited to performing many similar tasks at once due to their flexible architecture. Programming into the FPGA the image calibration information to remove hot pixels, reduce noise and undistort the image would decrease the time taken to process images after they are taken.

Full environmental testing should be performed on the camera system to ensure its operability in the space environment. A thermal test has been performed and it shows the camera continues to operate over the full range of temperatures expected. Testing the camera in a Thermal Vacuum Chamber would also test the camera for the vacuum environment of space while confirming its ability to radiate enough thermal energy away to remain active without convection. Vibrational tests should also be performed to verify that the camera system survives launch and that the lens system is not affected by the vibrations and is still at the desired level of focus.

Further experimentation with the camera settings could improve the performance of the sensor. Without a controlled low brightness test as explained above it is difficult to predict the performance of the camera in extremely low light level environments. With a controlled light level test more camera settings should be varied to find the optimal settings for the camera.

Further night sky imaging should be performed to obtain images with multiple stars to allow for the verification of the uncertainty in the star positions. This is limited by the weather as well as the time of year as different constellations are visible at different times.

References

1. **1st Canadian Nanosatellite Workshop.** *Small is Beautiful.* Quebec City : s.n., 2012.

2. **California Polytechnic State University.** *CubeSat Design Specification Rev. 13.* San Luis Obiso : s.n., 2013.

3. **NASA.** NASA Helps Launch Student-Built Satellites as Part of CubeSat Launch Initiative. *NASA.* [Online] 11 20, 2013. [Cited: 03 04, 2014.] http://www.nasa.gov/press/2013/november/nasa-helps-launch-student-built-satellites-as-part-of-cubesat-launch-initiative/#.UxZSjPldV8E.

4. Russian Dnepr conducts record breaking 32 satellite haul. *NASA Space Flight.* [Online] 11 23, 2013. [Cited: 03 04, 2014.] http://www.nasaspaceflight.com/2013/11/russian-dnepr-record-breaking-32-satellite-haul/.

5. UNISAT-5 and its Payloads. *GAUSSTEAM.* [Online] [Cited: 03 04, 2014.] http://www.gaussteam.com/unisat-5/.

6. **QB50.** Mission Objectives. *QB50.* [Online] [Cited: 03 04, 2014.]

7. **Wertz, James R and Larson, Wiley J.** *Space Mission Analysis and Design.* New York : Space Technology Library , 2010.

8. **ISIS.** Static Earth Sensor. *CubeSat Shop.* [Online] 2014. [Cited: September 25, 2014.] http://www.cubesatshop.com/index.php?page=shop.product_details&flypage=flypage.tpl&product_id=103&category_id=7&option=com_virtuemart&Itemid=69&vmcchk=1&Itemid=69.

9. **SSBV Aerospace and Technology Group.** *SSBV Fine Sun Sensor.*

10. *Survey of worldwide Pico- and Nanosatellite missions, distributions and subsystem technology.* **Bouwmeester, J. and Guo, J.** 2010, Acta Astronautica 67, pp. 854-862.

11. Star Tracker and Hood Assembly Support Equipment, Voyager Spacecraft. *Smithsonian Air and Space Museum.* [Online] [Cited: 02 19, 2014.] http://airandspace.si.edu/collections/artifact.cfm?id=A19990065003.

12. *Galileo Spacecraft Autonomous Attitude Determination Using a V-Slit Star Scanner.* **Mobasser, Sohrab and Lin, Shuh-Ren.** 1991. IEEE.

13. **Doody, Dave.** *Deep Space Craft: An Overview of Interplanetary Flight.* Chichester, UK : Praxis Publishing Ltd., 2009.

14. **Kollsman Instrument Corp.** *Spacecraft Star Trackers.* s.l. : NASA, 1970 .

15. *The Advancing State of the Art in Second Generation Star Trackers.* **Eisenman, Allan Read and Liebe, Carl Christian.** 1998. IEEE Aerospace Conference.

16. **Padro, Jorge.** *Development of a Star Tracker Based Reference System for Accurate Attitude Determination of a Simulated Spacecraft.* 2012.

17. **University of Applied Sciences Aachen.** Images of the Earth. *COMPASS-1 CubeSat.* [Online] [Cited: 03 05, 2014.] http://www.raumfahrt.fh-aachen.de/compass-1/results.htm.

18. **Space Systems Laboratory University of Kentucky.** KySat-1. *Space Systems Laboratory.* [Online] [Cited: 03 05, 2014.] http://ssl.engineering.uky.edu/missions/orbital/kysat1/about-kysat-1/.

19. —. Image Processing Unit. *Space Systems Laboratory.* [Online] [Cited: 03 05, 2014.] http://ssl.engineering.uky.edu/image-processing-unit-ipu/.

20. **Kramer, Herbert J.** CSTB-1. *Earth Observation Portal.* [Online] [Cited: 03 05, 2014.] https://directory.eoportal.org/web/eoportal/satellite-missions/c-missions/cstb1.

21. **Istanbul Technical University.** ITUpSAT1. *USTTL.* [Online] [Cited: 03 05, 2014.] http://usl.itu.edu.tr/en/projects/itupsat1.

22. **Tokyo Institute of Technology.** Camera Subsystem. *CUTE 1.7 + APD II Project.* [Online] [Cited: 03 05, 2014.] http://lss.mes.titech.ac.jp/ssp/cute1.7/subsystem_camera_e.html.

23. **Aalborg University.** Camera. *AAU CubeSat.* [Online] [Cited: 03 05, 2014.] http://www.space.aau.dk/cubesat/.

24. **Stras, Luke, et al.** *The Design and Operation of The Canadian Advanced Nanospace eXperiment.*

25. **University of Würzburg.** STELLA. *University of Würzburg.* [Online] 11 14, 2013. [Cited: 03 05, 2014.] http://www8.informatik.uni-wuerzburg.de/wissenschaftforschung/stella/.

26. **Kaia, Glassey Roseanne.** *Developement of an Imager System for Low-Powered Limited-Bandwidth Space Applications.* San Luis Obiso : California Polytechnic State University, 2009.

27. **Erlank, Alexander Olaf.** *Development of CubeStar a CubeSat Compatible Star Tracker.* s.l. : University of Stellenbosch, 2013.

28. **Technical University of Denmark.** *The Micro Advanced Stellar Compas A Fully Autonomous Star Tracker.*

29. **Space Micro.** *µSTAR Tracker .* 2014.

30. *Development of the Pico Star Tracker ST-200 - Design Challenges and Road Ahead.* **Segert, Tom, et al.** 2011. 25th Annual AIAA/USU Conference on Small Satellites.

31. **Blue Canyon Technology.** *Nano Star Tracker High Performance Attitude Determination for CubeSats.*

32. **Sinclair Interplanetary.** *ST-16 Star Tracker.*

33. **Holst, Gerald C.** *CCD Arrays Cameras and Displays.* s.l. : JCD Publishing, 1998.

34. Astronomy 302 Lecture 8. [Online] [Cited: 02 23, 2014.] http://exoplanet.as.arizona.edu/~lclose/a302/lecture%208/Lecture_8.html.

35. *Review of CMOS image sensors.* **Bigas, M., et al.** 2006, Microelectronics Journal 37, pp. 433-451.

36. **Litwiller, Dave.** CMOS vs. CCD: Facts and Fiction. *Photonics Spectra.* 2001.

37. **Jones, Jill.** *Three Buttes Observatory.* [Online] [Cited: 02 23, 2014.] http://www.threebuttes.com/anti-blooming.htm.

38. **Turchetta, Renato, Spring, Kenneth R. and Davidson, Michael W.** Introduction to CMOS Sensors. *Optical Microscopy Primer.* [Online] 07 16, 2004. [Cited: 02 23, 2014.] http://micro.magnet.fsu.edu/primer/digitalimaging/cmosimagesensors.html.

39. **Ogiers, Werner.** CMOS Imaging Sensors for Space Applications. [book auth.] Henry Baltes, Wolfgang Gopel and Joachim Hesse. *Sensors Update Volume 4.* 1998, pp. 167-193.

40. *Detection of Visible Photons in CCD and CMOS: A Comparitive View.* **Magnan, Pierre.** 2003. Proceedings of the 3rd International Conference on New Developments in Photodetection. pp. 199-212.

41. **Janesick, James R.** *Scientific Charge-Coupled Devices.* Bellingham Washington : SPIE Press, 2001.

42. **Yadid-Pacht, Orly and Etienne-Cummings, Ralph.** *CMOS Imagers: From Phototransduction to Image Processing.* s.l. : Kluwer Academic Publishers, 2004.

43. **Nakamura, Junichi.** *Image Sensors and Signal Processing for Digital Still Cameras.* s.l. : Taylor and Francis Group, 2006.

44. **Olympus America.** Introduction to CMOS Image Sensors. *Olympus Microscopy Resource Centre.* [Online] [Cited: 05 28, 2013.] http://www.olympusmicro.com/primer/digitalimaging/cmosimagesensors.html.

45. **Holst, Gerald C. and Lomheim, Terrence S.** *CMOS/CCD Sensors and Camera Systems.* s.l. : JCD Publishing and SPIE Press, 2007.

46. *Determining the Fixed Pattern Noise of a CMOS Sensor: Improving the Sensibility of Autonomour Star Trackers.* **Pereira, Eduardo dos Santos.** 2, São José dos Campos : Journal Of Aerospace Technology and Management, 2013, Vol. 5.

47. **Porter, William C., et al.** Dark Current Measurements in a CMOS Imager. [book auth.] Morley M. Blouke and Erik Bodegom. *Sensors, Cameras, and Systems for Industrial/Scientific Applications IX.* 2008.

48. **Tian, Hui and Gamel, Abbas El.** *Analysis of 1/f Noise in CMOS APS.*

49. **Sasian, Jose.** *Introduction to Aberrations in Optical Imaging Systems.* s.l. : Cambridge University Press, 2013.

50. **Malacara-Hernandez, Daniel and Malacara-Hernandez, Zacarias.** *Handbook of Optical Design.* s.l. : CRC Press, 2013.

51. **Farrell, Joyce, Xiao, Feng and Kavusi, Sam.** *Resolution and Light Sensitivity Tradeoff with Pixel Size.* Santa Clara California : s.n.

52. **Wolfe, William L.** *Optical Engineer's Desk Reference.* Washington D.C. : Optical Society of America, 2003.

53. **CoMedia.** *C328 Camera Module Datasheet.* http://www.electronics123.net/amazon/datasheet/C328-7221.pdf : s.n.

54. **Omnivision.** *OM7692 Datasheet.* http://www.ovt.com/download_document.php?type=sensor&sensorid=84 : s.n.

55. **Saelig.** *Microcam Datasheet.* http://www.4dsystems.com.au/downloads/micro-CAM/Docs/uCAM-DS-rev3.pdf : s.n.

56. **Quasar Electronics.** *1/3 Monochrome Camera Module Datasheet.* [http://www.quasarelectronics.co.uk/kit-files/camera-module/d-c3188a.pdf] s.l. : Quasar Electronics.

57. **Omnivision.** *OV7690 Camera Module Datasheet.* http://www.ovt.com/download_document.php?type=sensor&sensorid=45 : s.n.

58. **Videology Imaging Solutions Inc.** *Application Note 24B752XA Wide VGA B&W CMOS Board Camera.* s.l. : Videology Imaging Solutions Inc., 2012.

59. **Edmund Optics.** High Resolution Infinite Conjugate µ-Video™ Imaging Lenses. *Edmund Optics.* [Online] Edmund Optics. [Cited: 03 05, 2014.] http://www.edmundoptics.com/imaging/imaging-lenses/techspec-lenses/high-resolution-infinite-conjugate-micro-video-imaging-lenses/2589.

60. **Marshall Electronics.** High Resolution Miniature Glass Lenses. *Marshall Electronics USA.* [Online] Marshall Electronics. [Cited: 03 05, 2014.] http://www.marshall-usa.com/optical/lenses/ccd_cmos/44.php.

61. **Sunex Inc.** Miniature CMOS lens for 1/3" format. *Sunex Partner for Optical Solutions.* [Online] Sunex Inc. [Cited: 03 05, 2014.] http://www.optics-online.com/dsl_third.asp.

62. **Newport Corporation.** *Lens Selection Guide.* 2001.

63. **Kalos, H. Malvin and Whitlock, A. Paula.** *Monte Carlo Methods 2nd Edition.* s.l. : Wiley, 2008.

64. Yale Bright Star Catalog. [Online] [Cited: 7 21, 2012.] http://tdc-www.harvard.edu/catalogs/bsc5.html.

65. **Curtis, Howard D.** *Orbital Mechanics for Engineering Students.* Kidlington, Oxford : Elsevier, 2009.

66. **Analytical Graphics, Inc.** Systems Toolkit. *AGI.* [Online] AGI. http://www.agi.com/products/stk/.

67. **Fairchild Semiconductor.** *AN-5017 LVDS Fundamentals.* 2005.

68. **Altera.** *Cyclone IV FPGA Device Family Overview.* 2013.

69. —. *DE2-115 User Manual.* 2010.

70. **Aptina Imaging.** *MT9V022: 1/3" Wide-VGA CMOS Digital Image Sensor.* 2005.

71. **Maxim Integrated .** MAX9111 Datasheet. *Maxim Integrated.* [Online] http://datasheets.maximintegrated.com/en/ds/MAX9111-MAX9113.pdf.

72. **Faccio, Federico.** Radiation Effects and Hardening by Design in CMOS Technologies. [book auth.] Herman Casier, Michiel Steyaert and Arthur H. M. Van Roermund. *Analog Circuit Design.* s.l. : Springer, 2011.

73. *Simulation of Space Radiation for Nanosatellites in Earth Orbit.* **Trusculescu, M. F. and Sima, O.** 1, s.l. : Romanian Report in Physics, 2010, Vol. 64.

74. **Smith, Warren J.** *Modern Optical Engineering 4th Ed.* s.l. : McGraw Hill Professional, 2007.

75. **Bouguet, Jean-Yves.** Calibration Toolbox for Matlab. [Online] 12 02, 2013. [Cited: 06 30, 2014.] http://www.vision.caltech.edu/bouguetj/calib_doc/.

76. **Tomshine, Jonathan.** Dark Sky Finder. *Jshine.* [Online] [Cited: July 7, 2014.] http://www.jshine.net/astronomy/dark_sky/.

77. **Stellarium.** Stellarium. [Online] http://www.stellarium.org/.

78. **Mahajan, Virendra N.** *Optical Imaging and Aberrations Part 1: Ray Geometrical Objects.* Belmont Washington : SPIE Press, 1998.

79. **Shcherback, Igor and Yadid-Pecht, Orly.** CMOS APS MTF Modeling. [book auth.] Orly Yadid-Pecht and Ralph Etienne-Cummings. *CMOS Imagers: From Phototransduction to Image Processing.* s.l. : Kluwer Academic Publishers, 2004, pp. 64-85.

80. **Boreman, Glenn D.** *Modulation Transfer Function in Optical and Electro-Optical Systems.* s.l. : SPIE, 2001.

81. *Survey and Comparison of Focal Plane MTF Measurement Techniques.* **Dutton, Tracy, Lomheim, Terrence and Nelson, Mark D.** 2002. Infrared Spaceborne Remote Sensing IX.

82. **Atkins, Bob.** Modulation Transfer Function - what is it and why does it matter? *Photo.* [Online] 04 2007. [Cited: 02 24, 2014.] http://photo.net/learn/optics/mtf/.

83. **Mansurov, Nasim.** How to Read MTF Charts. *Photography Life.* [Online] [Cited: 02 24, 2014.] http://photographylife.com/how-to-read-mtf-charts.

84. **Sunex Inc.** *Application Note: Image Circle Tolerance.*

85. *Modeling and Estimation of FPN Components in CMOS Image Sensors.* **Gamal, Abbas El, et al.** s.l. : SPIE, 1998.